Master's thesis

NTNU
Norwegian University of Science and Technology
Faculty of Natural Sciences
Department of Physics

Kristoffer Sosulski Moen

The Role of Planetary Waves in Gravity Wave Activity in the Middle Atmosphere During Northern Hemisphere Winter

A High-Resolution General Circulation Model Approach

Master's thesis in Applied Physics & Mathematics
Supervisor: Patrick J. Espy
Co-supervisor: Yvan J. Orsolini
June 2023

NTNU
Norwegian University of
Science and Technology

Kristoffer Sosulski Moen

The Role of Planetary Waves in Gravity Wave Activity in the Middle Atmosphere During Northern Hemisphere Winter

A High-Resolution General Circulation Model Approach

Master's thesis in Applied Physics & Mathematics
Supervisor: Patrick J. Espy
Co-supervisor: Yvan J. Orsolini
June 2023

Norwegian University of Science and Technology
Faculty of Natural Sciences
Department of Physics

NTNU
Norwegian University of
Science and Technology

Abstract

The role of large-scale planetary waves (PWs) on the smaller-scaled gravity waves (GWs) in the stratosphere and mesosphere in the winter Northern Hemisphere, is studied using the high-resolution WACCM-X model. The purpose is to understand the complex nature of GWs and how PWs affect them. GWs are typically generated by winds over mountains (orographic GWs), or from shears or convection in the atmosphere (non-orographic GWs), and often propagate high into the mesosphere before breaking. This results in a GW drag on the high winds, a process crucial for the middle atmosphere dynamics. However, GWs remain a major source of error in the dynamics of models due to their small scales, interactions, and intermittency of sources. This affects the predictability of weather events with significant societal impacts. Moreover, the role of PWs in generating and propagating GWs is not fully understood. Therefore, using the high-resolution WACCM-X, this interaction is studied near the stratospheric polar vortex edge in the mid- and high-latitude stratosphere in a month-long Jan-Feb simulation of temperatures and winds. It is found that the zonal GW power, proportional to the zonal GW potential energy, is correlated with the zonal RMS PW amplitudes in the high-latitude middle atmosphere, and anti-correlated at mid-latitudes. Furthermore, non-orographic GWs dominate at high latitudes, in particular when large-amplitude PWs, generated by an excessively strong polar vortex, are present. These GWs are found to most likely be generated by strong wind shears caused by the strong PWs in the vicinity of the vortex edge. On the other hand, orographic GWs are dominant in the mid-latitudes. These waves occur when the polar vortex is displaced off the pole, in a weak state with moderate winds above significant orography, and weak PWs, consistent with recent observations. Also, orographic GWs typically appear when the stratospheric PW wind is eastward above the source orography, indicating the filtering of GWs by PWs in the stratosphere. The results generally support previous observations, but the high-resolution model run gives new insights into how GWs are generated and modulated by PWs in the winter stratosphere. However, whether there is a regularity and systematic correlation between GWs and PWs for a longer time than a month or several winters, is uncertain, and should therefore be studied further.

Sammendrag

Interaksjonen mellom storskala planetære bølger (PWs) og de langt mindre atmosfæriske tyngebølgene (GWs) i stratosfæren og mesosfæren i nordlige breddegrader, analyseres ved bruk av den høyoppløselige WACCM-X-modellen. Formålet er å bedre forstå de komplekse GWs og hvordan PWs påvirker disse. GWs oppstår typisk når vind blåser over fjell (orografiske GWs) eller fra vindskjær og konveksjon i atmosfæren (ikke-orografiske GWs), og disse propagerer typisk høyt opp i mesosfæren før de bryter. Dette resulterer i en motstandskraft på vindene i mesosfæren, en helt avgjørende prosess for den midtatmosfæriske sirkulasjonen. Likevel er GWs en vesentlig feilkilde i dynamiske modeller, grunnet deres små skalaer, interaksjoner og variable kilder. Dette påvirker varsling av ekstremvær og klimaprognoser av stor påvirkning på samfunnet. Videre er rollen PWs har i dannelsen og aktiviteten av GWs ennå ikke fullt forstått. Derfor er den høyoppløselige WACCM-X brukt for å undersøke denne interaksjonen, i nærheten av den stratosfæriske polarvirvelen, ved midtre og høye nordlige breddegrader, i en månedslang simulering av temperaturer og vind i jan-feb. Resultatene indikerer en korrelasjon mellom total sonal GW-effekt, som er proporsjonalt med sonal GW potensiell energi, og den sonale effektivverdien av PW-amplituder, i stratosfæren og mesosfæren ved høye breddegrader. I motsetning er de anti-korrelert ved midtre breddegrader. Dessuten er ikke-orografiske bølger dominerende i stratosfæren ved høye breddegrader, særlig når PW-amplituder er store i samme område, forårsaket av en usedvanlig sterk polarvirvel. Studien viser at disse GWs sannsynligvis oppstår grunnet sterke vindskjær forårsaket av sterke PWs i nærheten av polarvirvelen. Ved midtre breddegrader er derimot orografiske GWs mer dominerende. Disse oppstår særlig når polarvirvelen er forskjøvet bort fra Nordpolen, og er noe svekket, med virvelkanten over orografi og med svake PWs i nærheten, noe som er i samsvar med observasjoner. Dessuten oppstår disse bølgene typisk når PW-vinder er vestlige i stratosfæren over orografi, noe som indikerer en filtrering av GWs ved PWs. Resultatene underbygger generelt tidligere funn, men den høyoppløselige modellen gir også ny innsikt i hvordan GWs oppstår og moduleres av PWs i stratosfæren på vinteren. Likevel er det usikkert om det er en regelmessig og systematisk korrelasjon mellom GWs og PWs dersom et lengre tidsintervall eller flere vintre ville blitt studert, og er derfor et mulig videre fokus.

Preface

This master's thesis concludes five years of studying physics at NTNU. Effectively 7250 hours were spent studying the past years, many of which were for calculating integrals, writing and debugging codes, reading books and articles, and fighting through endless deadlines and hard exams. But also many moments getting curiously lost down the rabbit hole in exciting physics and maths concepts, with some incredible epiphanies regarding the physics surrounding us. Similarly, the last months working on this thesis have been a roller-coaster experience. On the one hand, it has been a story of struggling with confusing results and getting frustrated at the complications of doing signal processing in a complex atmosphere model. On the other hand, it is a story of endless fascination for atmospheric dynamics, getting excited every time I see gravity waves in the clouds, and almost getting emotional as the plot I have been running for three days straight finally shows up with interesting results. These years, but especially the thesis, have all been a rewarding journey of great academic and personal development. On this note, I want to thank my thesis supervisors, prof. Patrick J. Espy at NTNU and senior researcher Yvan J. Orsolini at the Norwegian Institute of Air Research (NILU). Both have been crucial to my thesis by helping me find ways out of the frustrating problems at hand, while also helping me focus on one thing at a time rather than branch out to whatever looks interesting to me.

A master's degree in physics is an accomplishment the curious little mind of mine could only dream of as a young kid. As a little 11-year-old boy, I wandered around the little stream near my home, measuring and drawing maps of water flow and ground temperatures in sheer fascination for understanding the phenomena. Weather, fluid mechanics, and physics in general have always been intriguing to me. After finishing my degree, that same childish curiosity is still alive and has contributed to science for the first time, but certainly not the last time. This curiosity-led journey could not have been possible without the foundation and support of my parents, Bjørnar and Eva, my two sisters, Annika and Natalie, and other family members, throughout my childhood and as a student. Thank you!

It has been five years of incredible growth personally, much due to the environment of people I have been surrounded by. I want to thank the friends I have been lucky to connect with here in Trondheim. My study friends and classmates have been great sources of help, support, intellectual discussions, and great company on and off campus. In particular, I want to thank Andreas Hennig for the way too long talks about how cool turbulent fluids and waves are while running by the river, and for inspiring me to pursue a research career further.

Sincerely,
Kristoffer S. Moen
Trondheim, Norway
June 2023

Table of Contents

List of Tables

List of Figures

Abbreviations

GW	=	Gravity wave
PW	=	Planetary wave
MW	=	Mountain wave
WACCM	=	Whole Atmosphere Community Climate Model
GCM	=	General Circulation Model
NCAR	=	National Center for Atmospheric Research (US)
DALR	=	Dry Adiabatic Lapse Rate
WN	=	(Zonal) Wavenumber
MLT	=	Mesosphere & Lower Thermosphere
NH	=	Northern Hemisphere

Chapter 1

Introduction

Over the last decades, weather and climate models have significantly improved their accuracy due to better knowledge and modelling of physical and chemical processes, and better computational resources. Their importance is crucial in predicting local and global weather and climate events with huge societal impacts, such as droughts, floods, and hurricanes. However, the models are far from complete and still cannot account for every phenomenon in this complex system. A significant source of error in the models is assumed to stem from small-scale waves in the atmosphere, called gravity waves (GW for short). They are typically generated by wind over high mountains or by large storm systems. GWs are often too small to resolve properly in weather and climate models. Hence, their effects must often be parameterised, i.e. modelled, which involves significant uncertainties. Although GWs may be small compared to planetary scales, their impact on atmospheric dynamics is significant enough to affect weather systems and thus essential to account for in models [2]. Moreover, their interactions with other large-scale waves such as planetary waves (PWs) and atmospheric tides may impact the formation and breaking of GWs. Hence, this is currently a fundamental research topic within GW research. Recent developments in computational resources and decades of atmospheric research have enabled a high-resolution General Circulation Model (GCM) called the Whole Atmosphere Community Climate Model (WACCM) to be developed [32]. This model can resolve GWs better than most other GCMs and can be used to study their effects on the atmosphere from a modelling approach. Together with observational data, this may improve how these waves are included in weather and climate models. Thus, our prediction of weather and climate events of significant impact on humanity is likely to be improved by understanding GWs better.

1.1 Gravity Wave Basics

In general, a gravity wave is a fluid wave in which gravity acts as a restoring force against the uplift force, buoyancy, to cause vertical oscillations. Well-known examples are ocean waves and ripples in a dam as a stone is thrown. This type of wave also exists in the

atmosphere and is called an atmospheric gravity wave, or just gravity wave (GW) when the atmospheric context is clear. Whereas ocean gravity waves are surface waves in the interface between water and air, atmospheric GWs are internal waves in the air, with no interface, just density distributions internally. They may form due to storms and other large convective processes, as well as strong wind shears in jets in the atmosphere, so-called non-orographic GWs. GWs can also be generated as winds meet high mountains that force the air to move up over the mountain, as seen in Fig. 1.1. The waves are then called orographic GWs, or mountain waves (MWs). Since air cools over the cold mountain, it sinks back down. However, since it is heated again when back down, it rises, and the oscillation may continue as a wave. These internal waves will affect the wind layer above it, and cause waves, and thus wave energy, to propagate upwards. As seen in Fig. 1.1 the lines of constant phases are typically tilted with respect to the vertical.

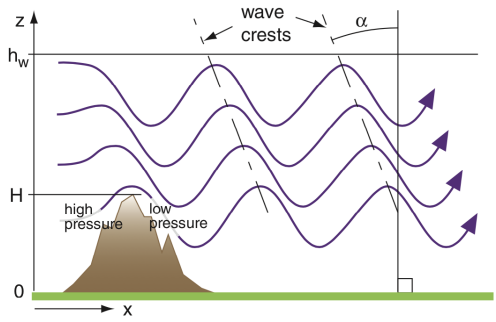

Figure 1.1: A simplified illustration of mountain-generated gravity waves. The wind comes from the left and oscillates as it passes the mountain. Wave crests become tilted as each wind layer is affected by the layer below. There is a high pressure at the crests, while low pressure is found at troughs. Image credit: Roland Stull, UBC EOAS [54].

As the waves propagate to the stratosphere ($\sim$ 12-50 km) and mesosphere ($\sim$ 50-85 km), their amplitudes become large due to decreasing air density. Eventually, the waves may break due to nonlinear wave effects, which cause a drag on the mean flow. While Fig. 1.1 shows a coherent waveform of constant wavelength, a spectrum of waves is typically generated by differences in orography or by different sources of wind shears and convection in the atmosphere. Wavelengths are typically about 10-1000 km horizontally, and 1-30 km vertically [18]. GWs are classified as small in atmospheric scales. Occasionally they manifest themselves by stripe-shaped clouds past mountains, or more spectacularly, mesospheric noctilucent clouds (also known as polar mesospheric clouds) in the summer polar nighttime, as shown in Fig. 1.2(a), and marked in 1.2(b).

1.1.1 Aspects of Gravity Waves

While mountain-generated GWs in the troposphere (0-12 km) have been studied for some time, the first recognition of GW activity in the stratosphere and mesosphere came in the 1960s, by the pioneering work of Hines [22]. Some key findings from the subsequent decades of research are presented in the following paragraphs.

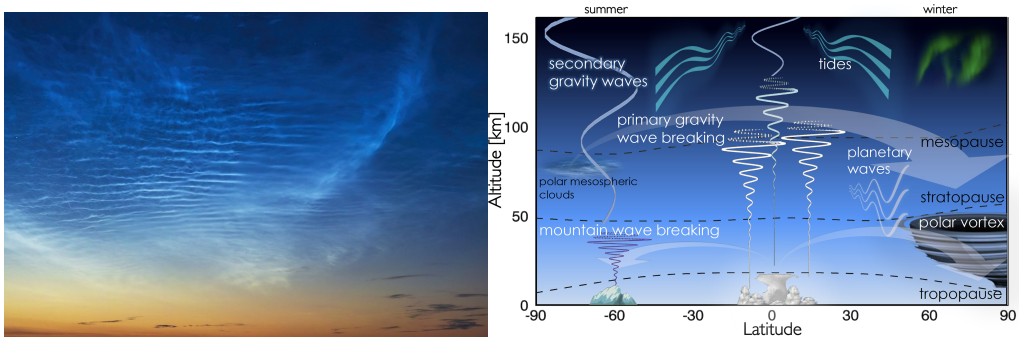

(a) **(b)**

Figure 1.2: **(a)** Mesospheric GWs visible in noctilucent clouds at around 70-80 km altitude. This phenomenon is only visible on summer nights between 50°-70°N/S. Image credit: Virginia Tech [58]. **(b)** A simplified illustration of GW generation and interactions with other waves in the atmosphere. GWs are generated by mountains, wind shears, and convective storms. These break in the mesosphere and cause drag on planetary waves, the polar vortex, tides, and the pole-to-pole circulation. However, the vortex and PWs may also affect GWs. Image credit: McCormack et al. [36],

GWs are found to significantly impact wind circulations in the stratosphere, mesosphere, and thermosphere. The pioneering work of Lindzen has found that as vertically-propagating GWs break due to instabilities in the upper mesosphere and lower thermosphere altitude, turbulent mixing occurs [28]. Due to the momentum balance in the mesosphere, this causes a zonal (east-west) drag opposing the mean flow. Indeed, it is found that GW drag strongly reduces the stratospheric polar vortex jet, i.e. the strong eastward jet stream in the upper stratosphere and lower mesosphere of the winter pole, as seen in Fig. 1.2(b) [18]. Furthermore, GWs are the dominant drivers of the quasi-biennial oscillation [32]. This is the nearly 28-month-periodic reversal of zonal winds in the stratosphere around the equator, affecting the jet streams [56]. In addition, GWs are essential drivers of the mesospheric semi-annual oscillation, where zonal winds reverse twice per year in the equatorial mesosphere. It is therefore the dominant source of mesospheric wind variability, and a significant contributor to stratospheric dynamics, together with the much larger planetary waves (PWs).

The thermal structure is also strongly affected by GWs. It has been proposed by Holton that GWs are the leading cause of abnormal temperature gradient reversals in the high mesosphere, where the summer pole is cooler than the winter pole [24]. Thus, GWs drive the mesosphere and lower thermosphere (MLT) circulation off the radiative equilibrium in the summer and winter hemispheres [32], [18].

GWs may impact, but also be reversely impacted by, the much larger planetary waves (PWs). These are large-scale temperature and wind variations, with typical periods of 2-20 days, that are generally strong in the winter stratosphere and occasionally also mesosphere. Also, atmospheric tidal waves (daily oscillations primarily due to solar radiation) may interact with GWs, but this becomes significant only in the MLT. These GW interactions with PWs and tides may change the amplitude and phase of the larger waves [32], [44]. Furthermore, PWs may filter GWs, in particular in the stratosphere.

Here PWs are found to selectively transmit orographic GWs of certain phase speeds, and absorb others, in particular in the intermediate range of 50-200 km horizontal wavelengths [26], [13]. Furthermore, GW activity is found to maximise when the PW winds are in their maximal eastward phase in the winter stratosphere and mesosphere, and minimised when PW winds are maximally westwards due to the critical level filtering of waves of similar phase speeds [35]. Moreover, several studies have found that 2- and 16-day PWs in the stratosphere and mesosphere modulate GWs, causing a periodic forcing to occur in the mesopause [18], [35]. A previous study using the high-resolution WACCM5 model, suggests that PWs and GWs are out-of-phase in activity in the austral winter mid-latitude mesosphere, but emphasises that there could exist indirect interactions that may possibly affect this planetary-gravity wave interaction [3]. Fig. 1.2(b) illustrates the different waves and circulations GWs may interact with.

In the winter stratosphere and mesosphere, GWs are sometimes generated by the forcing from strong wind shears, typically near the stratospheric polar vortex edge [15]. During instability events of the vortex, a strong meandering of the vortex jet may occur and both PWs and GWs become prominent in the vicinity of the vortex edge. See Fig. 1.2(b) illustrating PWs around the vortex. GW energy has been found to be large at the vortex edge, low in the centre and intermediate outside of the vortex in the Northern Hemisphere (NH) stratosphere [15]. However, the nature of these non-orographic GWs is complicated, in terms of their sources, occurrence, generation, and propagation. A study from 2014 pointed out that the complexity of the generation process of GWs from jets and fronts, like the polar vortex, makes it challenging to study and find deterministic relations [46]. A proposed way forward is to study high-resolution observational datasets, as well as high-resolution GCMs that include parameterisations of non-orographic waves.

1.2 The Role of High-Resolution Models in Gravity Wave Research and GCM Parameterisations

Models are necessary to study the interactions of the complex atmosphere. There is a constant interplay between observations and models. Observations improve models, and models are checked against observations [34]. With a model, the response of different initial conditions in time can be tested and highlight aspects of atmospheric dynamics that may be difficult to observe, e.g. the GW impact on large-scale circulation over time. For this reason, models and simulations of the atmosphere are important in the development of GW research.

The fact that unresolved GWs exist in General Circulation Models (GCMs) like climate and weather models, has been known for decades. A first attempt to parameterise the GW drag effect on the mean flow in GCMs, was done by Lindzen and later Holton, and is still the cornerstone of methods used today [28], [24]. The key parameters, like wavelengths, phase speeds etc. are found by observations. The models use reasonable assumptions of GW generation and propagation, although they typically oversimplify the physics. Moreover, PWs and tides may affect the GWs in ways that are not accounted for in the models. Additionally, a significant source of error in the GW drag is likely from the failure of GCMs to determine GW sources and their intermittency [1].

Adding the uncertainty of parameter determination, GW assumptions, and GW source resolution issues, GW parameterisation becomes a major source of model bias and uncertainty. This primarily restricts the predictability of the middle- and upper atmospheric circulations. Like a butterfly effect, downward interactions of the stratosphere and mesosphere on the troposphere causes the prediction of weather and climate events close to ground to become uncertain [34], [30].

WACCM, a model provided by the National Center for Atmospheric Research, has been in constant development for the past two decades [41]. Compared to other GCMs, its high-resolution version is significantly better resolved with 0.25° horizontal (roughly 25 km in mid-latitudes) and 0.2-0.7 km vertical resolution, up to 700 km altitude (in the extended WACCM-X version). However, due to the high resolution, only a restricted time span is possible to model. Nevertheless, such high-resolution full-atmosphere models are ideal for studying the highly-resolved complex interactions of the atmosphere. The first-ever high-resolution WACCM simulation showing GWs in the mesosphere was done in 2014 [32]. The smallest properly resolved waves in the study were found to be about 200-250 km, even though the horizontal resolution is smaller. In addition, the simulations indicate the increasing importance of GWs at higher altitudes, which is in accordance with experiments.

A strong advantage of WACCM, particularly in relation to the complexity of GWs around fronts and jets, is that it has a built-in scheme for generating non-orographic GWs based on convection and instabilities [41]. Hence, a high-resolution WACCM-X simulation of the complex GW processes in the atmosphere is invaluable in understanding the mechanisms, comparing them with observations, and consequently improving the GCMs even further.

1.3 Thesis Motivation and Context

The enormous complexity of GWs in the middle atmosphere, both orographic and non-orographic, calls for more research on the topic. To cite A. Dörnbrack from his 2021 article about orographic GWs in the stratosphere above Europe in the winter of 2016: ”The deeper I sounded (...), the more I found about the manifold processes occurring during this period. (...) Very deep is the well of the facts. Should we not call it bottomless?” [14]. Furthermore, non-orographic GWs generated in the stratosphere in the vicinity of the winter polar vortex have been a major challenge to understand. As suggested by Plougonven & Zhang, high-resolution GCMs, in parallel with high-resolution observations, may improve our understanding of these non-orographic GWs in the polar winter stratosphere and mesosphere [46]. Consequently, the parameterisation of these processes in GCMs may be further improved. Although the research on GWs may seem bottomless at first, every step towards a greater understanding of them, is a step towards better weather and climate models, hence predictions of weather.

A major challenge in our understanding of GWs in the middle atmosphere stems from determining different stratospheric sources of GWs. Large-scale PWs that manifest as large temperature and wind variations, may cause strong temperature and wind gradients in the middle atmosphere. This may contribute to the generation of GWs due to strong shears. Understanding the location and occurrence of this possible generation mechanism

is crucial for better understanding the processes that may affect GW activity in the middle atmosphere. In addition, the interactions between GWs and PWs go both ways and are complex. Studies focusing on the GW interaction of PWs are many. Somewhat fewer studies also focus on the reverse interaction of PWs on GWs, and the complexity that arises here makes it difficult to find general relations to explain them. In particular, the relation becomes difficult as the PWs are linked to the polar vortex, showing significant variability in the polar winter middle atmosphere.

A recent master's thesis by H. Alexandersen used the high-resolution WACCM version 5 to study the interactions between GWs and PWs in the high-latitude middle atmosphere in the Southern Hemisphere winter (July). It found an anti-correlation of the wave amplitudes over the course of a week [3]. However, the analysis was only conducted at roughly 70 km altitude at a single point, downstream of small islands in the Southern Ocean, focusing mainly on orographic GWs. Furthermore, the correlation was based on a relatively sparse time series, using data for temperature PW and GW amplitudes once daily for a week. Hence, it is of great interest to expand the analysis to the whole middle atmosphere at mid- to high-latitudes in the polar winter, where PWs and the polar vortex are located and GWs are strong, as well as extending the time series.

1.4 Thesis Statement

Armed with the high-resolution WACCM-X model, the main goal is to follow up and extend the findings and work of H. Alexandersen, where the interaction of PWs with GWs was studied in the model. While he focused on orographic GWs, the following analysis aims to classify both orographic and non-orographic waves. For the latter, the focus is mainly on waves generated by shears in the stratosphere. Hence, the role of PWs in this mechanism will be studied in the high-resolution model, as has been suggested from previous work [46]. To address the issues mentioned in the last paragraph, the following analysis will look at the variations of zonally-averaged amplitudes and power of the waves, at a range of latitudes and altitudes in the winter hemisphere middle atmosphere. This is in contrast to the single grid point amplitude analysis. For this, a total zonal GW power, proportional to the total zonal GW potential energy, is derived by integrating the spatial power density spectrum of GWs. In contrast, zonally-averaged PW amplitudes are found by applying a zonal RMS of PW temperature. The central question revolves around whether there is any correlation between this GW power and PW RMS temperature in the middle atmosphere, hence a possible link.

Furthermore, to isolate GWs and PWs, spatial and temporal filters are used, a spatial medial filter and a temporal IIR digital filter. These have been developed in a pre-thesis project report [38] as an extension and improvement to the filtering in Alexandersen's work. The emphasis of the report was on filtering, using the same July WACCM5 data Alexandersen studied. The wave isolation was successful, compared with observations and models, and improved Alexandersen's method. Several methods and theoretical concepts are developed from this pre-thesis report and are crucial for this thesis where the PW-GW interactions are in focus.

A significant advantage of using WACCM-X, compared to the WACCM5 used by Alexandersen, is the inclusion of wind. This enables an analysis of the relation of GWs

and PWs in terms of the location of the polar vortex edge, the strength of the vortex, as well as locating regions of large shears, that are likely key sources of non-orographic GWs in the middle atmosphere. Moreover, this simulation by WACCM-X is a particular high-resolution run, and the model does indeed include a scheme for generating non-orographic GWs, which is often not the case for GCMs. Additionally, WACCM has been known to produce a realistic winter stratosphere at mid to high latitudes where strong PWs and GWs reside near the polar vortex edge. It has been noted that the model may realise spontaneous adjustments of the vortex, an important stratospheric mechanism typically generating PWs and GWs around the vortex [32]. Thus, WACCM-X is a suitable choice for studying the complex nature of both orographic and non-orographic GWs, and their interactions with PWs in the vicinity of the polar vortex.

The WACCM-X dataset to be analysed is retrieved from NCAR's Globus file-sharing website [40]. The dataset is generated using a supercomputer before being publicly shared on the website. However, at the time of this thesis, only data from the 13th of January to 28th of February is available, although a full-year run is currently in progress. Due to the dominance of GWs, PWs, and the polar vortex in the winter hemisphere [2], this thesis focuses on the Northern Hemisphere (NH). Since PWs and GWs most typically occur at mid- and high-latitudes, the region of study will mainly be concentrated between 30°N to 80°N. In altitude, the main focus will be on stratospheric processes, mainly around 41 km altitude, and to some degree on mesospheric processes at 71 km. However, the whole altitude range from the ground to the mesopause around 85 km will be covered in the analysis. Due to the restrictions of computational resources, only the 31-day dataset from 13th January to 12th February is analysed in this thesis, with a time resolution of 6 hours.

Hence, the thesis revolves around the following questions:

- Where do GWs occur in the 31-day-long WACCM-X winter simulation?
- Where are orographic GWs typical? What is the role of PWs in their existence and propagation in the middle atmosphere? Is a filtering process present?
- Where and how do non-orographic GWs appear? Are their activity related to PWs?
- Is there any correlation between the zonal GW power, related to the GW potential energy, and the zonally-averaged PW amplitudes in the NH middle atmosphere during winter? Does it indicate interactions occur?

1.5 Thesis Outline

To get a grasp of the characteristics of the GWs from a more theoretical point of view, the underlying GW theory is presented in Section 2, based on the theory presented in the pre-thesis report [38]. Here, a thorough introduction to how to arrive at the GW dispersion relation, central to GW characterisations, from fundamental fluid equations and central energy and momentum flux equations, is presented. In addition, a presentation of PWs is given. In Section 3, the methodology of the project is presented. This includes a more detailed explanation of the WACCM-X model and the dataset format as retrieved from the National Center for Atmospheric Research (NCAR). Moreover, since the data contain

multiscale information, spatial and temporal filtering schemes developed in the pre-thesis report, are applied to isolate the wave types, and are thoroughly described here. Additionally, the method of deriving the zonal GW power from a spatial power spectrum and some description of methods for temporal spectra are described here.

Finally, Section 4 presents and discusses the results. The structure of this can be summarised in the following:

- Section 4.1 establishes and presents the atmosphere at hand in the simulation. That means the simulation realisation and different results for GWs, PWs, and the polar vortex are all presented.
- Section 4.2 is two-fold. First, a presentation and discussion of the spatial wavenumber power spectrum of GWs is given. Then, this is used to derive the zonal GW power, a central quantity in the forthcoming discussion.
- Section 4.3 presents and discusses the zonal RMS amplitudes of PW temperatures.
- Section 4.4 presents and discusses significant periods of the PW RMS T and GW power and the zonal mean wind in terms of Lomb-Scargle periodograms.
- Section 4.5 tries to connect the discussion together by discussing GW-PW interactions. Correlation plots of GW power vs. PW RMS T are shown and discussed. This section is the culmination and central point of the thesis.

Chapter 2

Theory

To understand atmospheric GWs, their characteristics, propagation, and interactions with PWs, the fundamental theory of GWs and PWs should be presented. The fundamental equations for GWs, their propagation, and dissipation, as well as momentum flux, are derived in the following sections. These are based on GW and large-scale fluid dynamics presented by Andrews [4], Vallis [56], Fritts & Alexander [18], Espy [17], and Liu [29]. This chapter aims to highlight assumptions and limits underlying the mathematical GW theory by walking through these rather detailed.

2.1 Atmospheric Structure

The temperature profile typically classifies the structure of the atmosphere into distinct layers. The vertical profile shown in Fig. 2.1 shows that the temperature does not vary equally in altitude everywhere but shows distinct vertical temperature gradients with breaking points.

The lowest layer is the **troposphere**, which reaches up to 10-12 km altitude and contains most of the weather phenomena that directly impact life. In this layer, temperature decreases with altitude approximately linearly with a lapse rate, i.e. temperature gradient, of about -6.5K per kilometre of displacement upwards. This is due to the air being heated primarily from the ground up.

At the top of the troposphere lies the tropopause, at about 12-18 km, where the temperature varies minimally. This region acts as a buffer layer between the troposphere below and the **stratosphere** above. In the latter layer, temperature increases linearly with altitude due to the radiative effect of ozone, which has its peak density in this layer. The stratosphere spans from 20 km to about 44 km altitude.

Above the stratosphere, lies the stratopause, at about 44-50 km where the temperature is about $0°C$ (273K). Further above, in between 50-85 km is the **mesosphere**. Here, the temperature decreases again, with a lapse rate of about -3K per kilometre. This is also the layer where GWs typically break.

Further above is the mesopause at about 85-90 km, followed by the **thermosphere**. Here, temperature increases significantly due to the effects of ionisation. This layer stretches well up to about 500-700 km.

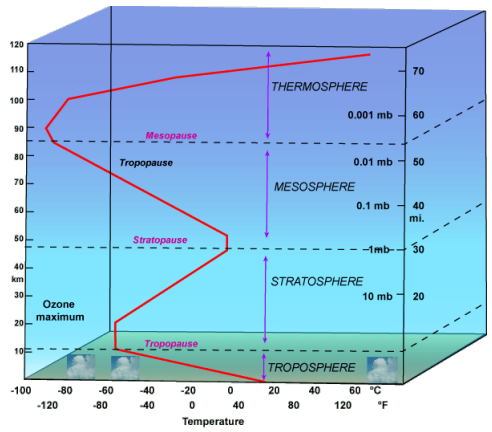

Figure 2.1: The vertical temperature profile in the atmosphere and its layers up to 120 km. Illustration credit: StratusDeck [5].

For convenience, the term **middle atmosphere** is typically used for the stratosphere and mesosphere, and is a significant region for PWs, GWs, and to lesser extent tides. For reference, the lower atmosphere is then the troposphere, and the upper atmosphere consists of the thermosphere. Another convenient term, particularly for GWs and tides, is the **Mesosphere and lower thermosphere (MLT)** region from about 50 km to 120 km. This is often used in relation to GWs since these break, deposit energy, and may regenerate here.

2.2 Parcel Theory

The concept of GWs can be established by first imagining a parcel of air, and applying thermodynamics and force balance as it is transported or perturbed from equilibrium. An air parcel at rest vertically follows the Taylor-approximated hydrostatic balance equation

$$\frac{\mathrm{d}p}{\mathrm{d}z} = -\rho g, \tag{2.1}$$

where p is the pressure from the environment, z the vertical height from a reference, ρ the mass density of the parcel and g the gravitational acceleration on Earth's surface. Assuming the air parcel is an ideal gas, the pressure, temperature and density are related by

$$p = \rho R_a T, \tag{2.2}$$

where R_a is the gas constant of air and T the parcel temperature. Inserting Eq. (2.2) into

Eq. (2.1) for ρ, one obtains

$$\frac{\mathrm{d}p}{\mathrm{d}z} = -\frac{gp}{R_a T}. \tag{2.3}$$

For an air parcel moving in dry air, the temperature change is adiabatic, meaning no parcel heat is lost to the environment. The reversible heat change is given by $\delta Q = T\delta S$, where Q is the heat and δS is the entropy change of the system. It can be shown from fundamental thermodynamical relations for the entropy, together with Eq. (2.3) that when δQ is zero per definition for the adiabatic parcel, the parcel temperature follows

$$-\left(\frac{\mathrm{d}T}{\mathrm{d}z}\right)_{\text{par}} = -\frac{R_a T}{c_p p}\left(\frac{\mathrm{d}p}{\mathrm{d}z}\right)_{\text{par}} = \frac{g}{c_p} \equiv \Gamma_a, \tag{2.4}$$

where Γ_a is the dry adiabatic lapse rate (DALR), of about 9.8 K/km.

Now, assume the parcel is perturbed by an initial external trigger force $\boldsymbol{F}_0$ (for example by orography) and moves from an altitude with temperature T_0 and density ρ_0 (parcel and environment at equal temperature and density), to a higher altitude where the surrounding air holds temperature T_1 and density ρ_1. Furthermore, let the parcel temperature and density after the displacement be T_{par} and ρ_{par}, as illustrated in Fig. 2.2. Then the temperatures would change according to the parcel lapse rate $\Gamma = -\mathrm{d}T/\mathrm{d}z$ that may or may not be equal to Γ_a.

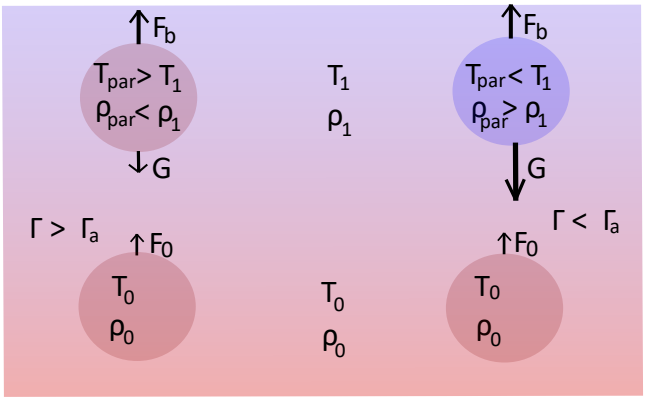

Figure 2.2: A vertical displacement of a parcel of air due to an initial external trigger force $\boldsymbol{F}_0$ in two cases of parcel lapse rate, illustrating the essentials of vertically oscillating waves. To the left: the parcel cools down slower than the environment, as $\Gamma > \Gamma_a$, and ends up warmer and lighter than the environment at the displaced altitude. Thus, the upward buoyancy ($\boldsymbol{F}_b$) is larger than gravity ($\boldsymbol{G}$), and the parcel moves upward. To the right: the parcel cools down faster than the environment, so $\Gamma < \Gamma_a$, and is colder and heavier. Gravity is larger than the buoyancy, and the parcel sinks down. Illustration made by author.

The densities of the parcel and environment can be found from the ideal gas law, and the net force on the parcel is then found by the downward gravity force and upward buoyancy force on the parcel, which becomes

$$\sum F = gV(\rho_1 - \rho_{\text{par}}), \tag{2.5}$$

which by Newton's second law becomes a simple ODE

$$\frac{\mathrm{d}^2(\delta z)}{\mathrm{d}t^2} = g\left(\frac{\rho_1}{\rho_{\text{par}}} - 1\right) = g\left(\frac{T_{\text{par}}}{T_1} - 1\right). \tag{2.6}$$

By using Eq. (2.4), and the definition of lapse rate, while also assuming only small variations of δz, one may approximate Eq. (2.6) to

$$\frac{\mathrm{d}^2(\delta z)}{\mathrm{d}t^2} = -\frac{g}{T}(\Gamma_a - \Gamma) \equiv -N^2(\delta z). \tag{2.7}$$

Here, Γ is the lapse rate of the parcel itself, and N is defined as the **Brunt-Väisälä frequency**. This frequency is identified as

$$N^2 = \frac{g}{T}\left(\frac{dT}{dz} + \frac{g}{c_p}\right), \tag{2.8}$$

where the lapse rates of parcel and DALR are inserted.

If the parcel lapse rate is lower than DALR, as seen to the right in Fig. 2.2, the perturbed parcel will accelerate back downwards and is cooler (more cooled down per altitude change as $\Gamma < \Gamma_a$) than the surrounding air and thus has a higher density. When the parcel sinks, it is heated by the surroundings until the acceleration reverses. As $N^2 > 0$, Eq. (2.7) yields simple harmonic solutions for $z(t)$, with oscillation frequency N. Since temperature increases with altitude in the stratosphere, this layer allows parcels to oscillate harmonically. The stratosphere is therefore called stable.

However, if the parcel cools down faster per altitude change than the surroundings, $\Gamma > \Gamma_a$, as seen to the right in Fig. 2.2, then the acceleration will be positive and continue to rise. As $N^2 < 0$, Eq. (2.7) will then have exponential solutions of $z(t)$, so the parcel does not oscillate. This typically happens in the troposphere and mesosphere, where the temperature decreases with altitude and is called statically unstable layers.

Eq. (2.8) may alternatively be written in terms of the potential temperature θ as

$$N^2 = \frac{g}{\theta}\frac{\mathrm{d}\theta}{\mathrm{d}z}, \tag{2.9}$$

with the potential temperature θ given by

$$\theta = T\left(\frac{p_0}{p}\right)^{R_a/c_p} = \frac{p}{\rho R}\left(\frac{p_0}{p}\right)^{c_p/c_v}, \tag{2.10}$$

relative to a reference pressure p_0, R_a is the dry air gas constant, and c_p and c_v as the specific heat capacities of dry air.

2.3 Equations of Motion

Atmospheric gravity waves are internal waves with a continuous stratification of densities. A set of equations of motion can be derived for these waves. These include the three momentum equations derived from the inviscid Navier-Stokes equations, which are

$$\frac{\mathrm{D}u}{\mathrm{D}t} - fv + \frac{1}{\rho}\frac{\partial p}{\partial x} = X, \tag{2.11}$$

$$\frac{\mathrm{D}v}{\mathrm{D}t} + fu + \frac{1}{\rho}\frac{\partial p}{\partial y} = Y, \tag{2.12}$$

$$\frac{\mathrm{D}w}{\mathrm{D}t} + \frac{1}{\rho}\frac{\partial p}{\partial z} + g = 0, \tag{2.13}$$

where $u = U + u'$, $v = V + v'$ and $w = W + w'$ are x, y and z velocities respectively, with U, V, W as mean velocity components and u', v', w' the velocity fluctuation components. Furthermore, $f = 2\Omega\sin(\vartheta)$ is the Coriolis parameter with Earth's angular frequency $\Omega = 7.292 \cdot 10^{-5}$ rad/s and latitude ϑ, while X and Y are undetermined forcings. Here

$$\frac{\mathrm{D}}{\mathrm{D}t} = \frac{\partial}{\partial t} + u\frac{\partial}{\partial x} + v\frac{\partial}{\partial y} + w\frac{\partial}{\partial z}$$

is the material derivative that includes the temporal change and advection. In addition, the mass-continuity equation states

$$\frac{1}{\rho}\frac{\mathrm{D}\rho}{\mathrm{D}t} + \frac{\partial u}{\partial x} + \frac{\partial v}{\partial y} + \frac{\partial w}{\partial z} = 0, \tag{2.14}$$

and the thermodynamic equation is

$$\frac{\mathrm{D}\theta}{\mathrm{D}t} = Q, \tag{2.15}$$

where Q is an undetermined forcing and θ is the potential temperature. Eq. (2.15) may alternatively be written

$$c_p\frac{\mathrm{D}T}{\mathrm{D}t} - \frac{1}{\rho}\frac{\mathrm{D}p}{\mathrm{D}t} = Q \tag{2.16}$$

preferential if pressure and temperature derivatives are known. However, in modelling and theoretical work, the thermodynamic equation is often used in the form of Eq. (2.15).

Eqs. (2.11)-(2.15), together with the ideal gas law of Eq. (2.2) constitute the set of equations that fully describes the fluid flow in the inviscid atmosphere.

2.3.1 Boussinesq Approximation

The density is typically linearised in atmospheric modelling by the **Boussinesq approximation**. The essence of it is to ignore the variations of density in the horizontal momentum Eqs. (2.11)-(2.12), where the density is set to a reference value, typically the average density of the background, $\rho = \rho_0$. Thus, the density is broken up into

$$\rho = \rho_0 + \hat{\rho}(z) + \rho'(x, y, z, t) \equiv \rho_0 + \delta\rho(x, y, z, t) \tag{2.17}$$

with ρ_0 as the reference density at a reference altitude z_0. In the Boussinesq approximation, it is assumed that $|\hat{\rho}|$, $|\rho'|$, $|\delta\rho| << |\rho_0|$. Furthermore, for any differentiation with

respect to z, the density profile is assumed exponential when considering fluid motions within a density scale height $H = R_a T_0/g$ so that

$$\rho_0(z) = \rho_0(z_0)e^{-(z-z_0)/H}. \tag{2.18}$$

Most derivations of the atmospheric Boussinesq equations of motion would neglect the resulting terms stemming from the vertical differentiation of Eq. (2.18), thus not considering them necessary. However, as highlighted by Fritts & Alexander, including these terms yield interesting, slightly more general gravity wave solutions for large-scale waves [18].

Likewise, the pressure is also broken up to

$$p = p_0(z) + p'(x, y, z, t) \tag{2.19}$$

where it is assumed that $|p'| << |p_0|$.

When inserting Eq. (2.17) for ρ and Eq. (2.19) for p into Eqs. (2.11)-(2.12), neglecting small terms from the Boussinesq assumptions, yield the **Boussinesq horizontal momentum equations**

$$\frac{\partial u}{\partial t} + u\frac{\partial u}{\partial x} + v\frac{\partial u}{\partial y} + w\frac{\partial u}{\partial z} - fv + \frac{\partial}{\partial x}\left(\frac{p'}{\rho_0}\right) = X, \tag{2.20}$$

$$\frac{\partial v}{\partial t} + u\frac{\partial v}{\partial x} + v\frac{\partial v}{\partial y} + w\frac{\partial v}{\partial z} + fu + \frac{\partial}{\partial y}\left(\frac{p'}{\rho_0}\right) = Y. \tag{2.21}$$

These momentum equations are nonlinear due to the advection terms still present, highlighted by writing out the material derivative entirely.

For the z-momentum Eq. (2.13), small deviations of ρ must not be neglected when coupled with gravity. Eq. (2.13) can be multiplied by ρ of the form of Eq. (2.17). The variables in the second term differentiation of Eq. (2.13) are written in component form, where the differentiation of $p_0(z)$ is simply the hydrostatic Eq. (2.1), with density ρ_0. Then $\rho' g/\rho_0$ is the only remaining gravity term when dividing by $\rho \approx \rho_0$. The benefit of this approximation technique for the z-momentum equation is that gravity is coupled with the dimensionless density fluctuation parameter ρ'/ρ. The z-derivative of the density terms in the second term of the original z-momentum Eq. (2.13) is calculated using the exponential density within a scale height H, according to Eq. (2.18). Consequently, a term of p with a proportionality factor of $1/H$ appears in the derivation of Fritts & Alexander [18]. Neglecting the mean pressure term $p_0(z)/H$ due to the exclusion of background mean terms yields the **Boussinesq vertical momentum equation**

$$\frac{\partial w}{\partial t} + u\frac{\partial w}{\partial x} + v\frac{\partial w}{\partial y} + w\frac{\partial w}{\partial z} + \frac{\partial}{\partial z}\left(\frac{p'}{\rho_0}\right) - \frac{1}{H}\frac{p'}{\rho_0} + g\frac{\rho'}{\rho_0} = 0. \tag{2.22}$$

The continuity Eq. (2.14) decouples due to the Boussinesq assumptions, so that $\nabla \cdot \boldsymbol{V} = 0$, where $\boldsymbol{V}$ is the total velocity vector, and $\mathrm{D}\rho/\mathrm{D}t = 0$. Separated into two equations, with horizontal differentiation of ρ following the standard Boussinesq assumption

of Eq. (2.17), and letting the vertical differentiation be of the exponential density form of Eq. (2.18), yields the **Boussinesq continuity equations**

$$\frac{\partial}{\partial t}\left(\frac{\rho'}{\rho_0}\right) + u\frac{\partial}{\partial x}\left(\frac{\rho'}{\rho_0}\right) + v\frac{\partial}{\partial y}\left(\frac{\rho'}{\rho_0}\right) - \frac{w}{H} = 0 \tag{2.23}$$

$$\frac{\partial u}{\partial x} + \frac{\partial v}{\partial y} + \frac{\partial w}{\partial z} = 0. \tag{2.24}$$

The last term of Eq. (2.23) stems from the advection z-derivative term of ρ with the exponential density variation of Eq. (2.18) implemented.

The Boussinesq decomposition of θ follows the same strategy, so $\theta = \theta_0(z) + \delta\theta(x, y, z, t)$ and assuming $|\delta\theta| << |\theta_0|$, variations only in the z-direction and an exponential density form. The nonlinear **Boussinesq thermodynamic equation** is then found to be

$$\frac{\partial}{\partial t}\left(\frac{\theta'}{\theta_0}\right) + u\frac{\partial}{\partial x}\left(\frac{\theta'}{\theta_0}\right) + v\frac{\partial}{\partial y}\left(\frac{\theta'}{\theta_0}\right) + w\frac{N^2}{g} = Q, \tag{2.25}$$

where the last term stems from the z-derivative of θ and using Eq. (2.9) to relate this derivative with the Brunt-Väisälä frequency N.

2.3.2 Linearisation of Velocities & WKB Approximation

Several of the obtained equations, Eqs. (2.20), (2.21), (2.22), (2.23) and (2.25) are nonlinear Boussinesq equations due to advection terms. These may be solved iteratively in weather and climate models if fed with sufficient input measurements. However, simple analytic solutions can be found if further **linearisations** are applied, this time of the velocities. Velocities are broken into mean background winds U,V, and W, and turbulent velocity components u', v', and w' that are assumed small compared to the mean winds. Linearising about the hydrostatic state gives $W \approx 0$, so the mean vertical wind is neglected. Additionally, the horizontal mean velocities are assumed to be purely z-dependent, so the horizontal derivatives of U and V are zero. Furthermore, the terms of the mean velocities that do not contain any perturbed quantity, e.g. the Coriolis terms fV and fU, may be neglected. This is because only the perturbation momentum Eqs. relative to the background mean wind is of interest. Further linearisations of the resulting turbulent advection terms can be done. All quantities assumed to be small perturbations and that are quadratic, i.e., terms like $u'\partial\theta'/\partial x$, may be neglected in linear theory. In linear theory, any forcing X, Y, and Q are neglected.

In addition, by using the WKB approximation, the mean flow values, such as U and V, are assumed to vary slowly with z over a wave cycle, so that the w'-driven advection term of the horizontal momentum equations can be neglected. In addition, in the WKB approximation, the Brunt-Väisälä frequency N is assumed to be slowly varying over a wave cycle and thus approximated to be constant, as this will simplify the analytic calculations. However, it should be noted that N typically varies with altitude in the atmosphere, particularly in the stratosphere and mesosphere [56].

After reducing the nonlinear Boussinesq Eqs. (2.20), (2.21), (2.22), (2.23) and (2.25) by linearisation about the hydrostatic state and applying the WKB approximation, the final

linearised Boussinesq momentum equations become

$$\frac{\partial u'}{\partial t} + U\frac{\partial u'}{\partial x} + V\frac{\partial u'}{\partial y} - fv' + \frac{\partial}{\partial x}\left(\frac{p'}{\rho_0}\right) = 0, \tag{2.26}$$

$$\frac{\partial v'}{\partial t} + U\frac{\partial v'}{\partial x} + V\frac{\partial v'}{\partial y} + fu' + \frac{\partial}{\partial y}\left(\frac{p'}{\rho_0}\right) = 0, \tag{2.27}$$

$$\frac{\partial w'}{\partial t} + U\frac{\partial w'}{\partial x} + V\frac{\partial w'}{\partial y} + \frac{\partial}{\partial z}\left(\frac{p'}{\rho_0}\right) - \frac{1}{H}\frac{p'}{\rho_0} + g\frac{\rho'}{\rho_0} = 0. \tag{2.28}$$

The mass-continuity equations (2.23)-(2.24) become

$$\frac{\partial}{\partial t}\left(\frac{\rho'}{\rho_0}\right) + U\frac{\partial}{\partial x}\left(\frac{\rho'}{\rho_0}\right) + V\frac{\partial}{\partial y}\left(\frac{\rho'}{\rho_0}\right) - \frac{w'}{H} = 0. \tag{2.29}$$

$$\frac{\partial u'}{\partial x} + \frac{\partial v'}{\partial y} + \frac{\partial w'}{\partial z} = 0. \tag{2.30}$$

Furthermore, using the definition of the potential temperature given by (2.10), the thermodynamic equation (2.25) becomes

$$\frac{\partial}{\partial t}\left(\frac{\theta'}{\theta_0}\right) + U\frac{\partial}{\partial x}\left(\frac{\theta'}{\theta_0}\right) + V\frac{\partial}{\partial y}\left(\frac{\theta'}{\theta_0}\right) + w'\frac{N^2}{g} = 0. \tag{2.31}$$

Thus, Eqs. (2.26)-(2.31) are the fully **linearised Boussinesq equations** for atmospheric fluid flows. The benefit of all these approximations, compared to the raw Eqs. of motion (2.11)-(2.15), is that Eqs. (2.26)-(2.31) can be solved analytically, which will give insight into the characteristics of atmospheric GWs.

An additional Boussinesq-linearised version of the potential temperature equation (2.10) yields the relation between the potential temperature, pressure, and density variables as

$$\frac{\theta'}{\theta_0} = \frac{1}{c_s^2}\left(\frac{p'}{p_0}\right) - \frac{\rho'}{\rho_0}, \tag{2.32}$$

where c_s is the speed of sound in air [18]. The first term on the right-hand side includes acoustic waves in the atmosphere. However, acoustic waves are neglected for the remaining analysis by letting the acoustic term approach zero in the absence of acoustics. This yields a handy link between potential temperature and density coordinates that is useful as the scale height (and thus the validity) of θ is typically larger than that of ρ. For large-scale waves, the potential temperature formulation is preferred.

2.4 Plane Wave Solution and Dispersion Relations

By assuming plane wave solutions of the linearised Boussinesq Eqs. (2.26)-(2.31) for u', v', w', $\frac{\rho'}{\rho_0}$, $\frac{\theta'}{\theta_0}$ and $\frac{p'}{p_0}$, the waves can be expressed as

$$\left(u',\, v',\, w',\, \frac{\rho'}{\rho_0},\, \frac{\theta'}{\theta_0},\, \frac{p'}{p_0}\right) = (\tilde{u},\, \tilde{v},\, \tilde{w},\, \tilde{\rho},\, \tilde{\theta},\, \tilde{p}) \cdot \exp\left[i(kx + ly + mz - \omega t) + \frac{z}{2H}\right]. \tag{2.33}$$

Here $\tilde{u}$, $\tilde{v}$, $\tilde{w}$, $\tilde{\theta}$, $\tilde{p}$, and $\tilde{\rho}$ are complex wave coefficients, k, l and m are wave numbers in x, y and z directions respectively, and ω is the angular frequency of the wave as observed in a stationary frame of reference on the Earth's surface. However, it is convenient to introduce the intrinsic wave frequency, $\hat{\omega}$, as measured in the frame following the background wind motion, as

$$\hat{\omega} = \omega - kU - lV. \tag{2.34}$$

Inserting the plane wave solutions of Eq. (2.33) into the linearised Boussinesq Eqs. (2.26)-(2.31), in the intrinsic frame of reference, yields the set of equations for the wave coefficients as

$$-i\hat{\omega}\tilde{u} - f\tilde{v} + ik\tilde{p} = 0, \tag{2.35}$$

$$-i\hat{\omega}\tilde{v} + f\tilde{u} + il\tilde{p} = 0, \tag{2.36}$$

$$-i\hat{\omega}\tilde{w} + \left(im - \frac{1}{2H}\right)\tilde{p} + g\tilde{\rho} = 0, \tag{2.37}$$

$$-i\hat{\omega}\tilde{\theta} + \frac{N^2}{g}\tilde{w} = 0, \tag{2.38}$$

$$-i\hat{\omega}\tilde{\rho} + ik\tilde{u} + il\tilde{v} + \left(im - \frac{1}{2H}\right)\tilde{w} = 0. \tag{2.39}$$

In addition, Eq. (2.32) can be written as

$$\tilde{\theta} = \frac{\tilde{p}}{c_s^2} - \tilde{\rho}, \tag{2.40}$$

which for non-acoustic waves reduces to $\tilde{\theta} = -\tilde{\rho}$.

Solving the set of Eqs. (2.35)-(2.39) for the intrinsic frequency $\hat{\omega}$ yields the dispersion relation for the internal gravity waves

$$\hat{\omega}^2 = \frac{N^2(k^2+l^2) + f^2\left(m^2 + \frac{1}{4H^2}\right)}{k^2 + l^2 + m^2 + \frac{1}{4H^2}}, \tag{2.41}$$

which relates the wave frequency to the wavenumbers k, l, m, Coriolis parameter f, density scale height H and the Brunt-Väisälä frequency N.

The group velocity vector of the waves is found from the dispersion relation as it is defined as (note the use of ω instead of the intrinsic frequency, as the velocity components become dependent on the background wind)

$$\boldsymbol{c}_g = \left(\frac{\partial\omega}{\partial k}, \frac{\partial\omega}{\partial l}, \frac{\partial\omega}{\partial m}\right). \tag{2.42}$$

Thus, the components of the group velocity become

$$c_{gx} = U + \frac{k(N^2 - \hat{\omega}^2)}{\hat{\omega}\left(k^2 + l^2 + m^2 + \frac{1}{4H^2}\right)}, \tag{2.43}$$

$$c_{gy} = V + \frac{l(N^2 - \hat{\omega}^2)}{\hat{\omega}\left(k^2 + l^2 + m^2 + \frac{1}{4H^2}\right)}, \tag{2.44}$$

$$c_{gz} = \frac{-m(\hat{\omega}^2 - f^2)}{\hat{\omega}\left(k^2 + l^2 + m^2 + \frac{1}{4H^2}\right)}, \tag{2.45}$$

where m is assumed positive in downward direction, while k is positive for eastward wind and l positive northward.

Important relations between perturbation amplitudes can be derived from Eqs. (2.35)-(2.40). These are called polarisation relations and become

$$\tilde{u} = \left(\frac{i\hat{\omega}k - fl}{i\hat{\omega}l + fk}\right)\tilde{v}, \tag{2.46}$$

$$\tilde{p} = \left(\frac{\hat{\omega}^2 - f^2}{\hat{\omega}k + ifl}\right)\tilde{u} = \left(\frac{\hat{\omega}^2 - f^2}{\hat{\omega}l - ifk}\right)\tilde{v}, \tag{2.47}$$

$$\tilde{w} = \frac{\left(m - \frac{i}{2H}\right)\hat{\omega}}{N^2 - \hat{\omega}^2}\tilde{p}. \tag{2.48}$$

In addition, Eq. (2.38) relates $\tilde{\theta}$ to $\tilde{w}$, and Eq. (2.40) relates $\tilde{\theta}$ and $\tilde{\rho}$. The physical quantities can be obtained by only considering the real component.

2.4.1 Gravity Waves of High Frequencies and Small Wavelengths

For high-frequency waves with small vertical wavelengths of $\lambda_z < 30$ km, the correction term $1/4H^2$ in the dispersion relation (2.41) can be neglected since then $m^2 >> 1/4H^2$. Furthermore, the Coriolis parameter f can also be neglected if the waves have short periods (i.e. less than a day) or spatially small (i.e. less than 1000 km horizontal wavelengths). Then, the dispersion relation (2.41) for gravity waves reduces to

$$\hat{\omega}^2 = \frac{N^2(k^2 + l^2)}{k^2 + l^2 + m^2} \equiv N^2\cos^2(\alpha), \tag{2.49}$$

where α is the angle between the vertical and the wavefronts (or equivalently, the angle between the horizontal and wave vector). The intrinsic frequency can never be larger than the Brunt-Väisälä frequency, and $|\hat{\omega}| \leq |N|$. For small horizontal scales, i.e. $k^2 + l^2 >> m^2$, the intrinsic frequency approaches N from below, as the oscillation becomes purely vertical.

The phase speeds in each direction, as measured in the reference frame of the Earth (i.e. not intrinsic), are found to be

$$c_{px} = U + \frac{N\cos(\alpha)}{k}, \quad c_{py} = V + \frac{N\cos(\alpha)}{l}, \quad c_{pz} = \frac{N\cos(\alpha)}{m}. \tag{2.50}$$

The group velocity vector, as given in component form in Eqs. (2.43)-(2.45), becomes

$$\boldsymbol{c}_g = \left(U + \frac{Nm^2}{(k^2 + l^2 + m^2)^{3/2}},\, V + \frac{Nm^2}{(k^2 + l^2 + m^2)^{3/2}},\, \frac{-Nm\sqrt{k^2 + l^2}}{(k^2 + l^2 + m^2)^{3/2}}\right). \tag{2.51}$$

The group velocity vector is directed parallel to wavefronts and perpendicular to the total wave vector and the direction of phase propagation, as seen in Fig. 2.3. Note that since the wave source is typically topography, the wave group must propagate upwards. Thus, the vertical component of the group velocity must be positive. Therefore, for GWs generated in the troposphere from mountains or convective storms, the vertical wavenumber is defined as negative, i.e. $m < 0$. For an upward-propagating wave group, the wave phases move downward, since then $c_{pz} < 0$. Note that if $m = 0$, so that $\lambda_z \to \infty$, then wavefronts are vertical, and the vertical group velocity component is zero. This special case is called an evanescent GW since no wave energy is transported vertically, as it is carried by the group velocity.

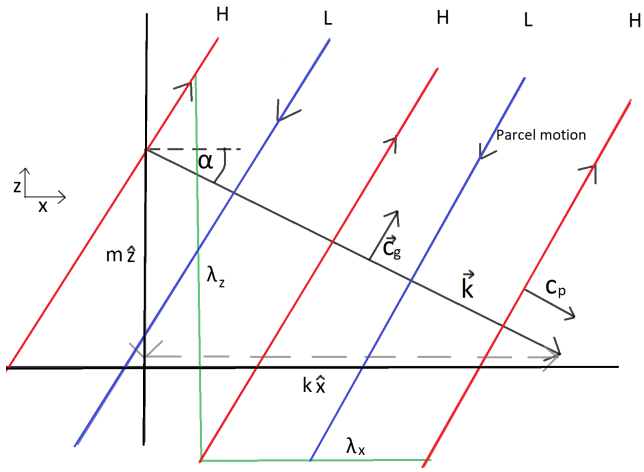

Figure 2.3: Illustration of wave fronts, wavelengths, wavenumbers, and phase and group velocities, with $l = 0$ for simplicity. Wavefronts of high (H) and low (L) pressures are formed with the wave vector $\boldsymbol{k}$ normal to the fronts, with an angle α with respect to the horizontal. Air parcels move along fronts according to arrows: up along high pressures and down along low pressures. The phases propagate along the wave vector, in this case slightly downward. Since $k > 0$ and $m < 0$ by definition, an upward group velocity carries energy and momentum upwards, parallel to wave fronts. An oppositely tilted wavefront is possible in which c_p is directed downwards since the group velocity is still supposed to have an upward component. Illustration made by the author.

2.4.2 Mountain Waves

The subset of GWs caused by winds over mountains are called mountain waves (MWs) and are a set of orographic GWs. They are often seen as stationary waves relative to the ground. Their relations are essentially the same as presented above, except that the intrinsic frequency (and thus their existence) is purely wind-dependent. Then $\omega = 0$ and the dispersion relation becomes

$$\hat{\omega} = -\boldsymbol{k} \cdot \boldsymbol{V} \tag{2.52}$$

Here $\boldsymbol{k}$ is the wave vector, and $\boldsymbol{V}$ is the total wind vector. Since the wave frequency must be positive, MWs can only exist in theory if $\boldsymbol{k}$ and $\boldsymbol{V}$ are antiparallel, i.e. phase

propagation into the wind. If, for example, the wind blows eastwards over a mountain, then MWs can only exist if their phase propagation relative to the wind is westwards while stationary relative to the ground. It should be noted that a constant wind is assumed, though this is not always the case as it may vary in time. The effect of a time-varying wind is a Doppler shift and apparent propagation of MWs relative to the ground. The group velocity is similar to the expression given in the previous subsection, following Eq. (2.51).

2.5 Energy Propagation and Dissipation of Gravity Waves

The dispersion relation follows Eq. (2.49) for waves of small vertical wavelengths. In this case, when combining the momentum, thermodynamic, and mass-continuity Eqs. (2.26)-(2.28), (2.30) and (2.31), this yields the **energy conservation equation** for the linearised Boussinesq-approximated fluid flow

$$\frac{\partial}{\partial t}\frac{1}{2}\rho_0\left[\boldsymbol{v}'^2+\left(\frac{g\rho'}{\rho_0 N}\right)^2\right]+\nabla\cdot(\boldsymbol{v}'p')=0. \tag{2.53}$$

Here, the velocity term inside the bracket with the preceding coefficients describes the kinetic energy per volume of fluid. In contrast, the last term in the bracket relates to the available potential energy (APE) of the parcel. The divergence term describes the **energy flux**, which if averaged over a wavelength, is defined as $\boldsymbol{\mathcal{F}}=\overline{\boldsymbol{v}'p'}$. It is positive and increases if energy (kinetic and APE) is pumped out of the system, and vice versa.

The energy density of a wave is equivalent to the wavelength-averaged mean perturbation energy per volume, written as

$$2\overline{E}=\overline{\boldsymbol{v}'^2}+\overline{\left(\frac{g\rho'}{\rho_0 N}\right)^2}. \tag{2.54}$$

Using the polarisation relations (2.46)-(2.48), the energy flux vector is found to be

$$\boldsymbol{\mathcal{F}}\equiv(\overline{u'p'},\,\overline{v'p'},\,\overline{w'p'})=\left(\frac{k}{\hat{\omega}},\,\frac{l}{\hat{\omega}},\,-\frac{k^2+l^2}{m\hat{\omega}}\right)\tilde{p}=\boldsymbol{c}_g\overline{E}. \tag{2.55}$$

The important consequence of Eq. (2.55) is that the wave energy flux is aligned with the group velocity, which is parallel to wavefronts, upwards from the wave sources. Energy is therefore carried upwards. Moreover, the energy flux can be shown to be related to the **momentum flux**, most useful for quantifying GW drag on the mean flow. The result is a vertical GW flux of horizontal momentum as

$$(F_{Px},\,F_{Py})=\rho_0 c_{gz}\frac{\overline{E}}{\hat{\omega}}(k,\,l). \tag{2.56}$$

It can be shown, by inserting the group velocity and energy, that the momentum flux components become related to the velocity fluctuations by the Reynolds stresses $\overline{u'w'}$ and $\overline{v'w'}$ as [18]

$$(F_{Px},\,F_{Py})=\rho_0(\overline{u'w'},\,\overline{v'w'}), \tag{2.57}$$

which can be shown to be related to the energy flux [16].

The horizontal **GW drag** on the mean flow is often described by

$$(\overline{X},\, \overline{Y}) = -\frac{\varepsilon}{\rho_0}\frac{\partial}{\partial z}(F_{px},\, F_{py}), \tag{2.58}$$

where $\overline{X}$ and $\overline{Y}$ are the wave-induced forces in the horizontal mean flow momentum Eqs. (equivalent to the RHS of Eqs. (2.11)-(2.12), but for the mean flow equations). Also, ε is the intermittency factor, which is often a crucial factor to determine for GW parameterisations in GCMs [16].

Eq. (2.58) states that for GWs to generate drag on the mean flow, the vertical flux of horizontal momentum must be positive and change with altitude. The vertical momentum flux is constant if there is no dissipation of GWs [18]. However, when GWs break, turbulent dissipation causes the momentum flux to change with altitude and thus generates GW drag on the mean flow.

If the momentum flux is positive upward, but dissipation forces act to reduce the flux, then the force decelerates the flow. Mean flow forcing by GWs can only be present if the vertical flux of the horizontal momentum changes with altitude, i.e., a dissipating force exists, or $U = c_{px}$ at a critical level.

Another way GWs deposit energy and momentum to the mean flow is by atmospheric or wave instabilities, such as GW breaking at high altitudes due to wave amplitudes growing large enough that nonlinearities cause the waves to break. Also, momentum deposition often happens around a critical level where the vertical wavelengths become too small and the vertical wavenumber m approaches infinity. The background horizontal mean flow $(U,\, V)$ causes a Doppler shift of the frequency, as accounted for by the introduction of $\hat{\omega}$ in Eq. (2.41). If, at a level, the background mean winds are large enough that the intrinsic frequency $\hat{\omega} = \omega - kU - lV$ becomes zero, then from evaluating the components of the group velocity of Eq. (2.51) becomes $\boldsymbol{C}_g = (U,\, V,\, 0)$. Thus, since energy is transported by the group velocity, no vertical energy and momentum fluxes are possible at the critical level. In this case, wave energy and momentum may easier dissipate due to dissipative forces having more time to act on the slowly-moving horizontal energy and momentum transport.

2.6 Planetary Waves

While the theory of gravity waves is thoroughly presented as this is the central topic, it is necessary to present and discuss other types of waves in the atmosphere, as these may interact with GWs. Generally, there are two central atmospheric waves in addition to GWs: Planetary waves (PWs) and atmospheric tidal waves. The latter type is only dominant in the upper mesosphere and up. Hence the tides are unimportant in the stratosphere, where the majority of the focus is in this thesis. On the other hand, PWs are the largest sources of stratospheric variability in winds and temperatures. Since this thesis revolves around the PW interactions with GWs in the middle atmosphere, these waves must be presented. In contrast to the GW theory, the description presented here is shorter, with only the essential background equations established. More detailed derivations can be found in more advanced texts such as Vallis [56] and Andrews [4] for PWs.

A key difference between the GWs and the PWs is their length scales. Spatially, the wave scales are typically classified by the **zonal wavenumber** (WN for short). It is defined as the number of wavelengths λ fitting around the globe zonally at a given latitude. Thus, WN1 corresponds to a wavelength of 360°, the largest wave scales, WN2 equals $\lambda = 180°$, i.e. two waves fit around the globe, while WN3 becomes $\lambda = 120°$, and so on. PWs have generally low wavenumbers, while short-scale GWs of wavelengths less than 1000 km, have high wavenumbers of 40 and above.

Planetary waves (PWs), sometimes called Rossby waves, are waves of much larger scales than that of small-scale GWs. These are not gravity waves since gravity does not act as the restoring force but are instead called inertia waves. These waves are driven by the variation of the Coriolis force. PWs typically have periods of 2-20 days and wavelengths of thousands of kilometres. In the troposphere, most PWs are in the range of zonal wavenumbers 1 to 10, meaning their wavelengths are generally from 4000 km and above. These are primary drivers of weather fronts in the troposphere, as illustrated in Fig. 2.4 with low-pressure systems in the troughs. Higher in the atmosphere, PWs cover primarily zonal wavenumbers 1 to 6.

The fundamental mechanism underlying PWs is the conservation of potential vorticity on the Coriolis β-plane. The β-plane is a linear approximation of the Coriolis parameter on a tangential plane due to variations of the latitudinal angle ϑ. The parameter becomes

$$f = 2\Omega \sin(\vartheta_0) + \frac{\partial f}{\partial y} y \equiv f_0 + \beta y, \tag{2.59}$$

where ϑ_0 is the latitude at which the β-plane is tangent to. For small-scale atmospheric motion, the variation of the latitudinal angle ϑ and therefore variation of f in the north-south, along y, is small enough that $f \approx f_0$ is approximately constant. However, for large-scale motions, such as PWs, the motion covers a large span of ϑ, and the Coriolis parameter cannot be approximated as a constant. Then, a β-plane approximation with a linear y-component as a correction term is a more suitable approximation.

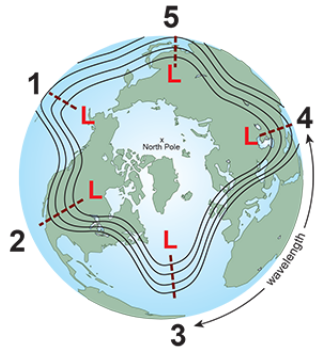

Figure 2.4: Illustration of zonal wavenumber 5 planetary waves propagating around the North Pole. Low-pressure systems are marked, illustrating the relation between PWs and weather systems in the troposphere. Illustration credit: National Weather Service [42].

Vorticity is a measure of the curl of the velocity field, or equivalently the local

rotation of the flow. For a 2D flow, the only nonzero component of the vorticity vector is the vertical component ζ_{rel}, defined as

$$\zeta_{\text{rel}} = \frac{\partial v}{\partial x} - \frac{\partial u}{\partial y} = \frac{\partial^2 \psi}{\partial x^2} + \frac{\partial^2 \psi}{\partial y^2}, \tag{2.60}$$

where u and v are the zonal and meridional velocities, and the last equivalence comes from the definition of the stream function as a function $\psi(x, y)$ such that

$$u = \frac{\partial \psi}{\partial y}, \quad v = -\frac{\partial \psi}{\partial x}. \tag{2.61}$$

However, ζ_{rel} is the relative vertical component of the vorticity in the frame of reference following the Earth's rotation. It is therefore convenient to introduce the absolute vorticity in the fixed frame of reference by including the β-plane Coriolis approximation to account for the rotational effects of the Earth, as

$$\begin{aligned} \zeta &\equiv f + \zeta_{\text{rel}} \\ &= f_0 + \beta y + \frac{\partial v}{\partial x} - \frac{\partial u}{\partial y} \\ &= f_0 + \beta y + \frac{\partial^2 \psi}{\partial x^2} + \frac{\partial^2 \psi}{\partial y^2}. \end{aligned} \tag{2.62}$$

The relevant quantities are now introduced, and the relevant equations for PWs can be derived. Following somewhat the derivation of Andrews [4], the horizontal momentum, thermodynamic, and continuity equations in this case are the so-called **quasi-geostrophic equations**,

$$\frac{\partial u_g}{\partial t} + u_g \frac{\partial u_g}{\partial x} + v_g \frac{\partial u_g}{\partial y} - f_0 v_a - \beta y v_g = 0, \tag{2.63}$$

$$\frac{\partial v_g}{\partial t} + u_g \frac{\partial v_g}{\partial x} + v_g \frac{\partial v_g}{\partial y} + f_0 u_a + \beta y u_g = 0, \tag{2.64}$$

$$\frac{\partial \rho'}{\partial t} + u_g \frac{\partial \rho'}{\partial x} + v_g \frac{\partial \rho'}{\partial y} - N^2 \frac{\rho_0 w_a}{g} = 0, \tag{2.65}$$

$$\frac{\partial u_a}{\partial x} + \frac{\partial v_a}{\partial y} + \frac{\partial w_a}{\partial z} = 0. \tag{2.66}$$

Here, geostrophic flow is assumed, so the pressure gradient and Coriolis force balance give the geostrophic velocities u_g and v_g (while the vertical is negligible). The deviation from geostrophy is noted as the ageostrophic velocities

$$u_a \equiv u - u_g, \quad v_a \equiv v - v_g, \quad w_a \equiv w. \tag{2.67}$$

Note that due to the assumption of hydrostatic balance and the underlying Boussinesq approximations mentioned in Section 2.3.1 for GWs, Eq. (2.65) is the quasi-geostrophic version of the Boussinesq thermodynamic equation. It therefore contains the Brunt-Väisälä frequency N and the density fluctuation ρ', similarly to Eq. (2.31). The quasi-geostrophic

equations are valid for describing large-scale and low-frequency motion in the atmosphere, thus ideal as a starting point for modelling PWs.

By taking the x-derivative of Eq. (2.64), subtract the y-derivative of Eq. (2.63) and use the mass-continuity Eq. (2.66), the vorticity equation can be found as

$$\frac{\partial \zeta}{\partial t} + u_g \frac{\partial \zeta}{\partial x} + v_g \frac{\partial \zeta}{\partial y} = f_0 \frac{\partial w_a}{\partial z}. \tag{2.68}$$

This equation expresses the relation between the vertical velocity and the vorticity. The right-hand term is known as the stretching term since it implies that an increase in vertical velocity produces vertical stretching and horizontal compression so that the vorticity increases. Expressing the vertical velocity by using Eq. (2.65), the vorticity Eq. (2.68) becomes the **quasi-geostrophic potential vorticity equation**

$$\frac{\partial q}{\partial t} + u_g \frac{\partial q}{\partial x} + v_g \frac{\partial q}{\partial y} = 0. \tag{2.69}$$

Here, q is the potential vorticity in a continuously stratified system and is given by

$$q \equiv \zeta + \frac{\partial}{\partial z}\left(\frac{f_0^2}{N^2}\frac{\partial \psi}{\partial z}\right), \tag{2.70}$$

and is a crucial quantity in describing PWs. This is because Eq. (2.69) is the central equation underlying PWs (since this is valid for large-scale and low-frequency fluid flows) and states that the potential vorticity is a conserved quantity.

The vorticity concept of PWs is considered in Fig. 2.5. Along a fixed latitude, marked by the dark horizontal line, the fluid flow is perturbed to an initial waveform in the y-direction (north-south) marked as $\eta(t = 0)$. Because of the conservation of potential vorticity, q as given in Eq. (2.72) in the quasi-geostrophic case, then q must be the same everywhere along the wave. For the simplest case of barotropic flow, the potential vorticity is equal to the absolute vorticity ζ as given by Eq. (2.62). Thus, for a displacement northward, the βy term from the Coriolis effect in the absolute vorticity increases, and so the relative vorticity in the frame of the rotating Earth must be negative, $\zeta_{\text{rel}} < 0$. This corresponds to a clockwise rotation of the fluid, as seen in Fig. 2.5. On the other hand, for southward displacement, the opposite occurs, and the relative vorticity must be positive, so $\zeta_{\text{rel}} > 0$, and the fluid rotation is anticlockwise. The effect of the relative vorticity is that it causes a velocity field to set up that causes each fluid parcel to move either northwards or southwards. This causes the wave phase to move westward relative to the mean wind flow. However, eastward propagating wave groups may occur for certain wavenumbers.

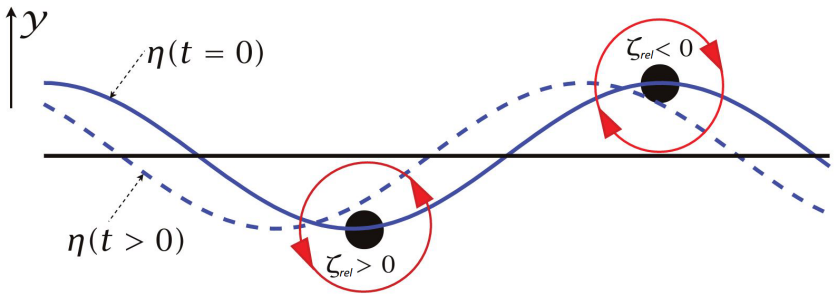

Figure 2.5: An illustration of a horizontal planetary wave in light of potential vorticity conservation, in the simple case of barotropic flow, where $q \approx \zeta$. An initial air parcel displacement initiates the wave marked by $\eta(t = 0)$. Due to the conservation of potential vorticity q, a northward displacement causes negative relative vorticity ζ_{rel} and vice versa. This causes the fluid parcels to move up/down with the rotation, and the wave phase propagates westwards. Image credit: Geoffrey Vallis [56].

Now, assume a background mean flow U in the x-direction and consider small perturbations from equilibrium for ψ as

$$\psi = -Uy + \psi'. \tag{2.71}$$

If inserted into the quasi-geostrophic potential vorticity equation, Eq. (2.69), with a linearisation that neglects nonlinear orders of ψ', the result is

$$\left[\frac{\partial}{\partial t} + U\frac{\partial}{\partial x}\right]\left[\frac{\partial^2}{\partial x^2} + \frac{\partial^2}{\partial y^2} + \frac{\partial}{\partial z}\left(\frac{f_0^2}{N^2}\frac{\partial}{\partial z}\right)\right]\psi' + \beta\frac{\partial \psi'}{\partial x} = 0. \tag{2.72}$$

As for the case with GWs, the Brunt-Väisälä frequency, N, is assumed constant to look for simple plane-wave solutions for the waves in focus. The wave is such that

$$\psi' = \tilde{\psi} \cdot \exp[i(kx + ly + mz - \omega t)], \tag{2.73}$$

where, as with GWs, k, l, m are the wavenumbers and ω the wave frequency. It can be shown that the dispersion relation for PWs using this plane-wave solution is

$$\omega = kU - \frac{\beta k}{k^2 + l^2 + f_0^2 m^2/N^2}. \tag{2.74}$$

The horizontal phase velocity can then be found from the dispersion relation, as

$$c_{px} = U - \frac{\beta}{k^2 + l^2 + f_0^2 m^2/N^2}, \quad c_{py} = \frac{kU}{l} - \frac{\beta k}{l(k^2 + l^2 + f_0^2 m^2/N^2)}. \tag{2.75}$$

Furthermore, the group velocity can be found in the same manner as for GWs. The components of the PW group velocity are then

$$\begin{aligned} c_{gx} &= U + \frac{\beta(k^2 - l^2 - f_0^2 m^2/N^2)}{(k^2 + l^2 + f_0^2 m^2/N^2)^2}, \\ c_{gy} &= \frac{2\beta kl}{(k^2 + l^2 + f_0^2 m^2/N^2)^2}, \\ c_{gz} &= \frac{2f_0^2 \beta km}{N^2(k^2 + l^2 + f_0^2 m^2/N^2)^2}. \end{aligned} \tag{2.76}$$

The PW characteristics can be analysed now that the PW dispersion relation, phase velocities, and group velocities are derived. First, the importance of the β-plane approximation is evident from the dispersion relation, where $\beta = 0$ yields a dispersion with the wind, with no intrinsic wave frequency (i.e. no wave relative to the wind). It is seen that the phase velocities of Eq. (2.75) reduce to the mean wind velocities, and likewise for the group velocity of Eq. (2.76). Thus, PWs cannot exist in small scales where the Coriolis term is constant or the Rossby number is large enough that Coriolis is neglected after all.

Since β from Eq. (2.59) is a term dependent on positive constants and $\cos(\vartheta_0)$, which is positive for $\vartheta \in (-90°,\, 90°)$, then $\beta > 0$. This implies that $U > c_{px}$ so that the wave phases move westward relative to the eastward mean flow. This does not necessarily mean that the PW phases move westward relative to the ground. With no background wind, the crests and troughs still move westward (negative x-direction) due to the β term. For vertical phase propagation, m^2 must be positive so that m is real. Since $U - c_{px} > 0$, then vertical phase propagation must imply that

$$U - c < U_c \equiv \frac{\beta}{k^2 + l^2}, \tag{2.77}$$

where U_c is the critical difference at which $m \to 0$ (infinite vertical wavelength, i.e. phase lines standing vertically). As long as Eq. (2.77) is met, the PWs will have a vertical phase propagation. Another consequence of Eq. (2.77) is that stationary PWs, relative to the ground, i.e. $c_{px} = 0$, implies that only an eastward wind less than the critical value, $0 < U < U_c$, can cause upward phase propagation.

PWs may propagate momentum and energy upwards in a similar way as GWs. For an upward propagating momentum flux, $m > 0$ and $k > 0$ by convention (for PWs). Then c_{gz} from Eq. (2.76) is positive, meaning upward group velocity. The phase fronts for upward propagating PWs should slope westward in the vertical, particularly in the stratosphere. Energy and momentum may thus be transported vertically and deposited if frictional forces from the turbulence caused by wave-breaking acts. Therefore, the PWs may affect the mean flow and other waves, such as GWs and tides.

Chapter 3

Methodology

This chapter contains a description of some methods and details for how the analysis of the dataset has been done. It starts with describing the WACCM model in more detail than presented in the introduction. Then, the data structure of the model simulation files is described, as they are NetCDF files containing different variables that need an introduction. As these variables, e.g. temperature must be filtered to yield isolated GWs, PWs, and mean wind, a thorough description of the filtering scheme is presented in Section 3.3.4. Then comes a short presentation of how the spatial GW power density spectrum is calculated, and how a zonal GW power can be derived from this. Lastly, the temporal power density spectrum is presented using the Generalised Lomb-Scargle periodogram and significance levels.

3.1 Whole Atmosphere Community Climate Model (WACCM)

The Whole Atmospheric Community Climate Model (WACCM) is an atmospheric General Circulation Model that is provided by the American National Center for Atmospheric Research (NCAR) [31]. Since its initial development at the beginning of the millennium, it has been a widely used model for studying the atmosphere from a modelling approach. The model combines elements from the upper atmospheric modelling of the High-Altitude Observatory (HAO), the middle atmosphere chemistry and dynamical modelling of the Atmospheric Chemistry Observation and Modeling (ACOM), and the tropospheric Climate and Global Dynamics (CGD) models. These are all unified into a single numerical model, WACCM, with the framework built around NCAR's Community Earth System Model (CESM). As the model is continuously expanded and improved, it can currently simulate the complex interactions and phenomena in the atmosphere to reasonably high detail given computational and physical constraints.

The specific model used in this thesis is the thermosphere- and ionosphere-extended WACCM version X, or WACCM-X for short. It is a component of the NCAR CESM version 1. It has physics version 5 of the Community Atmosphere Model implemented [41]. The dynamical core, i.e. the mathematical method for modelling the large-scale dynamics

of air and thermodynamics, is the continuous Galerkin spectral finite element method. This is the first dynamical core where energy and the 2D potential vorticity, important for PWs, are locally conserved. WACCM-X models waves, tides, tropospheric weather, middle atmosphere events, seasonal variations in the atmosphere, and the transport and chemistry of human-caused trace gases. Deep convection, known to excite GWs, is parameterised and modified to account for momentum transport and plume dilution [32].

The grid is a spherical cubic which is advantageous for the dynamical core used. That is because it results in a quasi-uniform grid that does not require a polar filter on small-scale GWs unnecessarily and incorrectly resolved in high latitudes [32] [41]. This iteration of WACCM-X is a high-resolution model. The horizontal resolution zonally and meridionally is $0.25°$. That is significantly higher resolving than the standard WACCM-X. This is why the high-resolution model is preferred in this GW study, as it can resolve more waves. Also, WACCM-X is the first version where the model couples the middle- and upper-atmosphere, with an upper altitude limit of around 500-700 km. This enables the study of the wave interactions from the troposphere and middle atmosphere, to the upper atmosphere. The vertical resolution varies with altitude. It is set to between 0.016 to 0.06 times the scale height below 40 hPa ($\sim$ 21 km), ranging from 0.1 to 0.5 km since this region's scale height is relatively constant of about 7-8 km. Above 40 hPa, the vertical resolution is 0.1 times the scale height.

The data studied in this project is a month-long NH winter period from 13$^{\text{th}}$ January to 12$^{\text{th}}$ February with 6-hourly data from the WACCM-X simulation provided by NCAR. The data is open-source and has been downloaded from Globus Shared Endpoint [40]. Temperatures, zonal and meridional winds, as well as pressures and vertical velocities, are included in the data. However, for GW perturbations only the temperature data is used in this thesis, while the horizontal wind is relevant for the vortex analysis and PWs. The simulation is a climatological realisation of general atmospheric conditions in January and February and is thus not actual weather data.

3.1.1 Gravity Wave Modelling in WACCM-X

WACCM-X uses a comprehensive parameterisation scheme for GWs that takes into account the generation, propagation, and dissipation of these waves in the Earth's atmosphere. GWs larger than the grid resolution are realised directly from the dynamics and physics of the model, and resolved properly. For the high-resolution model, more waves are realised than before. Small-scale GWs from orography, on the other hand, are parameterised according to the orography of the grid cells. The GW parameterisation scheme is implemented using a spectral method, where discrete waves with different frequencies and horizontal scales are launched from sources, determined by specific atmospheric conditions. The scheme includes several physical processes that contribute to the generation of gravity waves, such as orographic forcing, convective processes, and frontal systems. It also includes processes that lead to the dissipation of gravity waves, such as wave breaking due to turbulence and the effects of atmospheric damping. The source function for orographic GWs is primarily modelled by using the method of McFarlane [37]. The wave saturation condition, e.g. instability and wave breaking at high altitudes and critical levels, is modelled by combining Lindzen's [28] and McFarlane's parameterisations [41]. However, in this parameterisation, as with the expression for GW drag in Eq. (2.58), an intermittency

factor ε is included, which must be set using observations. The intermittency is a measure of how often GWs appear in a specific location. A high ε-factor indicates frequent GW activity. Non-orographic GWs are, on the other hand, modelled by using specific trigger functions, one for convective heat release, and another so-called ”frontogenesis function” for frontal generation [41]. The latter diagnoses strong temperature and wind gradients and launches GWs from these if conditions for non-orographic wave generation are met. This is a significant reason for using WACCM-X in studying non-orographic GWs, as this feature is not present in all GCMs.

The parameterisation scheme in WACCM-X is designed to capture the complex interactions between GWs and the larger-scale atmospheric circulation and to provide an accurate representation of the spatial and temporal variability of these waves. This allows the model to simulate the behaviour of the Earth's atmosphere over a wide range of scales, from the global circulation down to the small-scale GWs.

3.2 Data Structure

The WACCM-X simulation data is stored in the Network Common Data Form (NetCDF) data structure. This structure is widely used in geophysical research for storing data on a global 3D spatial grid in time. NetCDF is a product of the UCAR Unidata Program developed in the 1980s [55]. The version used here is the NetCDF 4.0 from 2008, which stores the files in the Hierarchical Data Format (HDF5), which easily enables the storage of large data sets. Though the files here are large, with about 15 GB per time step worth of data, handling NetCDF data in e.g. Python is efficient as not the whole file is read and used simultaneously. In this case, the Python package 'NetCDF4' is used to read and load the files [19].

Each NetCDF file has three major constituents: metadata, dimensions, and variables. The file has metadata that describes the file content, e.g. headers for each variable, title, creator, etc. The metadata also shows the data dimensions for all variables, meaning the size of the multidimensional arrays containing the variables. The variables can be temperature, wind, and pressure, where each is stored in an array of its given dimension, given by the coordinates. Coordinates are latitude, longitude, altitude and time. The arrays are only accessed by passing a variable-specific key. Thus, the variables are only loaded to NumPy arrays when the key is called and is not using significant RAM storage otherwise. When handling large multidimensional arrays, such as the 4-dimensional temperature array in space and time, memory error and leakage may occur if not handled properly. Thus, when using the temperature field here, the array is copied a minimum amount and all unnecessary arrays are deleted from the RAM when used. This is particularly relevant in time filtering, where a temperature array of 3 dimensions (a chosen 2D spatial plane, plus the full-time interval) is used. It should be noted that the computer power used for this project has been a standard 8 GB RAM, intel Core i5 computer. Hence, this restricts the data analysis because it takes more time and limits the computational power.

The variables, coordinates, keywords, and dimensions of the NetCDF files considered here, are presented in Table 3.1. Each NetCDF file contains a single time step worth of data, and there are four files/time steps per day since the time resolution is 6 hours. The total number of files/time steps are thus 124 for the 31-day dataset. The coordinates

Table 3.1: Table of variables and dimensions in each NetCDF file as provided by NCAR.

Keyname	Type	Description	Dependence	Dimension	Unit
time	coord	Time	-	1	hours
lev	coord	Pressure altitude	-	273	hPa
lat	coord	Latitude	-	721	°N
lon	coord	Longitude	-	1440	°E
T	var	Temperature field	time, lev, lat, lon	$1 \times 273 \times 721 \times 1440$	K
U	var	Zonal wind	time, lev, lat, lon	$1 \times 273 \times 721 \times 1440$	m/s
V	var	Meridional wind	time, lev, lat, lon	$1 \times 273 \times 721 \times 1440$	m/s
OMEGA	var	Vertical wind	time, lev, lat, lon	$1 \times 273 \times 721 \times 1440$	Pa/s

for latitude, longitude, and altitude are all one-dimensional arrays. There are in total 721 latitudes from $-90°$ to $90°$ with a resolution of $0.25° \approx 28$ km. There are 1440 longitudes from $0°$ to $360°$ with a resolution of $\sim 0.25°$, which at the equator equals about 28 km, but shorter the higher the latitude. Vertically, there are 273 altitude levels, in the coordinate with key 'lev', given in pressure coordinates in hPa, which decreases with altitude. The range is approximately from ground to 500-700 km when transformed to the metric altitude. The vertical resolution is variable.

Temperature and all three wind components are 4-dimensional fields that depend on time, altitude level, latitude, and longitude. Thus there is one 3D spatial temperature field per time step, and likewise for wind. The total NetCDF temperature and wind variables are of size $1 \times 273 \times 721 \times 1440 \approx 2.8 \cdot 10^8$ elements. Additionally, there is one file per time step, meaning 124 such files for the whole month-long data set. Loading this directly to a NumPy array is therefore memory heavy. However, a 2D spatial slice in time is workable, though arrays should be deleted when their purpose is done to avoid memory leakage. The 2D slices considered here will be horizontal slices at a constant altitude level, a zonal-vertical slice along a constant latitude, or a meridional-vertical slice along a constant longitude.

3.3 Wave Filtering

The raw temperature data extracted from the NetCDF files show the result of dynamics on widely different scales simultaneously. To distinguish the separate wave dynamics in the atmosphere, a series of filtering processes should be done. Then the GWs and PWs can be analysed separately. This follows the filtering methods developed in the pre-thesis project report leading up to this thesis, although the methods here are slightly modified [38]. In that, the atmospheric tides are also filtered. Hence, though these will not be in focus for this thesis, they are included in the filtering scheme that was developed.

3.3.1 Temporal and Spatial Wave Distributions

GWs, PWs, and tides can be separated by exploiting their different time and length scales. An illustration showing the distribution of wavelengths and periods for different wave

components is shown in Fig. 3.1, with GWs in blue, MWs (orographic GWs) in green, tides in red, and PWs in yellow-brown.

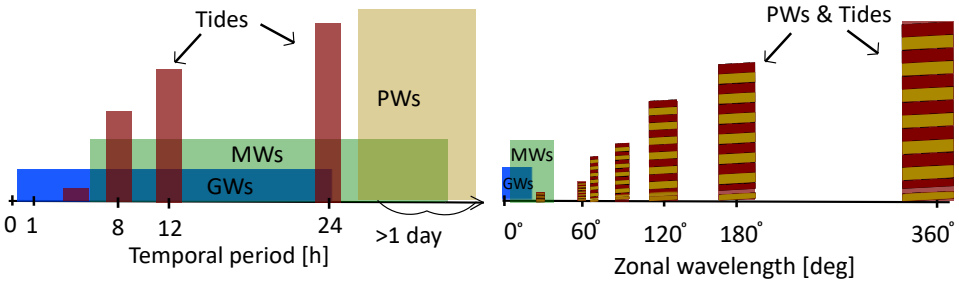

Figure 3.1: Sketch showing wave distributions in space and time. Left: the distribution of temporal wave periods is shown. Right: the distribution of zonal wavelengths is sketched for different wave types. These sketches illustrate the spatial and temporal characteristics of the different atmospheric waves, which may be utilised when isolating each wave by filter schemes. Different heights are used for illustrative purposes. However, for tides and PWs, the figure height also indicates what components are important relative to each other. Figure made by the author.

Spatially, the wave scales are classified by their zonal wavenumbers, or equivalently their wavelengths. As seen to the right in Fig. 3.1, there are three large wave components discretely distributed at WN1, WN2, and WN3 (these are in reality continuously distributed in a small interval around these wavelengths). These are predominantly components of PWs and tides, which are primarily large spatial-scale waves. They also have some components at higher WNs, but typically smaller amplitudes, although this depends on altitude and latitude. Above WN6, these are typically insignificant, apart from PWs having scales down to WN10 (36°) in the troposphere. GWs, on the other hand, are typically spatially small-scale waves. They rarely reach wavelengths longer than 1000 km and are of zonal wavenumbers higher than around WN25 (14°), but typically much higher than this. Since the GW sources are of vastly different scales (from mountains to wind jets and storm systems), their spatial wavenumber distribution in the atmosphere is a continuous spectrum from hundred meters to 1000 km in wavelengths. These are the smallest waves of importance in large-scale atmospheric circulation. Similarly, the MWs, which are special cases of GWs past orography, may be even longer and larger. However, they are small-scale in comparison to the tidal and PW components. In this regard, GWs and MWs will be considered as one ”small-scale wave” signal in the following filtering, in contrast to the method in the previous project report where they were separately analysed.

Temporally, there is a similar wave period distribution, as seen to the right in Fig. 3.1. Non-stationary GWs have periods ranging from 5 minutes (Brunt-Väisälä period) to 24 hours, as a continuous distribution (again, due to the multitude of wave sources). On the other hand, the MWs remain relatively stationary above mountainous regions with periods in the range from 4-5 hours to longer than 24 hours. Even more stationary, with periods of 2-20 days, are the PWs, on the far end of the spectrum. Lastly, the tides are discretely distributed mainly at 24 hours (diurnal tide), 12 hours (semidiurnal tide) and 8 hours (terdiurnal tide) components.

3.3.2 Time Filtering Using Digital IIR Filter

A digital Infinite Impulse Response (IIR) filter scheme can be applied for temporal filtering. This is suitable for signals that are linear and time-invariant. The temperature and wind time series at each grid point in the WACCM simulation data are linear time-invariant series. Thus an IIR filter can be used, such as the Butterworth filter.

To extract temporal wave components of specific frequencies of the time series at each grid point, a bandpass IIR filter can be applied. The filter is designed by using the *scipy.signal* package in Python [50]. First, the Butterworth IIR filter is extracted from SciPy by using *scipy.signal.iirfilter*. It is applied as a bandpass filter of frequencies in a range around a desired frequency. The order of the Butterworth filter is chosen to be 25, as this was found to be a high enough order to yield acceptable amplitudes without causing too long runtimes. In general, the higher order, the more data points are used to calculate the coefficients for the output signal, and thus the more accurate the output. With order 25, the deviation from e.g. order 48 was not significant. The effect of the order choice is presented in Fig. 3.2, where the highest order chosen has much stronger dampening over a shorter frequency interval around the cutoff frequency. The figure presents a lowpass filter since low-frequency amplitudes are passed while high-frequency amplitudes above the cutoff are dampened to zero amplitude. However, the Butterworth IIR filter can similarly work as a highpass filer, with the graph in Fig. 3.2 reversed about the cutoff frequency. Lastly, a bandpass filter would have two cutoff frequencies and only pass the interval in between.

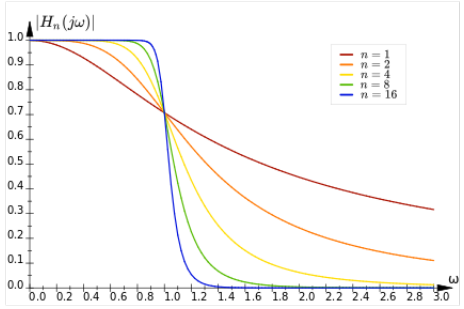

Figure 3.2: An illustration of the lowpass Butterworth filter for different orders n. A bandpass filter is designed by combining the lowpass and highpass filters. Illustration credit: Pieter P [45]

The output of the SciPy Butterworth filter is the cascaded Second Order Coefficients (SOS) of the filter, which is then applied to the data using the *scipy.filter.sosfiltfilt* function to yield the final bandpass filtered output of the chosen frequency range [51]. The benefit of using the sosfiltfilt function is that it applies the filter both forwards and backwards to correct for the inevitable phase shift caused by the initial Butterworth filter. Thus, the output is not phase-shifted. Furthermore, the data should span over as long time as possible for the filter to yield appropriate sinusoidal outputs without significant end effects such as decreased amplitudes. The data input for the filter is therefore the full-time range of the data set all at once, i.e. the full 31-day interval.

3.3.3 Spatial Filtering Using Median Filter

For spatial filtering, a median filter is applied. This acts as a spatial lowpass filter, passing low wavenumbers (long wavelengths/large scales) in a 2D plane image. Thus, the filter is only applied to a predetermined plane of interest, and only one frame at a time. The median filter replaces the value at a specific point on a grid with the median value of the data within a rectangle window of a selected scale. When repeated for all grid points in the 2D plane/image, the result is a "smoothed-out" image. The small scale details of smaller scales than the chosen rectangular window are then lost, while the scales larger than the chosen rectangle remain. The filter method is shown in Fig. 3.3.

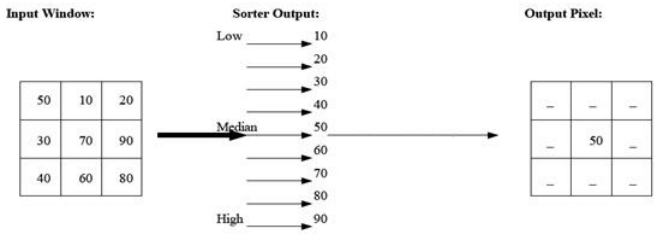

Figure 3.3: A sketch showing the median filter method for a grid point, here with a 3×3 rectangular filter scale. Illustration credit: Benjamin Weyori [8].

Since this is a lowpass filter, it is ideal for distinguishing small-scale and large-scale spatial structures in both vertical and horizontal planes. The median filter used is the *scipy.ndimage.median-filter* in Python [49]. The zonal scale of the rectangle is set to half of the cutoff zonal wavelength, so that for example for WN1, one peak and one trough fit around a latitude. In the horizontal plane, the meridional scale of the rectangle is set to $\sim 10°$, to ensure small-scale meridional wave structures are not passed. In the vertical-zonal plot, the vertical scale is set to a fixed value of 11 grid points, or about 2-5 km. Furthermore, to account for boundary points, where the filter rectangle encounters grid points outside of the boundary, a wrapping of the image is applied by the filter function parameters. This is to ensure that the filter considers that the map is zonally connected at the zonal ends.

3.3.4 Wave Separation Filter Scheme

The full filtering scheme, from raw temperature data to separated wave components, is schematically illustrated in Fig. 3.4. It is described in detail in the following.

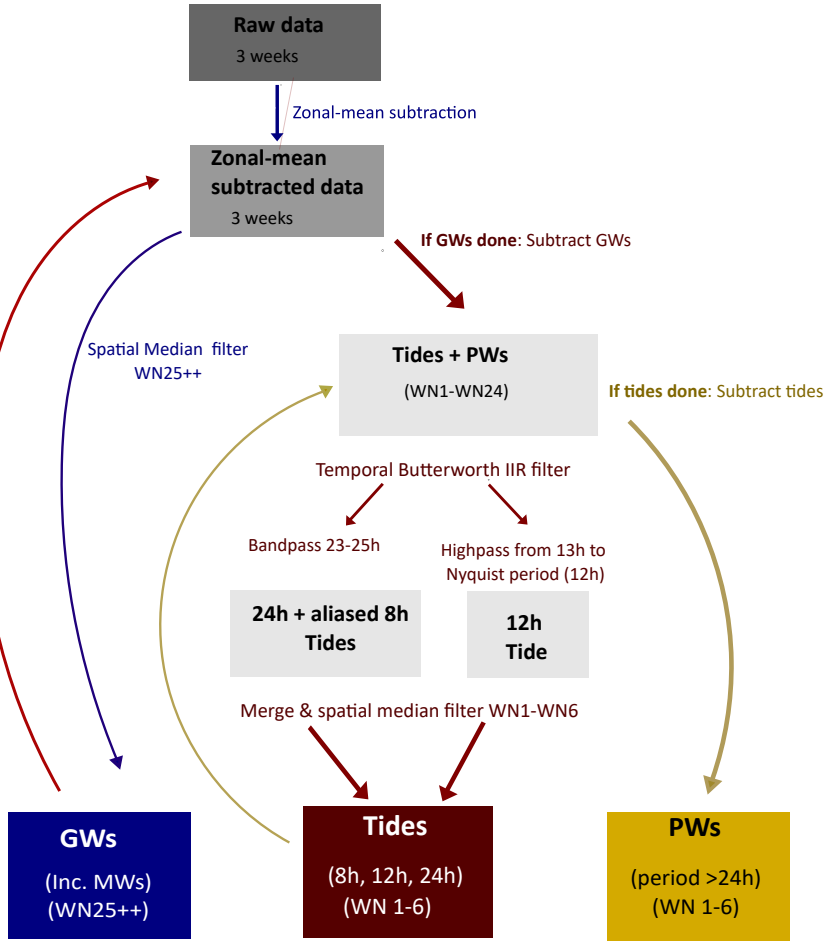

Figure 3.4: Flow chart of the process of wave filtering from raw temperature data to separated wave components. First, all small-scale waves that could only be attributed to GWs and MWs, are separated by a spatial median filter following the blue colour scheme. This includes all GWs and MWs from WN25 (roughly 1000 km wavelength) and up (down in wavelength). Then tides are separated by following the red path, using temporal filtering of the diurnal and semidiurnal components (including an aliased terdiurnal component with the diurnal signal), and spatial filtering to isolate WN1-6. Lastly, the PWs are separated following the yellow path, with an additional lowpass filtering to ensure only long periods are passed. Illustration made by the author.

Since GWs, PWs, and tides can be observed as perturbations in the background average temperature/wind, the first step to isolate these is to subtract the background average quantities. The **zonal mean temperature/wind** is found by averaging all temperatures/winds along a given latitude for a given time. This gives the average temperature/wind along a latitude and accounts for the seasonal changing background temperature since the major source of variability of the zonal mean is the seasons (e.g. NH troposphere is generally colder than the southern in January, and vice versa in July). This zonal mean

quantity is the background state, and if the variable is wind (either zonal or meridional), this is what is known as the **zonal mean wind** or **background wind flow**.

If the zonal mean quantities are subtracted from the raw data at each grid point for each latitude and altitude, the temperature/wind fluctuations from the mean remain. The filtering by **zonal mean subtraction** highlights the waves, though still superimposed on each other. The result is shown on the right-hand side of Fig. 3.5. The richness of time and length scale temperature variability is enhanced, as seen for example in wave structures in the zonal-vertical plot in the lower right. Here, some large-scale WN1 PWs are seen in the stratosphere, and vertically-standing GWs are also largely present. Similarly, the horizontal plot at 50 km reveals large WN1 PWs in the NH.

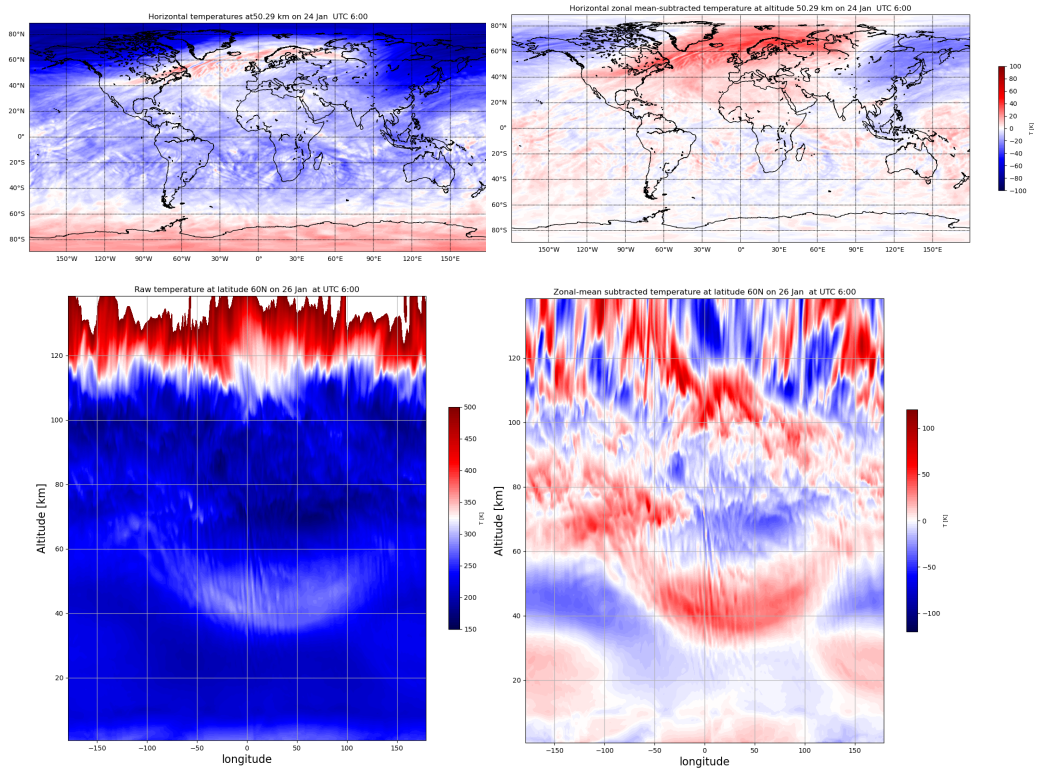

Figure 3.5: The effect of zonal mean subtraction. The raw temperature data is shown in the left images, and the corresponding zonal mean subtracted data is shown on the right. The upper images show horizontal planes at 50 km and lower a zonal-vertical cross-section at 60°N. This reveals hidden temperature perturbations to some extent.

The zonal mean subtracted data still contains structures of different lengths and time scales, with superimposed GWs, PWs, and tides. The first step is therefore to exploit the large spatial separation of GWs+MWs from the PWs and tides, as seen in Fig. 3.1. Here, GWs and MWs are treated as one merged GW signal, containing both orographic and non-orographic waves. By using the median filter with a zonal wavenumber cutoff at WN25,

the small-scale GWs (including MWs) of wavenumbers 25 and higher ($\lambda < 1000$ km) are separated from the large-scales (PWs + tides + other waves in between). Hence, GWs should be isolated and ready for separate analysis.

The remaining signal contains PWs, tides, and any residual signal of larger scales than 1000 km zonal wavelengths (WN1-WN24). The next step is then to isolate the tides. From Fig. 3.1 it is clear that they are most easily separated from PWs by their temporal distribution. Hence, a bandpass filter is constructed by applying a highpass followed by a lowpass digital IIR filter. With cutoffs at periods 23h and 25h, the combined diurnal (24h) and aliased terdiurnal (8h) tides are isolated. The aliasing occurs as a 6h resolution does not temporarily resolve 8h waves, so any 8h variation signal will be inseparable from the 24h variation. The semidiurnal (12h) component is separated by a highpass filtering at 13h down to the Nyquist period (12h). In the end, the total significant tidal signal is found when combining the filtered signals, and using the median filter only to pass the significant WN1-WN6.

Lastly, the PWs may be separated by subtracting the tides and GWs. However, some residual, high-frequency, and medium-wavenumber (WN10-WN24) signals remain. Since PWs in most of the atmosphere are primarily of WN6 or lower (WN10 or lower in the troposphere), a median filter is applied to isolate the WN1-WN6 PWs. Furthermore, since PW periods range from 2 to 20 days, the temporal lowpass IIR filter with a cutoff at 30h (1.25 days) is applied. Hence, the end result should be the isolated WN1-WN6 PWs in the atmosphere. Note that for the purpose of this thesis, the tidal isolation could have been omitted, and the PWs could be obtained by using the spatial and temporal filters on the combined PW+tidal signal. However, the filtering scheme used for the thesis is for simplicity the same as has been developed in the pre-thesis report.

Thus, applying a series of spatial and temporal filtering schemes should isolate the PW, GWs (both orographic and non-orographic), and tides. This enables a study of their individual characteristics.

3.4 Spectral Analysis Methods

When analysing GWs, studying their spatial and temporal spectral distributions is useful. This can be done by finding the power spectral density of a spatial and temporal signal respectively, typically by doing a Fast-Fourier Transform (FFT) or, for time-series, a Generalised Lomb-Scargle (GLS) approach. In Section 3.4.1, a presentation of how the FFT will be used to yield the spatial spectrum, will be given. Furthermore, a description of how a total zonal GW power can be developed from the spectrum is also presented. On the other hand, in Section 3.4.2 the GLS is presented in relation to the temporal/frequency power density spectrum.

3.4.1 Spatial GW Power Density Spectrum

Roughly speaking, the spatial power density spectrum shows how much spectral power (equal to the square of the amplitude divided by the spatial frequency), is contained in all the waves associated with a specific spatial frequency, or equally wavenumber [7]. Hence,

a large peak at one specific wavenumber, indicates that this wavenumber is more dominant in the signal and thus contains more spectral power.

The chosen spectrum in the following is that of a zonal signal of GWs, after wave filtering, at a specific altitude and latitude. The signal is then a temperature function of longitudes, specified at a latitude, altitude, and time. This signal contains a wide range of spatial scales zonally, from the smallest possible waves that the resolution allows for, to waves up to the cutoff wavelength for the GW filtering, at WN25, or roughly 1000 km zonal wavelength. Then, the zonal spatial power density spectrum can be calculated by applying the FFT to the zonal GW temperature variation signal. The output is then the power density as a function of the ordinal wavenumber $k = 1/\lambda$ in the zonal direction with λ as the wavelength in metres. The unit of the power density is then $\mathrm{K}^2\mathrm{m}$, since the division by spatial frequency (i.e. wavenumber k), corresponds to a multiplication of the wavelength.

The implementation of the FFT is done by using the NumPy library in Python. Since the GW temperature variation is real-valued, the function rfft in the fft package of NumPy is used [43]. This calculates the one-dimensional discrete FFT of the signal along the longitude-axis. However, zero-padding is applied to increase the resolution of the power density spectrum. In this case, padding for a total resulting FFT vector of 4096 elements is done and found sufficient to resolve the spectrum well enough. Since the ends of the longitudinal GW temperature profile are connected, there is no need for a window function to taper the ends in this case. Hence, the rfft function should now simply output the zonal spatial GW power density spectrum, with 4096 bins for wavenumbers. The result will be presented and discussed in Section 4.2.

Having a zonal spatial GW power density spectrum, call it S_{xx}, the next step is to calculate a single-valued quantity for the specific spectrum at this latitude, altitude, and time. First, one should note that a consequence of Parseval's theorem for Fourier transforms is that the integral of S_{xx} over a defined wavenumber range gives the variance, or averaged power, of the GW signal. Integration over wavenumbers yields the unit of K^2. However, the variance also appears in the general potential energy equation for GWs

$$E_p = \frac{1}{2}\left(\frac{g}{N}\right)\overline{\left(\frac{T_{GW}}{T_0}\right)}^2, \tag{3.1}$$

in the last factor [12]. Here, T_{GW} is the GW temperature variation, T_0 is the total (raw) temperature, and the bar indicates a zonally integrated variance. Hence, the potential energy is proportional to the variance. For the rest of the thesis, the exact value of the potential energy is not in focus, hence Eq. 3.1 will not be calculated exactly. Instead, a zonally-integrated GW power, corresponding to the variance of the GW temperature, will be calculated and studied. From now on, this quantity is called the GW power. It is proportional to the potential energy of the waves within the integration interval and may therefore be used as a scaled measure of zonal GW potential energy.

Having the power density spectrum of GWs, the next step in arriving at the total zonal GW power is to integrate S_{xx} with respect to wavenumbers. The range is chosen to be from roughly 66 km wavelengths to 500 km, based on the characteristics of the inertial range of the spatial GW power density spectrum, which will be further discussed in Section 4.2. This is generally the range where most resolved GWs will be contained. The

integration is done numerically by applying Simpson's method using NumPy, and subtracting the noise level as indicated by a flattening of the spectrum at high (unresolved, but not subgrid) wavenumbers. Hence, a single-valued zonal GW power quantity is calculated for this specific altitude, latitude, and time. When this is done for all times, the result is a time series of GW power at this altitude and latitude. The power may vary in time as the power density spectrum for the GWs may be larger at times of large wave activity or smaller for little activity, which then affects the integral. This then becomes a quantity related to the total GW potential energy, or wave activity, longitudinally at an altitude, latitude, and time.

3.4.2 Frequency Spectrum With Significance Levels Using the Generalized Lomb-Scargle Periodogram

When studying the GW power and PW amplitudes variations, and their correlations in time, knowing the dominant periods involved in the time series may help diagnose what wave components may be related. The simplest way of studying the periods is by applying the FFT on the time series to get the frequency power spectrum. However, another popular efficient and powerful method, while more easily combined with determining the probability of noisy peaks, is the Generalised Lomb-Scargle (GLS) periodogram [59]. In general, the idea is similar to Fourier analysis. In GLS, sine waves of the type

$$y(t) = a\cos(\omega t) + b\sin(\omega t) + c, \tag{3.2}$$

are fit to datapoints $y_i(t)$ of the time series by means of analytically solving the set of linear equations for curve fitting as introduced by Lomb in 1976 [33]. The idea is to analytically determine the coefficients a, b, and c so that the squared error $(y(t) - y_i(t))^2$ is minimal for a given frequency ω. The amplitude of a peak is determined by the ratio of that period's weight in the signal. A dominant period gives a taller peak, which then results in a reduction of all other peaks. Hence, if there are multiple peaks, but one dominates, the less dominant may look insignificant, though that is not necessarily the case.

The method was further developed by Scargle in 1982, who investigated how the method is related to the statistical significance of peaks [48], [59]. Apart from being an efficient method, and working with time series of uneven sampling (not the case in WACCM-X), the close connection to statistically determining noise in signals is a significant reason why the Lomb-Scargle method is so popular.

In particular, the GLS is suitable for determining the False Alarm Probability (FAP) for any peak in the frequency spectrum. The FAP measures the probability that a random signal of no periodic component would result in the peak of that specific height [57]. Hence, it is a measure of the likeliness of any peak in the LS periodogram to simply be noise-generated, rather than a true sinusoidal period in the signal. It must be stressed that the FAP does not indicate the probability that the signal is indeed periodic. The definition of the FAP value is

$$\text{FAP} = 1 - [1 - P(z > z_0)]^M, \tag{3.3}$$

where $P(z > z_0)$ determines the probability of the GLS amplitude z to exceed a given value z_0, and M is the number of independent frequencies in the periodogram. Typical FAP values used to determine that the given peak is not a result of pure noise are 5% or

1%. In this thesis, the latter will be used as a limit. Hence, every GLS peak surpassing the 1% limit (i.e. with lower FAP values) is determined to most likely not be generated by noise alone.

The GLS periodogram for the time series of GW power, PW RMS temperature, and zonal mean zonal wind are presented and analysed in Section 3.4. The PyAstronomy package in Python is used to obtain these periodograms [47]. The main reason for using this package rather than the ”lombscarge” function in SciPy's signal package, is the excellent setup, inclusion, and functionality of the FAP significance analysis that PyAstronomy offers. Its GLS function can be called by the command ”pyPeriod.Gls”, see the documentation in [47] if needed. However, since this is an analysis of a time series, where sine waves are fitted to the series, the ends must be tapered first before applying the Lomb-Scargle. First, the time average must be subtracted, to yield the variations around zero mean. Then a window function must be applied to the time series, to taper the function to zero at the ends. In this case, a Tukey (tapered cosine) window of alpha value 0.5 is applied using SciPy. This was chosen as it typically has a fast-damping amplitude at the ends, and a full amplitude for an extended range of the series, given enough data points (here 124 data points). The Tukey window prevents a too wide dampening of the signal, in contrast to other windows. Now, the tapered and zero-mean time series is sent into the GLS function. The FAP levels and peak height in the GLS depend on the normalisation scheme used. Here, the ZK, or Zechmeister & Kuerster scheme is used [59]. Then, the FAP levels can be calculated from the generated GLS, and if needed, only the amplitudes above a manually chosen significance may be plotted. Those peaks become the significant peaks of the signal. However, a thing worth noting is that if a strongly dominant peak occurs, other peaks may be reduced in the GLS periodogram, and fail to reach a safe FAP level. This may result in false attribution to noise for relevant signal periods. Nonetheless, the GLS and FAP-level analysis is popular as it is generally useful in many cases in analysing time-series periodicity.

Chapter 4

Results & Discussion

In the following, the main results will be presented and their relation to the thesis statement outlined in Section 1.4 is discussed. To recapitulate, the objective is to progress our knowledge of the interactions of PWs with GWs in the winter NH middle atmosphere using the high-resolution WACCM-X. This model can partly resolve GWs down to relatively small scales, parameterises subgrid orographic GWs, and includes a scheme for generating non-orographic GWs.

To understand the possible interactions going on, one first has to observe and get an idea of how the individual wave types, mean wind flow, and polar vortex evolve in the month-long simulation. Only then can one diagnose what features characterise this particular simulation. This includes determining what state the polar vortex is in, what phases the PWs are in, and when and where GWs occur. Then, the spatial spectral power characteristics of the GWs will be analysed to determine the integrated GW power and its time evolution in the model simulation. This is then used as a rough measure of total zonal GW potential energy, strongly related to GW activity. Taking the analysis of this quantity further, the temporal spectrum will be presented. This is done using Lomb-Scargle periodograms to understand the periodicity within the calculated integrated GW powers. A similar analysis will then be conducted for the PW RMS temperature and the zonal mean zonal wind to compare the signal periods. Lastly, linking the PWs, zonal mean zonal wind, and GW interactions together, correlation analyses are conducted, and a thorough discussion of the possible interactions is presented.

4.1 Atmospheric Conditions in the Model Simulation

To better understand the results, it is crucial to diagnose the atmosphere in terms of GWs, PWs, and the polar vortex. Additionally, examining various vertical and horizontal slices of the atmosphere at a time can provide insight into which waves are present in the month-long WACCM-X simulation and their respective location. Hence a more intuitive and fuller picture of the atmosphere at hand can then be made, which sets the groundwork for what is to come in the analysis of PW interactions with GWs.

4.1.1 Zonal Mean Zonal Wind

Since the GW activity depends on the mean wind flow conditions, it is worth investigating the zonal mean zonal wind in the month-long WACCM-X simulation.

The zonal mean zonal wind is calculated at each time step by zonally (longitudinally) averaging the zonal wind (U) at every altitude and latitude. Essentially, this corresponds to the zonal background wind flow in the atmosphere.

The latitude-altitude distribution of the zonal mean zonal wind is presented in Fig. 4.1. Fig. (a) shows the case of 17th Jan at UTC 18:00, while (b) represents the situation ten days later, on 27th Jan at UTC 18:00. The plots cover both hemispheres and reach up to 120 km.

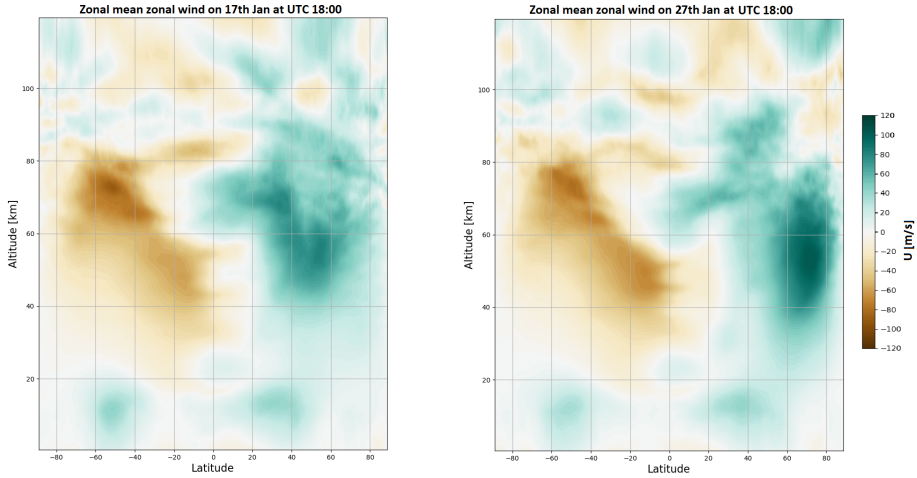

Figure 4.1: Vertical-meridional snapshots of zonal mean zonal wind at two different times. In (a), the zonal mean U is shown on 17th Jan at UTC 18:00, showcasing a stratospheric polar vortex mostly localised between 40°-60°N, as seen by the eastward wind maximum in this region. In contrast, (b) shows the zonal mean zonal wind ten days later, on 27th January at UTC 18:00, where the same polar vortex has moved north and strengthened, centred around 60°-80°N.

The first thing to notice is the apparent strong eastward zonal mean zonal wind in the NH middle atmosphere and the westward wind in the Southern Hemisphere. Those are characteristics of the polar vortices, strong zonal winds that typically range from 15 km to above 50 km in altitude and act to trap the polar middle atmosphere air from the airflow at lower latitudes. These stratospheric vortices are distinct from, and should not be confused with, the tropospheric polar jets, which can be seen as dots of eastward winds at about 10-15 km altitude in the mid-latitudes. For the middle atmosphere vortex, maximum polar vortex winds are found around 50-70 km high. This is all expected in January, and the vortex structures in the two hemispheres agree with climatology [56]. Interestingly, the zonal mean zonal wind in the simulation is significantly stronger than the reference climatology. As an example, when monthly averaging the zonal mean zonal winds in the winter stratosphere at 60°N for the winters of 1979-2020, the maximal wind was around 40

m/s, with a standard deviation of about 13 m/s [10]. Doing a similar mean gives a monthly mean wind maximum at 70 m/s in the stratosphere at this latitude in this simulation, hence outside 2 standard deviations (95%) from the mean.

Moreover, a key observation when comparing the two plots in Fig. 4.1 is the latitudinal motion of the middle atmosphere polar vortex in the NH. There is great variability within the time interval of the dataset. On 17th Jan, it is mainly centred above 30°-60°N, and reaches a maximum of about 80 m/s. Hence, the vortex is in a weak and spread-out state. Ten days later, the vortex has moved north to 60-80°N and is slim and tall. Furthermore, its maximum is around 120 m/s, so the zonal wind is significantly stronger. Hence, at this time, the vortex appears to be in a strong and concentrated state. This polar vortex motion and variability will be relevant for the remainder of the discussion.

A different perspective of the zonal mean zonal wind is shown by the time-evolution plots, also called Hovmöller plots, as shown in Fig. 4.2. In (a), the vertical-time plot of the zonal mean zonal wind at 45°N is shown, while (b) shows the case of 65°N. In the former case, the zonal mean zonal wind has its maximum at the beginning of the dataset, the first 7-8 days (13th-20th Jan), before weakening significantly with a reduction of about -50 m/s from day 8 to 11 (20th-23rd Jan). A slight increase of the wind then occurs before another weakening in the last few days. At this latitude, the plot may give an impression that there could be a 20-day periodicity to the zonal mean zonal wind at 45°N. However, the dataset is relatively short in order to determine this safely. Interestingly though, studies indicate that the polar vortex edge, and hence the zonal mean zonal wind, often follows a 20-day oscillation of displacement from the North Pole in the stratosphere during winters, known as the Polar Night Jet Oscillation (PJO) [23]. This occurs in particular in the European sector. It has been found that such a vortex position is correlated to the displacement and increase in strength of the Aleutian anticyclone, a strong high-pressure system above the Aleutian Islands (Alaska, US) and the Bering Sea [23], [20]. Furthermore, PW activity and propagation from below may displace the vortex, as will be discussed more in Sections 4.3 and 4.5. Hence, it is not unreasonable that this could be a factor behind the apparent periodicity of zonal mean U at 45°N. This will be studied further in Section 4.4.

In 4.2(b), at 65°N, the zonal mean zonal wind is found to be significantly stronger in the middle atmosphere. In contrast to the mid-latitude case, the weakest winds are found at the beginning of the dataset, while the vortex strengthens significantly on days 8-10 and onward. Comparing with the two side views of Fig. 4.1, 17th Jan corresponds to day 5, while 27th Jan is day 15. The maximal zonal mean zonal wind at 65°N occurs on day 19 (31st Jan) and exceeds 120 m/s. Interestingly, a weakening of the vortex at 65°N occurs in the last 7 days (6th-12th Feb).

A latitude-time Hovmöller plot at 50 km altitude is presented in Fig. 4.2(c). This clearly shows the polar vortex migration from mid to high latitudes around days 5-10 (17th-22nd Jan), and a strong vortex during days 10-23 (22nd Jan-4th Feb). The maximal zonal mean zonal wind at 50 km happens between latitudes 60°-70°N. This also illustrates that the time the vortex is located at high latitudes is long compared to the dataset. Furthermore, at mid-latitudes, the apparent periodicity is again noticeable. The location at which this occurs suggests that the polar vortex edge could have some oscillatory effects in that it typically migrates down to the mid-latitudes and back up to the high latitudes. Hence, this will be investigated in the next section.

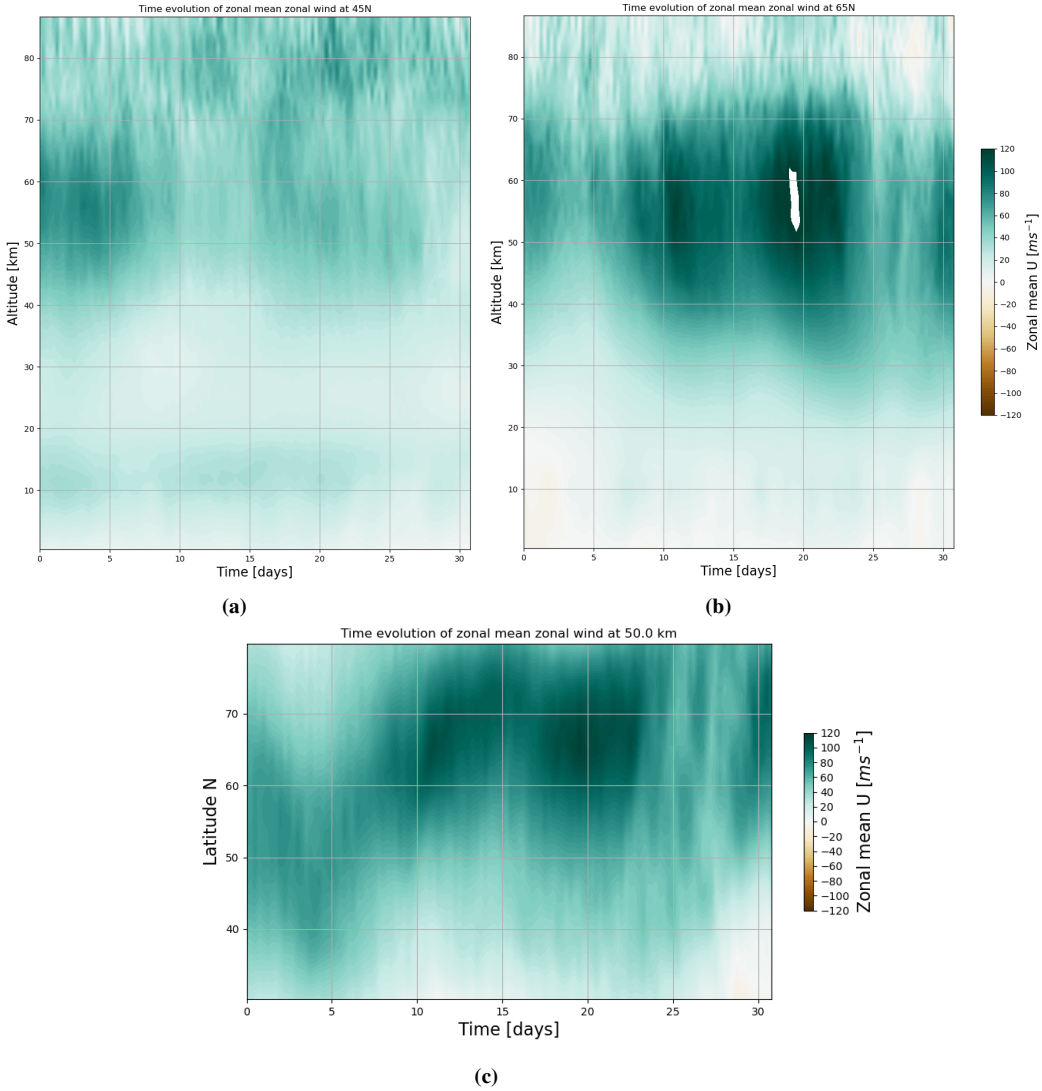

Figure 4.2: The variation of zonal mean zonal wind at (a) 45°N and (b) 65°N in time and altitude. A latitude-time plot of the zonal-mean zonal wind at 50 km (where the maximum wind is found) is also presented in (c) to complement the vertical evolution. The time axis represents the day number from 13th Jan (day 1) to 12th Feb (day 31).

Why precisely the polar vortex happens to be as strong and far north as in the simulation is not possible to infer due to the complexity of the model. It could be due to internal variability in the model, as the external forcings are set manually. For example, a possible deficit of PWs may reduce the total drag on the mean winds.

4.1.2 Stratospheric Polar Vortex Horizontal Wind

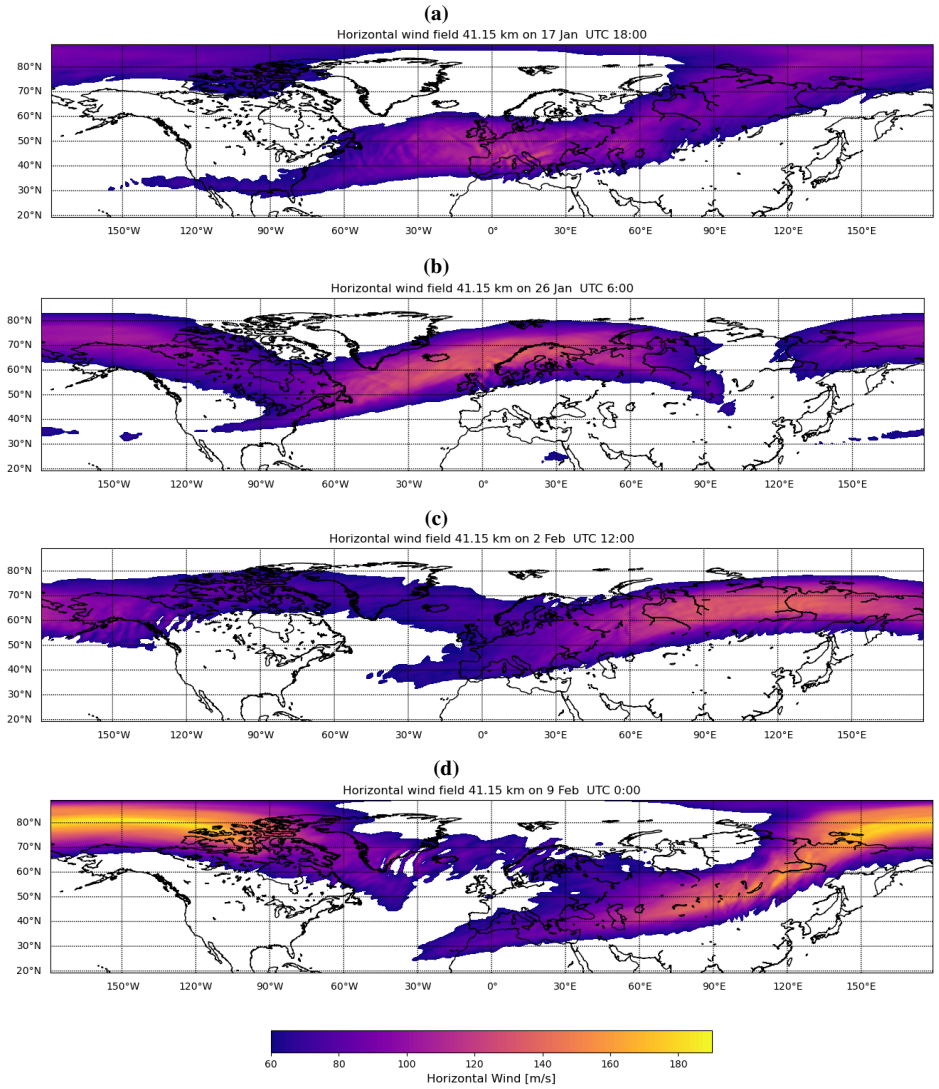

Figure 4.3: Horizontal snapshots of the raw horizontal winds between 60-190 m/s at 41 km. (a) 17th Jan UTC 18:00, (b) 26th Jan UTC 06:00, (c) 2nd Feb UTC 12:00, and (d) 9th Feb UTC 00:00.

To get a more complete picture of the polar vortex and its horizontal jet distribution at the stratospheric level, it is necessary to illustrate the raw wind at different times. While the zonal mean zonal wind represents the zonal background flow and manifests a zonal mean polar vortex, the vortex edge is typically a strong, meandering jet, and its structure is visible in the raw horizontal local wind. This wind is the combination of the zonal

mean background wind and the variability caused by waves, particularly PW wind. The meandering is visible as a strong stratospheric polar jet that makes up the polar vortex edge. The vortex could be stable or unstable. In the former case, the winds are strongly zonal. If the latter is the case, the vortex may wobble and meander at the edges, and the vortex centre displaced from the Pole [56], [27]. Since these meanderings typically cause zonal variations in the middle atmosphere wind, they become the primary source of wind perturbations from the zonal mean zonal wind background flow. Furthermore, since they are of planetary scales, they manifest as PWs.

The stratospheric horizontal wind, i.e. the vector magnitude of the combined zonal and meridional wind, is calculated and plotted at 41 km altitude for four different times in Fig. 4.3. The choice of snapshot times is based on the results of the zonal mean zonal wind plots of Fig. 4.2. The four times are (a) 17th Jan UTC 18:00, when the zonal mean wind maximum is far south and weak, (b) 26th Jan UTC 06:00 when the zonal mean wind is strong and maximum located far north, (c) 2nd Feb UTC 12:00 at the end of the strong zonal mean wind far north and (d) 9th Feb UTC 00:00 when the zonal mean wind has weakened again. The altitude of 41 km is chosen since that is within the altitude of the polar vortex with strong zonal winds. Furthermore, 41 km is in the upper stratosphere, where PWs and GWs tend to become large-amplitude waves and is thus a suitable altitude for comparisons of the waves later.

The raw wind plots illustrate strong meandering jets in the stratosphere that evolve over time. On 17th Jan, as shown in Fig. 4.3(a), the horizontal winds are relatively weak. However, a visible broad jet is seen over Central Europe, with local winds reaching 100-120 m/s. This occurs while the zonal mean zonal wind is relatively weak and centred at the mid-latitudes of 45-50°N. Moreover, the polar vortex centre appears to be between Greenland and Svalbard. Hence the whole vortex is displaced from the Pole towards the European sector at this stage.

Significant changes of the stratospheric wind jet occur between Fig. 4.3(a) and (b), around 21-24 Jan, which is not shown here. The jet above Europe and Siberia then wobbles violently and quickly in the meridional direction, causing a transverse wave in the jet moving eastward, indicating instabilities in the vortex. The entire jet above Europe collectively moves north as the polar vortex centre migrates polewards until the case of Fig. 4.3(b) is reached on 26th Jan. This wobbling coincides with the strengthening and high-latitude shift of the zonal mean zonal wind as seen and discussed in Fig. 4.2. In contrast to the violent wobbling of the jet on 21-24 Jan, the curvature of the wind jet on 26th Jan stays relatively fixed in its shape for several days. However, the whole jet structure is seen moving eastwards as a collective unit of fixed shape between 26th Jan and 2nd Feb (Fig. 4.3(c)). This likely occurs due to particularly strong eastward wind and stable vortex at this time interval.

Interestingly, the strongest horizontal winds reach up to 190 m/s and occur at the late stage of the dataset, as seen on 9th Feb in Fig. 4.3(d). This corresponds to when the zonal mean zonal wind weakens significantly as seen in Fig. 4.2. It also shows a drastically different structure from a week earlier in 4.3(c). The jet structure is strongly meandering with an extensive meridional range. The weakening of the zonal mean, but strengthening of the jet, is mainly due to the strong meandering of the polar vortex edge that causes strong zonal variations. Furthermore, the vortex centre appears to be around Svalbard.

Hence the vortex is again driven off the Pole towards the Eurasian sector. It should also be mentioned that rapid wobbles in the jet precedes this snapshot, indicating a strongly unstable polar vortex. Hence, the vortex appears to shift between stability and instability throughout the dataset.

4.1.3 Planetary Waves

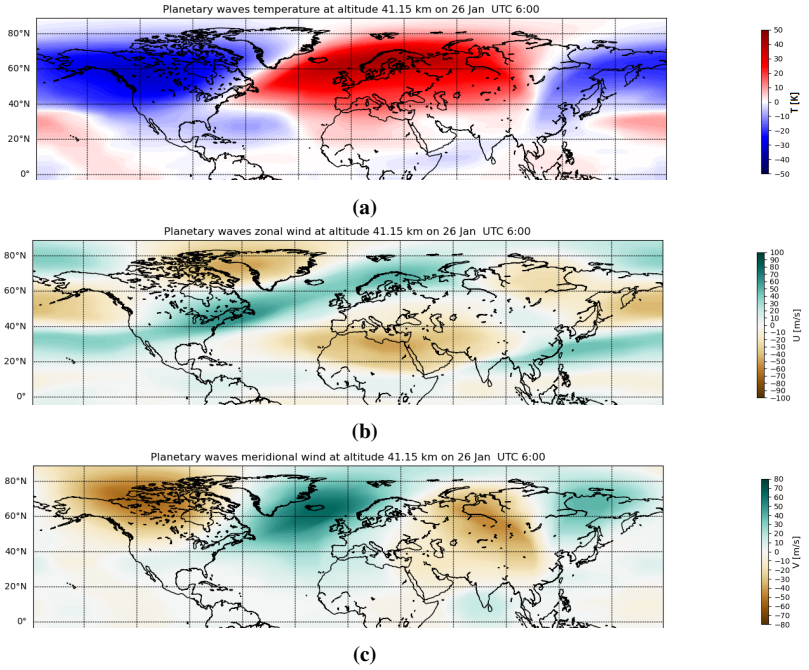

Figure 4.4: Horizontal snapshots of PW temperature in (a), PW zonal wind in (b), and PW meridional wind in (c), on 26th Jan UTC 06:00 at 41 km altitude.

It is also crucial to get a good impression of the PW distribution and dynamics to understand possible PW-GW interactions. Therefore a general description and discussion of the PWs will be presented here, focusing mainly on the stratospheric and mesospheric PWs.

The horizontal distribution of PWs on 26th Jan UTC 06:00 is shown in Fig. 4.4. Subfigures (a)-(c) show PW temperature, PW zonal wind, and PW meridional wind respectively, all for 41 km altitude, i.e. stratospheric PWs. As is discussed later, the PWs vary significantly during the 31-day dataset in dominant wavenumbers, amplitudes, and apparent motion relative to the ground. The time at hand in Fig. 4.4 corresponds to when the polar vortex in the stratosphere is strong, located between 60°-80°N, and when PWs show large amplitudes.

The horizontal snapshots clearly show that most PWs are located at mid and high latitudes during the winter. The two temperature plots show large WN1 PWs. The maximal amplitude of the temperature PWs is around 50 K.

The PW zonal wind in Fig. 4.4(b) are seen as diagonal lines, particularly over the North Atlantic, with apparent WN1 to WN2 structures. Notice that the PW wind is eastward at 41 km over the Atlantic and resembles the jet shown in the raw wind plots of Fig. 4.3(b), indicating that PWs manifest themselves in the meandering jets. Furthermore, this eastward PW wind swings and blows strong eastward winds of around 50-70 m/s in the stratosphere above Scandinavia.

The meridional wind PWs in Fig. 4.4(c) show a clear WN2 wave in the NH winter, with amplitudes of around 80 m/s at most. The amplitudes seem reasonable, as a combined WN1 and WN2 PW in the NH winter has been found to typically reach 60 m/s by meteor radar measurements [53].

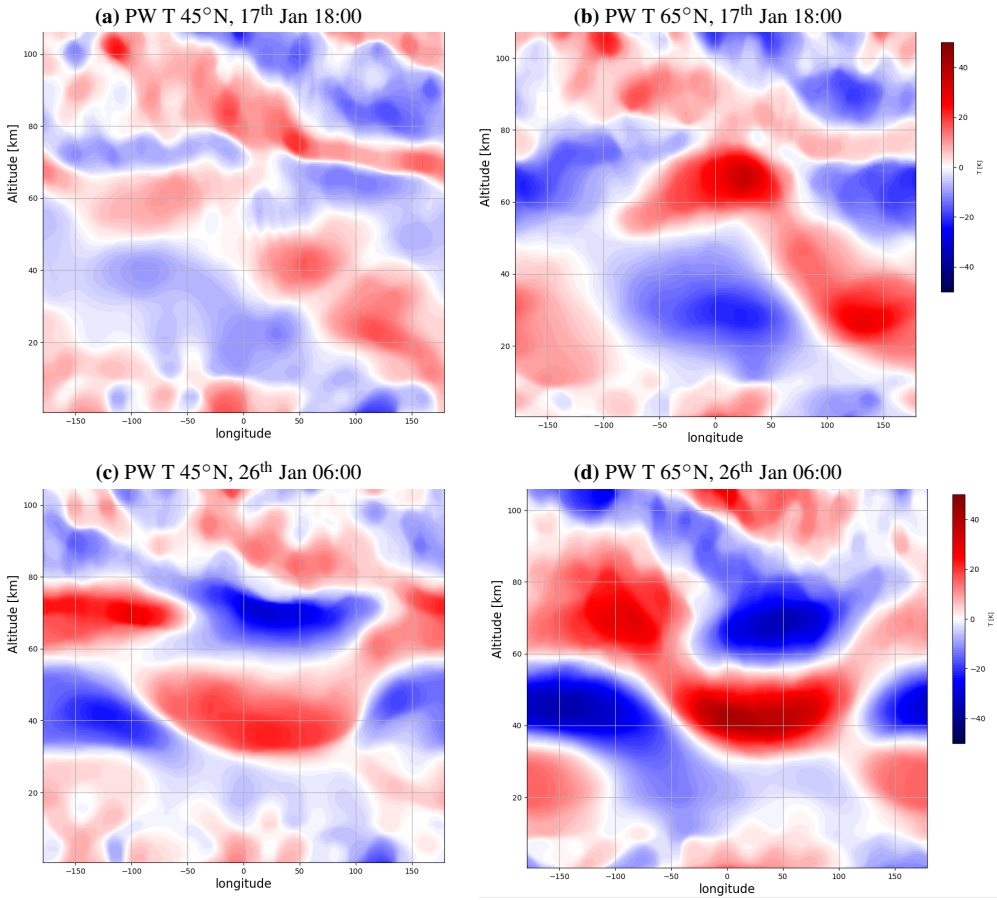

Figure 4.5: Zonal-vertical snapshots of PW temperature along 45°N (left) and 65°N (right) on (a)-(b) 17th Jan at UTC 18:00, and (c)-(d) 26th Jan at UTC 06:00.

The zonal-vertical distributions of PWs on 17th Jan 18:00 and 26th Jan 06:00 are shown in Fig. 4.5, with cross-sections at 45°N to the left and 65°N to the right. The

vertical plots show the vertical distribution of PW up to 100 km. As seen in subfigures 4.5(a) and 4.5(b), on 17th Jan 18:00, the PWs seem relatively weak and tilted at this time. This corresponds to the time of the weak and southward-displaced polar vortex. The tilt is suggestive of upward PW propagation [26]. On 26th Jan 06:00, as seen in Fig. 4.5(c)-(d), the tilt is gone, and the temperature PWs manifest themselves as vertically-stacked WN1 waves in the stratosphere and mesosphere, with opposite phases in the two layers. This is consistent with models and observations that some WN1 PWs of opposite phases often exist in the mesosphere in the wintertime [52], [26]. The structure is similar at mid-latitudes (45°N) as at high-latitudes (65°N), although the amplitudes in the latter case seem to be most prominent for both times.

In reality, the PWs change with time. Figs. 4.4 and 4.5 only show the PWs at one and two time steps respectively. Certain aspects of this change, particularly in the middle atmosphere, can be observed from the Hovmöller diagrams in Fig. 4.6. The zonal PW temperature evolution along 65°N, 41 km, is shown in Fig. (a). The evolution along other latitudes, like 45°N, looks similar, although with WN2 waves in the first five days, before evolving into a dominant WN1 motion similar to the figure at hand. Furthermore, the situation in the mesosphere (not shown) is similar, although opposite phases of what occurs in the stratosphere.

From the Hovmöller PW T diagram at 41 km, 65°N, in Fig. 4.6(a), it is evident that on day 14 (26th Jan), i.e. the day of Figs. 4.4 and 4.5, the PW temperature amplitudes are close to the maximum, at about 50-60 K. The weakest amplitudes are found during the first five days. In light of the zonal mean zonal wind discussion, this happens to be when the mean wind flow in the stratosphere is weak and centred above mid-latitudes. The PWs appear then to be quasi-stationary waves relative to the ground. This is followed by 5-7 days of westward propagation with an amplification of the waves. As the mean flow is eastwards in the NH stratosphere for all times in the dataset, most PWs should propagate westwards relative to the wind, although some weak eastward-propagating PWs are typically present. Around day 10-15 (22nd-27th Jan), the PWs reach their maximum amplitude and start propagating eastwards relative to the ground. This propagation continues until day 25 (6th Feb). During this time, the zonal mean zonal wind is strong, at about 80 m/s at 65°N, and its maximum is centred in the high latitudes. Lastly, one can observe that the PWs become quasi-stationary again in the last 5-6 days, with a slight westward propagation in the very last days. However, the amplitudes remain large. Knowing from Section 4.1.1 that the mean flow has weakened the last days, the change of propagation is likely caused by this zonal mean flow weakening.

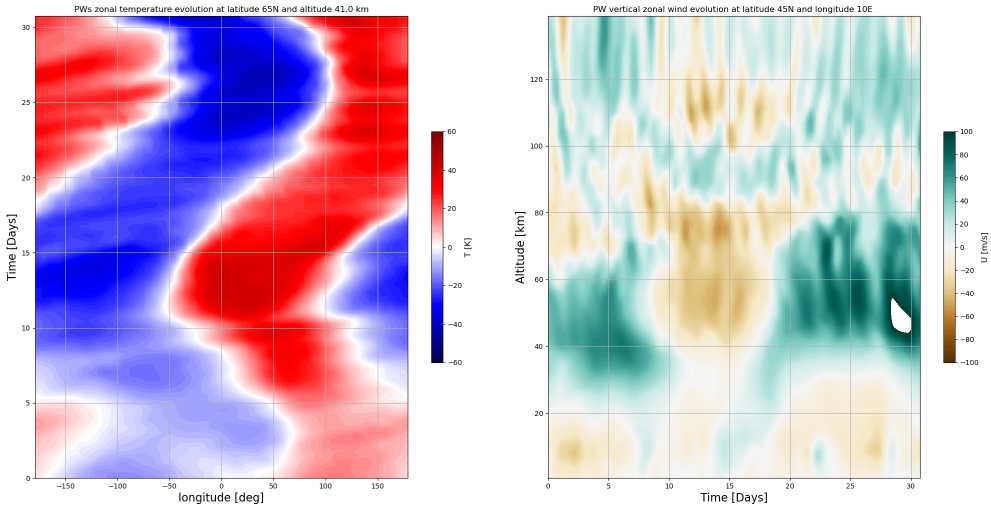

(a) PW T 41 km, 65°N

(b) PW U 45°N, 10°E

Figure 4.6: A selection of PW Hovmöller diagrams. Longitudinal evolution of PW temperature at 41 km, 65°N is shown in (a), indicating westward propagation relative to the ground in the beginning and eastward propagation during the days of strong zonal mean wind. Fig. (b) shows the vertical evolution of PW zonal wind at 45°N, 10°E (Northern Italy), indicating a change of PW U from eastward to westward in the stratosphere above this location around the time when the zonal mean wind is strong at high latitudes.

A vertical Hovmöller diagram of PW U at 45°N, 10°E (above Northern Italy, close to the Alps) is shown in Fig. 4.6(b). The location is chosen because it reflects the eastward PW wind variability over Central and Southern Europe. This is a region where the polar vortex edge appears to pass over several times, as indicated by the horizontal raw winds in Fig. 4.3. Such a Hovmöller diagram of PW U above Italy may diagnose when the stratospheric zonal wind perturbation is eastwards, which has been indicated before to be favourable for orographic GW generation and filtering [52]. One can observe from the diagram that the eastward PW zonal wind is present the first 5-7 days of the dataset, which is when, as will be seen in Section 4.1.4, the tropospheric-generated GWs are most active in this region. It also corresponds to when the middle atmosphere zonal mean zonal wind is generally weak but centred above 40-50°N. When the polar vortex starts migrating polewards and increasing its eastward wind speed, from around day 10-20, the PW zonal wind has been replaced by a westward PW wind over Central Europe. Lastly, an eastward PW wind is again present over Central Europe for the last ten days. Investigating this in depth by analysing the horizontal map of PW U for each time step reveals that this is due to the whole PW eastward wind jet, as seen in Fig. 4.4(b), propagating eastwards while in the strong eastward mean flow. Thus, the mid-latitude part of the PW U jet over America on day 14 propagates eastward toward Central Europe in the last few days.

4.1.4 Gravity Waves

Since the main focus of the thesis is the interaction of PWs on GWs, it is necessary to present when and where GWs occur. The area of focus is the NH since most GWs are located there in January-February. There are also some large GWs in the WACCM-X simulation near the Equator and a multitude of GWs in the MLT in both hemispheres. These are likely generated by convection from storms and other weather systems of large vertical scales in the troposphere. They are not of interest to this discussion.

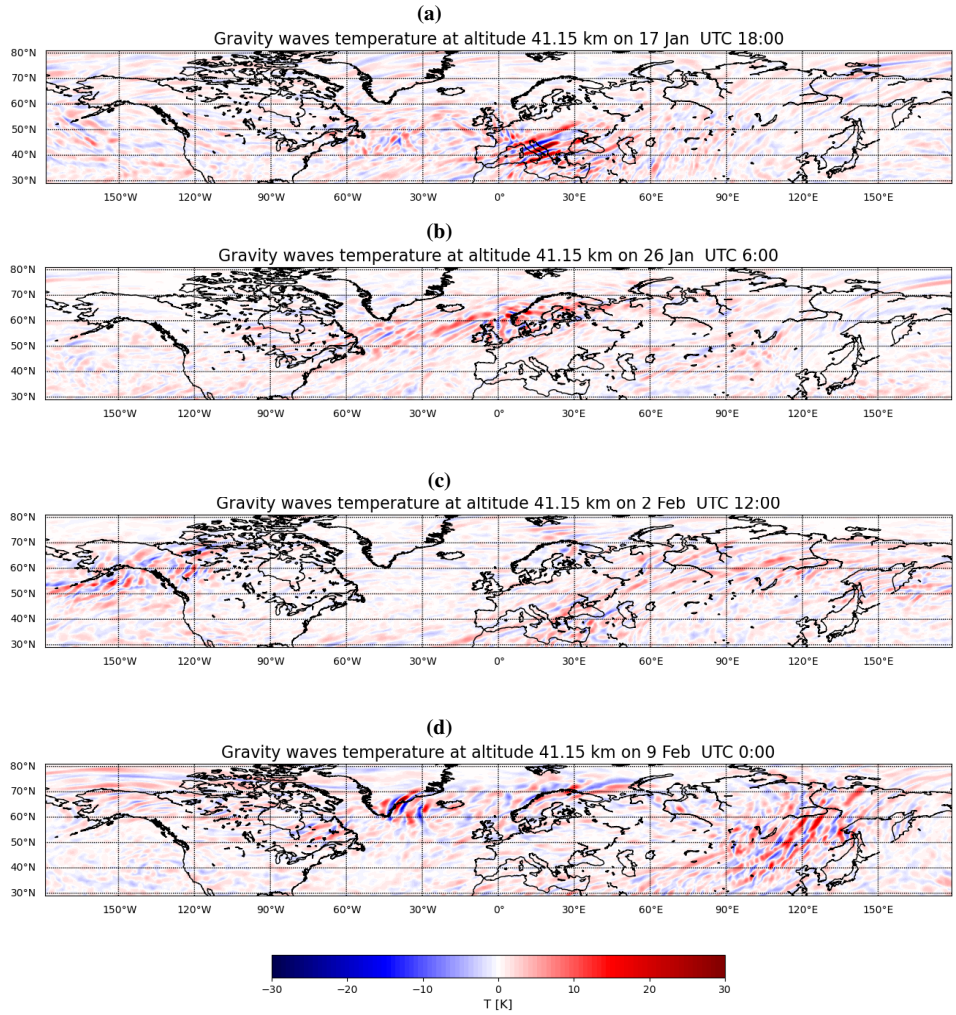

Figure 4.7: Horizontal snapshots of GW temperature in the stratosphere, at 41 km. This shows the horizontal GW distribution at four different times: (a) 17th Jan UTC 18:00, (b) 26th Jan UTC 06:00, (c) 2nd Feb UTC 12:00, and (d) 9th Feb UTC 00:00. GWs are generally located at different latitudes and locations for the four different times.

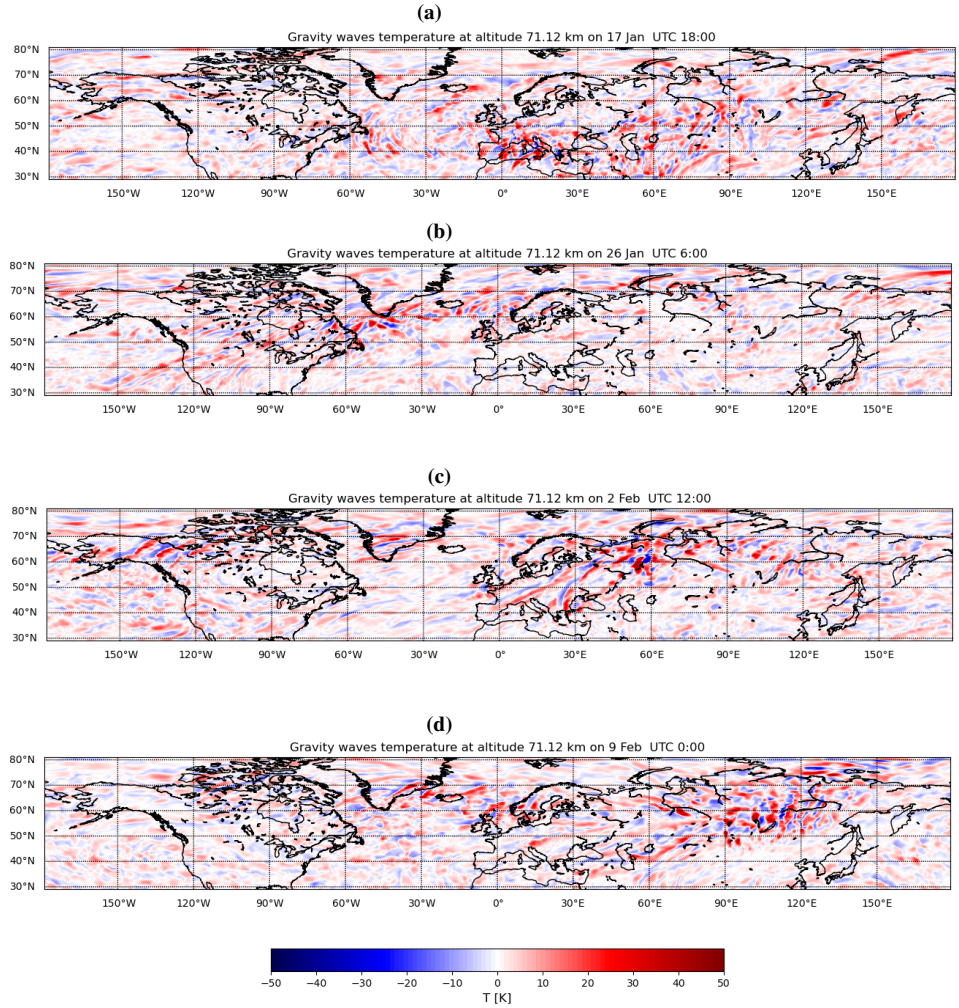

Figure 4.8: Horizontal snapshots of GW temperature in the mesosphere, at 71 km. This shows the horizontal GW distribution at four different times: (a) 17th Jan UTC 18:00, (b) 26th Jan UTC 06:00, (c) 2nd Feb UTC 12:00, and (d) 9th Feb UTC 00:00. GWs are generally located at different latitudes and locations for the four different times.

The horizontal distribution of GWs in the NH stratosphere at 41 km altitude at four different times is shown in Fig. 4.7, with corresponding GW plots for the mesosphere at 71 km shown in Fig. 4.8. The chosen snapshots correspond to the times of the 41 km raw wind plots of Fig. 4.3 at four different stages of the polar vortex. Some key observations can be drawn from these plots.

Firstly, the plots for 17th Jan UTC 18:00, in Figs 4.7(a) and 4.8(a), show that most of the GW activity at that time is located around mid-latitudes in both the stratosphere and mesosphere. In the latter, the situation is somewhat chaotic, as a multitude of GWs

are present. Furthermore, the altitude is close to the typical breaking altitude of GWs, which often occurs between 70-80 km altitudes. Because of the exponential growth of GW amplitudes with height, the wave amplitudes are large, up to 50 K. On 17th Jan, most waves are visible over Southern Europe, Central Asia, and east of North America, restricted to the mid-latitudes.

In the stratospheric case of Fig. 4.7(a), still on 17th Jan, large waves of horizontal wavelengths close to 600 km and wide wavefronts stretching thousands of kilometres can be seen in the stratosphere over Italy and the Balkan. These reach up to 30 K in amplitudes at 41 km altitude. The waves look similar to those observed over the same region during January 2016, which have been heavily analysed by multiple sources, using AIRS measurements [9], and reanalysis data from ERA5 [14]. Comparing Fig. 4.7(a) above with Fig. 13(c) in Dörnbrack's paper from 2021 [14], the GW temperature perturbations compare well at roughly the same altitude on 12 Jan 2016 as found from the ERA5 dataset. His study suggests large orographic GWs being generated, particularly from mountainous sources along the European section of the 45°N latitude during the specific conditions of January 2016. Interestingly, the conditions of the polar vortex horizontal wind (recall Fig. 4.3) are also similar on 17th Jan in the WACCM-X simulation at hand, as compared with the 12th Jan 2016 ERA5 reanalysis data. Looking at Fig. 4(c) in Dörnbrack's paper, which shows the horizontal stratospheric winds being strong between 50-60°N, and similarly Fig. 12 in Bossert's paper [9] showing the same Jan 2016 wind at 42 km, these conditions are similar to the case in the WACCM-X 17th Jan simulation. In all these cases, the zonal mean zonal wind maximum is centred at the mid-latitudes, as in Fig. 4.1. Hence, the similarities with 2016 and the nature of the wavefronts over Europe suggest that orography-generated GWs dominate Europe at this time.

On 26th Jan, the majority of the GWs are observed to be situated further north, as seen in Figs. 4.7(b) and 4.8(b). The difference from 17th Jan is apparent in both altitudes. Now waves over Central and Southern Europe are almost nonexistent, while large bands of waves are visible over the North Atlantic southeast of Greenland. This band is similar to the eastward PW zonal wind as seen in Fig. 4.4(b), and the polar vortex edge in Fig. 4.3(b), which at this time has wobbled and moved north. Furthermore, this time step corresponds to strong zonal mean zonal wind at high latitudes and large PW amplitudes. The lack of orography near the GW band over the North Atlantic may indicate non-orographic wave sources. The wavefront orientation, parallel to the wind jet direction, is typically an indication of in situ wave generation by the jet [9]. On the other hand, larger amplitude, shorter wavelengths, and wavefronts aligned with orography above Scandinavia may suggest orography-generated GWs occur at that specific location.

Next, on 2nd Feb, as seen in Figs. 4.7(c) and 4.8(c), the wave activity all over the North Atlantic is reduced. Little wave activity is seen over Europe in the middle stratosphere, while large waves are seen in the mesosphere across Europe and Siberia. Most notably, the GW activity in the stratosphere is the largest over Alaska. Recall that at this time, the vortex and zonal mean wind are still excessively strong at high latitudes, just before the final instability and weakening occur. Also, the eastward PW wind band that was above Europe a week earlier has now propagated eastward. Hence, the PW winds are no longer favouring waves over Europe and the North Atlantic. This eastward PW band is now located over Alaska, coincidental with GWs. This strengthens the possibility that the

eastward PW wind band allows GWs to filter or be generated. It is also found, by zonal-vertical analysis (not shown), that the southernmost wavefronts close to Alaska (at 55°N) are vertically connected down to the troposphere. In contrast, the northernmost wavefronts (at 65°N) of similar wavelengths are only visible from the mid-stratosphere and up to the mid-mesosphere. This may indicate partly orographic and partly non-orographic generation of GWs around Alaska.

Lastly, on 9th Feb UTC 00:00, Figs. 4.7(d) and 4.8(d) show the stratospheric and mesospheric GW distribution in the late stage of the dataset. Recall that the polar vortex is now unstable, migrating southwards, wobbling at the edges and weakening its strength. Large GWs are seen east of Greenland at both altitudes. A closer look at the vertical distribution of these waves can be seen in Fig. 4.9(a). The wavefronts stretch all the way down to the tropopause, indicating tropospheric generation. This could indicate orographic sources. Based on the wave orientation, they are likely caused by the north-south mountain ranges on Southern Greenland, at around 60-65°N, 45°W. The middle atmosphere mean flow has weakened at this time, and only a weak eastward turning westward PW wind (but strong PW T) is present in the stratosphere in this region. Thus, that could indicate orographic waves are being filtered through in the moderate wind at that location. Moreover, significant wave activity is found over Eastern Siberia and aligns well with the location of the polar vortex edge at this time.

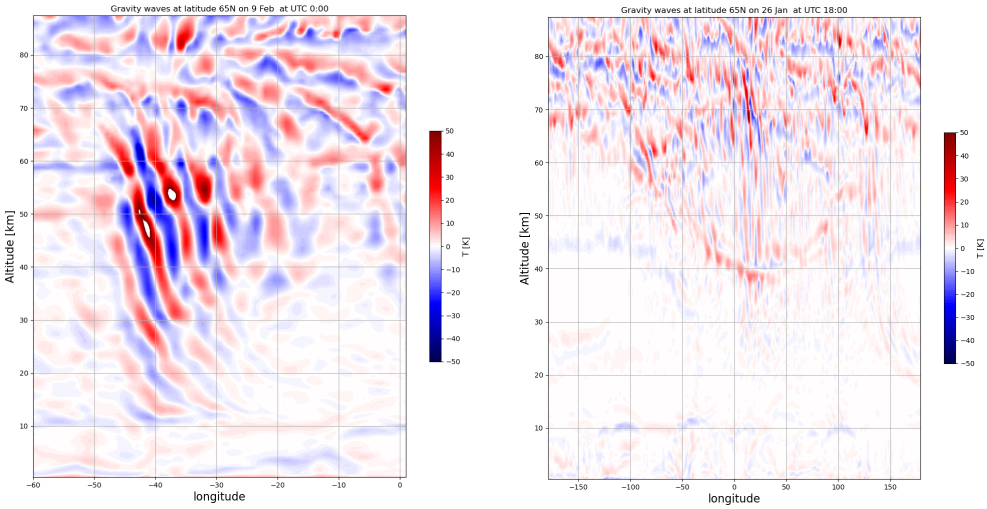

(a) **(b)**

Figure 4.9: A selection of GW profiles in the zonal-vertical cross-section. In (a), a close-up of the GWs east of Greenland at 65°N on 9th Feb at UTC 00:00 is shown, with vertically-tilted phase fronts of large amplitudes. In (b), a full zonal-vertical cross section up to 88 km along 65°N on 26th Jan at UTC 18:00 is shown. Note the lack of GWs in the lower stratosphere and troposphere in this case.

Looking again at the possibly orography-generated GWs east of Greenland in Fig. 4.9(a), the wavefronts are similar to those of Fig. 1.1, with a tilt relative to the vertical. This is due to each corrugated sheet of air affecting the layer directly above it so that

the waves at higher altitude lag in phase compared to the lower ones since the time the air perturbation has hit these layers is longer. The tilt gets steeper in the upper stratosphere, indicating stronger background winds to propagate against, which makes sense as the maximal zonal mean flow is found around 50 km high. This can be explained by the wind dependence of the phase and group velocities as described by Eqs. (2.50) and (2.51). Since the group velocity is parallel to wavefronts, any change in its components must correspond to changes in the tilt. The vertical wavelength increases for increasing background wind in the opposite direction to the wave propagation while the horizontal wavelengths remain unchanged. The opposite is the case for weaker wind.

A similar wavefront as that of Fig. 4.9(a) has been studied in depth in the pre-thesis project report [38]. The waves were then orographically generated from islands in the Southern Ocean and visible in the WACCM5 7-day July simulation of hourly time resolution. Background winds were estimated, and it was found that the steepest wavefronts corresponded to the largest background wind. The high time resolution enabled a frame-by-frame analysis of the wave propagation. This is not possible with the 6-hour resolution in WACCM-X since these waves typically have periods of a few hours and may vary significantly even within 6 hours. However, the waves seen east of Greenland appear to be roughly quasi-stationary for about a day or so, a strong indication of orographic MWs. Moreover, some simple calculations can be made from the observed wavelengths in this still image. The horizontal wavelength is close to 300 km, and the vertical wavelength varies from 7 km in the lower stratosphere to about 20 km in the upper stratosphere (30-50 km altitude). This gives a wave period of about 1.33 h in the stratosphere by calculating $\hat{\omega}$ as in eq. (2.49) and finding the period from this. This is reasonable, as similar wave periods and wavelengths were found for waves in the Southern Ocean in WACCM5 and are typical for MWs. Moreover, the overall characteristics of the MWs east of Greenland are consistent with the observed characteristics with orographic waves of this wavelength in the ERA5 reanalysis of the 2016 January wave activity as mentioned by Dörnbrack [14]. Although waves over Europe were the primary focus of his study, the waves are similar. Wavefronts were then found tilting westwards with a horizontal wavelength of 300 km and vertical wavelength of 18 ± 2 km (see Fig. 15(a) in Dörnbrack's 2021 paper), similar to the case here. Interestingly, Dörnbrack found these tilted wavefronts east of the Alps at around 45°N. Although not shown here, the vertical profile of the GWs on 17$^{\text{th}}$ Jan in our WACCM-X simulation, corresponding to the situation in Fig. 4.7(a), show similar characteristics southeast of the Alps, indicating large MW activity over Europe at that time.

An interesting observation can be inferred from Fig. 4.9(b), showing the zonal-vertical GW distribution along 65°N on 26 Jan UTC 18:00 (day 14). Even though Figs. 4.7(b) and 4.8(b) show significant wave activity in the stratosphere and mesosphere at high latitudes at this date, the zonal-vertical cross section gives insight into the sources of these waves. The lack of wavefronts in the lower stratosphere and troposphere, in contrast to Fig. 4.9(a), is apparent. Most waves only appear in the upper stratosphere and the MLT at this latitude and time. Furthermore, recall that the zonal mean wind is strong and located at high latitudes at this time. Moreover, the large diagonal red band seen around 40 km altitude, between 50°W to 50°E, is found to be a residual component of the polar vortex edge (in temperature), located in the strong wind jet as seen in Fig. 4.3(b). The jet is strong

and above several possible orographic sources. However, the zonal-vertical plot of Fig. 4.9(b) may suggest GW generation close to the red band associated with the jet at 40 km rather than from tropospheric sources. Further evidence stems from the already mentioned orientation of the horizontal wavefronts along the horizontal jet direction at 41 km (see Fig. 4.7(b)), which is a characteristic of stratospheric wave generation. Hence, these findings already indicate that orography-generated waves are not likely always the case in the NH winter, but another type of stratospheric generation occurs. The waves appear to be generated in the stratosphere and propagate up and down from there. This begs the question: What is causing this seemingly non-orographic GW generation? It is also interesting to study under what conditions the orographic GWs are filtered to propagate vertically through the stratosphere, particularly in relation to the PWs and winds.

4.2 Gravity Wave Spatial Power Density Spectrum and Zonal Wave Power

To better understand the variability of GWs during the polar winter, it is essential to analyse their spectral density across different spatial scales. This analysis can provide valuable insights into how well the GWs detected by WACCM-X align with actual data. By this analysis, it is also possible to calculate the integrated GW power, which is proportional to the total GW zonal potential energy at a specific altitude and latitude. For a detailed explanation of how to calculate the GW wavenumber spectrum and integrated GW power, Section 3.4.1 has covered this well.

4.2.1 GW Wavenumber Power Spectrum

The time-averaged GW temperature spatial wavenumber spectra at 41 and 71 km along 45°N are shown in blue in Fig. 4.10. They are derived from the GW temperature variation after wave filtering is done. Due to the large scale-separation of both the wavenumbers and the spectral density, GW power density is most conveniently plotted using log-scales on both axes. Although the total range of the spectrum is from planetary-scale waves at low wavenumbers to grid-scale (roughly 20-30 km) at high wavenumbers, the GWs that are possibly resolved in the model are only making up the spectral region where a significant dip in spectral density occurs. The limits of this region are marked by red dashed lines at wavenumbers corresponding to 66 and 500 km. Most GWs of interest will fall into this spatial range. The smallest wavelength is chosen on the qualitative basis of the spectral shape. The flattening of the spectrum at high wavenumbers is a characteristic feature indicating the dominance at small scales of a baseline turbulent noise level. For the spectral analysis of the GWs in this high-resolution version of WACCM-X, this noise is the dominant feature of temperature perturbations smaller than roughly 60-70 km in zonal wavelengths. Below this scale, GWs are not adequately resolved in WACCM-X, so the spectral nature of such small-scale GWs is not possible to infer from this simulation.

The shape of the spectrum is similar to that of turbulence theory, and Kolmogorov Theory [56]. The hypothesis of Kolmogorov states that energy production occurs at the largest scales (lowest wavenumbers) to the left. Then the energy cascades down the scales

as waves break down to smaller scales (or, in the case of turbulence, the breakdown of eddies). This cascade happens in the so-called inertial range, where the log-log slope is the most negative. Thus, the wavenumber region marked in red can be identified as the inertial range of the wavenumber spectrum. Following the hypothesis, at the smallest scales, typically defined by a Kolmogorov length scale, the energy is dissipated by viscous forces as the scales allow them to be dominant. This dissipative region is not visible in the spectra of Fig. 4.10 since the resolution of WACCM-X does not allow for the waves and turbulence of this scale to be resolved.

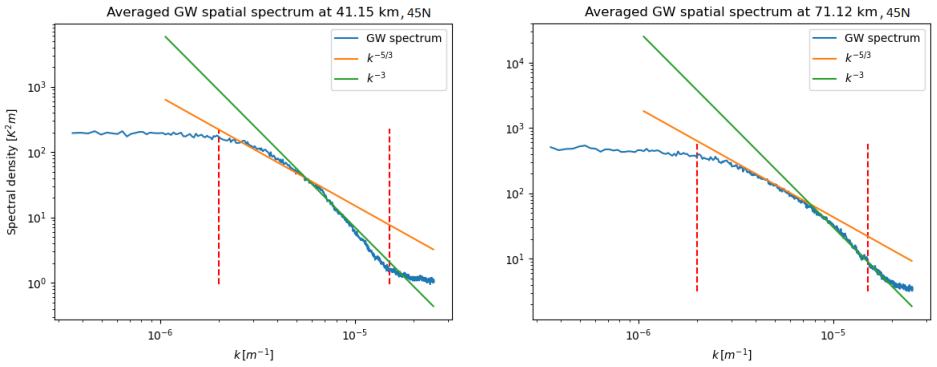

(a) **(b)**

Figure 4.10: The time-averaged GW wavenumber power spectrum for different altitudes at 45°N. The plots in (a) and (b) show the spectra at 41 km and 71 km, respectively. Note the logarithmic scales of both axes. The zonal wavenumber spectrum of the gravity wave temperature signal is marked in blue. Orange and green lines are added to show how the spectrum changes its wavenumber proportionality. Red dashed lines indicate the interval limits of the resolved GW spectrum, excluding white noise (flat region at high wavenumbers) and larger wavelengths than 500 km (flat region at low wavenumbers).

The spectral dependence on the zonal wavenumber is analysed by comparing the slope to those of the green line of $\alpha k^{-5/3}$ and the orange of βk^{-3}, where α and β are proportionality constants. The GW power density is proportional to $k^{-5/3}$ within a certain range at the low wavenumber end of the inertial range corresponding to roughly a wavelength span from 140 km to 330 km. Then, it appears that the exponent decreases towards -3, making the spectrum proportional to k^{-3} in the wavelength range between 66-140 km. Hence, the small-scale waves cascade energy more strongly with decreasing wavelengths than the larger waves. In general, observations typically find the GW spectrum of horizontal wavenumbers to follow a k^p dependence, with p typically valued around -1 to -4, most commonly with a certain range following $p = -5/3$ [39], [18]. This exact value is a universal feature of the inertial range in Kolmogorov turbulence theory, which is also found in GW wave spectra [18], [56]. Hence, the overall spectral results from the simulation agree with observations. Recent spectral analysis using a previous version of high-resolution WACCM also found a clear $p = -5/3$ slope in the horizontal wavenumber power spectrum for wind perturbations. The range was then from zonal wavenumber 10 down to the smallest properly resolved waves of about 250 km (though grid resolution

was 25 km) [30]. Since the wind perturbations at scales typically less than 1000 km are caused mainly by GWs, the power spectrum from temperature perturbations in the same wavenumber range should be similar. Indeed, the findings presented here indicate that the temperature perturbations associated with GWs in WACCM-X show reasonable spectral characteristics.

The wavenumber spectrum does vary in time in terms of shape and power density amplitudes. This time dependence can be explained by GWs being more present and stronger along a section or the whole latitude and altitude at certain times. For example, since GW activity is strong in the stratosphere over the European sector at 45°N early in the dataset, as seen in Fig. 4.7(a), the power density will generally be larger for the corresponding wavenumber region in the GW power density spectrum. What is shown in Fig. 4.10 is the time-averaged spectrum to analyse the general GW spectrum and compare it with those found in literature. However, the time-dependence of the spectrum becomes important when an integrated GW power, proportional to the GW potential energy, is to be found. This power will therefore vary in time in relation to the variation of GW activity.

Comparing the spectral shape with altitude, it is found that the spectral power density is generally larger in the mesospheric GWs. This is consistent with the observations of Figs. 4.7 and 4.8, where the GWs in the mesosphere are generally of larger amplitudes, thus have more potential energy associated with them, and waves are abundant throughout most of the NH atmosphere. Moreover, the variation of p, i.e. the difference between the p values corresponding to the steepest and flattest slopes, seems to be reduced with altitude. In the stratospheric plot, the steepest p corresponds to $p < -3$, while in the mesosphere it corresponds to $p \approx -3$, while it looks like the p value for the flattest slope is the same for both cases. This is consistent with previous findings from WACCM [30].

4.2.2 Integrated GW Power

The total GW potential energy zonally at a specific latitude and altitude is proportional to the integral of the power density of the GW interval of the spectrum. This is calculated, as described in Section 3.4.1, by integrating the power density of the part of the spectrum associated with GWs in the range of 66-500 km, i.e. the integral between the red dashed lines in Fig. 4.10. In a latitude-altitude location of exceptionally high GW activity at a particular time, the overall potential energy, hence the GW power density, will be larger. Thus, the integrated GW power can be treated as a measure of the GW activity zonally at a given latitude, altitude, and time.

The altitude-latitude distribution of GW power is presented in Fig. 4.11 for four times corresponding to the same times as the GW plots in Figs. 4.7 and 4.8. These times (a) 17$^{\text{th}}$ Jan, (b) 26$^{\text{th}}$ Jan, (c) 2$^{\text{nd}}$ Feb, and (d) 9$^{\text{th}}$ Feb, are chosen since they represent different cases of the polar vortex structure and PW stages. The zonal mean zonal wind, with 20 m/s intervals, is overlaid to compare it with the GW power. Note that the scale of the GW power is logarithmic due to the vast span of GW power vertically, caused by the exponential growth of GW amplitudes. Moreover, even though the values of GW powers are rather small, these values are proportional to the GW potential energy through a proportionality factor, which may scale the power properly. In the following, the exact values are not in focus, only the structure and distribution of GW power.

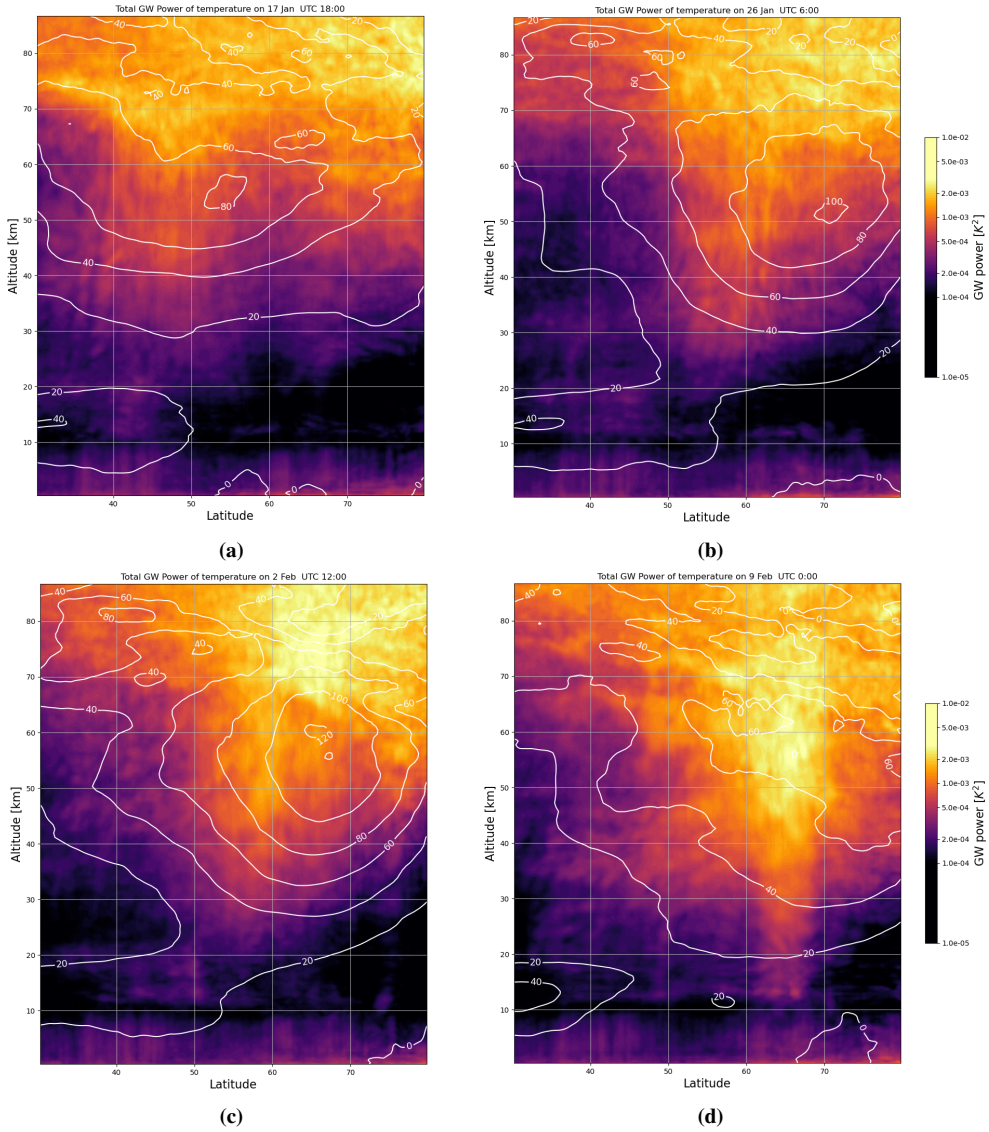

Figure 4.11: The altitude-latitude profile of integrated GW power for four different times, with an overlay of contour lines of zonal mean zonal wind shown in white. The case of 17th Jan UTC 18:00 is shown in (a), 26th Jan UTC 06:00 in (b), 2nd Feb UTC 12:00 in (c) while (d) shows the GW power and zonal mean U on 9th Jan UTC 00:00.

Large GW wavefronts are observed at mid-latitudes on 17th Jan UTC 18:00, with a particular concentration over Central and Southern Europe. This has been seen and discussed in Figs. 4.7(a) and 4.8(a) in Section 4.1.4. Hence, the zonal GW power in the mid-latitude stratosphere and mesosphere should generally be larger than at high latitudes. This is indeed the observation from Fig. 4.11(a). A clear vertical band of large GW power

is seen between 40-50°N, stretching from the tropopause and lower stratosphere up to the upper mesosphere where GW power seems to be large at all latitudes (due to a multitude of waves present). The connection to the tropopause further indicates that the mid-latitude waves are primarily generated by orography at this time, as previously discussed in Section 4.1.4. Note also that at this time, the stratospheric polar vortex edge is located around 45-55°N, but spread out, with a maximum between 80-100 m/s at 55 km altitude 55°N.

Nine days later, on 26th Jan UTC 06:00, the highest intensity of GW power in the stratosphere is now shifted north to about 55-65°N, as seen in Fig. 4.11(b). This is where a significant portion of GWs are seen over the North Atlantic and Scandinavia in Figs. 4.7(b) and 4.8(b). The GW power at 45°N is now much lower, as expected. Note that in the upper mesosphere, above 70 km, it is also apparent that high-latitude GW power is much stronger than mid-latitude power. Note also that the polar vortex has now shifted north and strengthened significantly, centred about 60-75°N, with a maximum of 100-120 m/s at 70°N. The stratospheric maximum of GW power is located somewhat south of this vortex maximum, while the mesospheric maximum of GW power occurs directly above the vortex.

Fig. 4.11(c) shows the GW power during the late stage of the strong polar vortex on 2nd Feb UTC 12:00. Note that the maximal zonal mean zonal wind exceeds 120 m/s at 65°N, indicating a very strong vortex. Notice also the very strong GW power in the upper mesosphere directly above the vortex maximum, similar to the week before, although significantly stronger. The maximum GW power in the stratosphere is still located around 55-65°N, again similar to the previous week. It is also interesting to note that there is little lower-stratospheric and tropospheric GW power at high latitudes. Hence, this suggests that non-orographic GWs dominate at high latitudes during the excessively strong polar vortex case. The large GW power directly north, south, and above the maximal zonal mean zonal wind could indicate generation of waves occurs in the vicinity of the polar vortex. A study by Becker and Vadas regarding GWs in a strong polar vortex wind and with strong PWs in the Southern Hemisphere winter found that GWs are often intense and have large phase speeds high up in the mesosphere, directly above the maximum of the zonal mean zonal wind, in parallel to the case in the NH Winter here [6]. However, it was argued that such waves of those phase speeds would not survive an upward propagation through the excessively strong vortex. Hence, the conclusion of Becker & Vadas was that the GWs must be generated in the middle atmosphere. It is reasonable to believe this is the case here too.

Lastly, Fig. 4.11(d) shows the GW power and zonal mean zonal wind contours on 9th Feb UTC 00:00. In this case, the polar vortex is significantly weakened, with a maximum of only 60-80 m/s, but spread out without a narrow and distinct maximum wind region. The strongest GW power is located between 60-70°N, with a maximum at around 60-75 km. Furthermore, a clear vertical band of strong GW power reaches down to the troposphere. This suggests orography is a major source of GWs at this latitude and time. A similar conclusion is made from the GW plots in Figs. 4.7(d) and 4.8(d), as well as the plot of vertically-standing orographic GWs east of Greenland at 65°N in Fig. 4.9(a). Hence, a significant source of GW power at this latitude and time is orographic GWs at high latitudes. Such waves can only propagate upwards in a moderate eastward wind regime. In contrast to the excessively strong zonal mean zonal wind case on 2nd Feb, there

are now significant instabilities in the polar vortex, as previously indicated by the jet plots in Fig. 4.3(d). The weakening of the zonal mean wind in combination and the unstable and wobbly polar vortex edge occurs, while orographic GWs seem to appear around this region in the late-stage breakdown of the vortex. However, the mesospheric GW power is generally strong at high latitudes, indicating that non-orographic GWs may also be largely present.

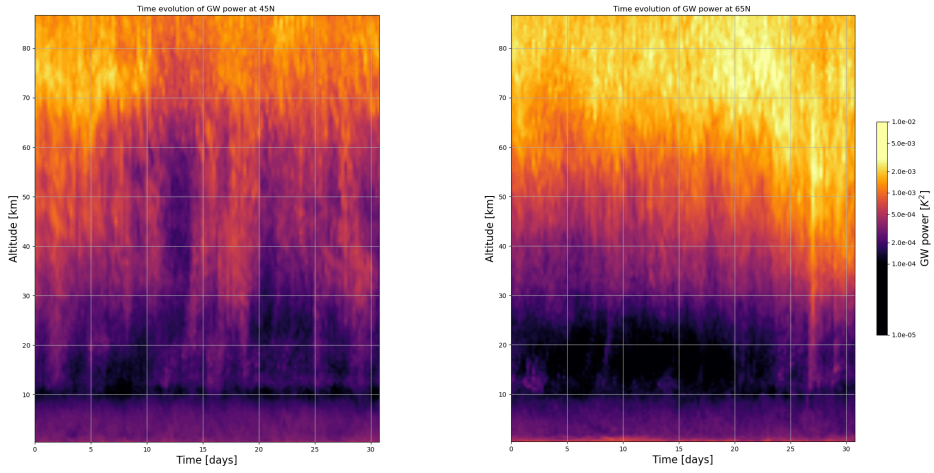

(a) 45°N

(b) 65°N

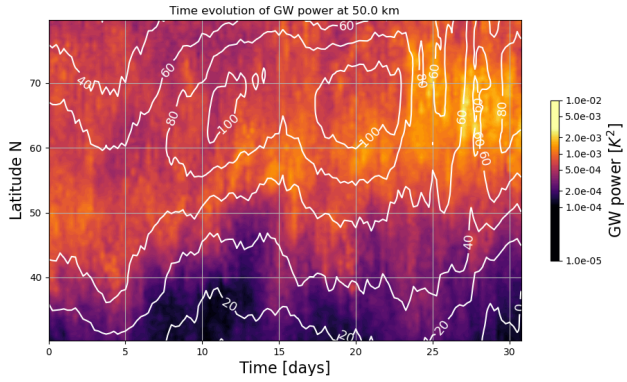

(c) 50 km

Figure 4.12: Hovmöller diagrams for GW power, for the same cases as in Fig. 4.2. The upper two plots show the altitude-time diagram of GW power at (a) 45°N and (b) 65°N. Fig. (c) shows the GW power in a latitude-time diagram at 50 km, i.e. close to the maximal zonal mean zonal wind in the polar vortex. Contour lines of zonal mean zonal wind are marked in white for the latter plot with intervals of 20 m/s.

Overall it is clear that the latitudinal position of the maximum GW power at any altitude varies with time in a pattern that seems related to the polar vortex. This could indicate that there is a possible link with either the position and strength of the polar vortex,

PWs that typically are strong around the vortex edge, or both. Moreover, the correlation between GW power and the zonal mean zonal wind is investigated in Section 4.5 and Fig. 4.18(b).

Hovmöller diagrams of GW power are shown in Fig. 4.12, with (a) and (b) showing the altitude-time diagram for 45°N and 65°N respectively, and (c) shows the latitude-time diagram for 50 km altitude. These diagrams correspond to those of Fig. 4.2 for the zonal mean zonal wind.

From the altitude-time diagrams of Figs. 4.12(a) and (b) a striking observation is the low GW power in the lower stratosphere at high latitudes. In contrast, at 45°N, one may observe vertical lines of strong GW power. These go all the way up from the upper troposphere and lower stratosphere to the upper mesosphere. Hence, the overall finding is that there is predominantly orographic GW generation at mid-latitudes in this simulation, though non-orographic waves may be present here too. On the other hand, looking at 65°N, the lower-stratospheric GW power is weaker than at mid-latitudes in the middle days (day 10-20), while the upper-stratospheric and mesospheric power is significantly stronger than at mid-latitudes. In other words, there appears to be little wave activity from the troposphere at high latitudes during an excessively strong polar vortex, suggesting the GWs originate somewhere in the middle atmosphere rather than from orography on the ground.

From Fig. 4.12(c), it is clear that the maximum GW power at 50 km altitude moves northward during days 5-15 (17^{th}-27^{th} Jan), and 20-25 (1^{st}-6^{th} Feb). The zonal mean zonal wind contour lines in white illustrate that the polar vortex also moves north, with a remarkably similar trend during the same time period. This indicates that GW power tends to follow the polar vortex in the middle atmosphere. Knowing that the vortex is strong during the middle days and located far north leads us to believe it is critical in generating GWs in the middle atmosphere. However, the role of PWs in this must be further studied to understand the mechanism of GW generation better, as these are known to be crucial for GW propagation and filtering in the middle atmosphere and generating strong shears.

4.3 Planetary Wave RMS Amplitudes

To compare PWs with the GW power, which is roughly a measure of the zonal GW potential energy, a zonally-averaged quantity of PWs must be found. From the plots of PWs in the horizontal and vertical atmosphere in Figs. 4.4 and 4.5 in Section 4.1.3, it is clear that the amplitudes of the temperature-based PWs vary in time, and show signs of amplifying while the polar vortex is strong. Hence, a zonally-averaged measure of the PW amplitudes could be suitable for comparisons with GW power. This is done by calculating the root-mean-square (RMS) value of the PW temperature signal zonally at a fixed altitude, latitude, and time. It is worth mentioning that a PW power could have been calculated similarly to the GW power described and derived earlier. However, the PW power would be proportional to the PW potential energy, which is related to the amplitudes of the PWs. Hence, both are valid. Here PW RMS T is chosen as the PW quantity since it is easier to calculate than the power.

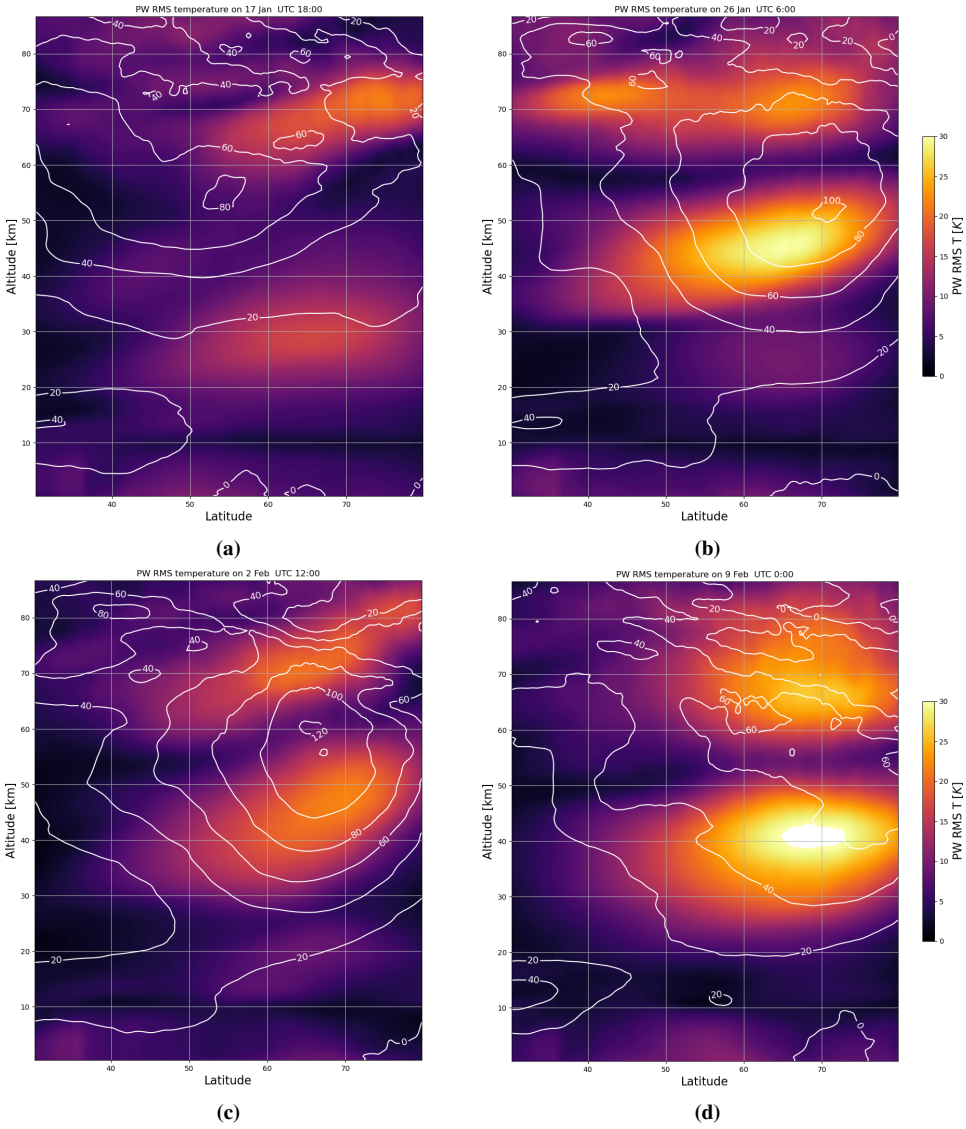

Figure 4.13: The altitude-latitude profile of PW RMS temperature for four different times, with an overlay of contour lines of zonal mean zonal wind shown in white. The case of 17th Jan UTC 18:00 is shown in (a), 26th Jan UTC 06:00 in (b), 2nd Feb UTC 12:00 in (c) while (d) shows the PW RMS T and zonal mean U on 9th Jan UTC 00:00. The contour interval for zonal mean zonal wind is 20 m/s.

The altitude-latitude profiles of PW RMS temperature for four different times are plotted in Fig. 4.13, with contours of zonal mean zonal wind marked by white curves. The times correspond to those for GW power in Fig. 4.11, meaning (a) 17th Jan UTC 18:00, (b) 26th Jan UTC 06:00, (c) 2nd Feb UTC 12:00, and (d) 9th Feb UTC 00:00. The unit of

the PW RMS T is K, and the range is from 0 to 30 K, although for a brief moment on 9th Feb, the PW RMS T exceeds 30 K in the high-latitude stratosphere.

The first thing to notice in the plots of Fig. 4.13 is the apparent concentration of large-amplitude PWs in the stratosphere and mesosphere separately. This is consistent with the structure of the temperature PWs, as was presented for the case of 26th Jan in Fig. 4.5. There, PWs typically stack onto one another, in one large stratospheric wave and one large mesospheric wave of opposite phases. In between, the PW amplitudes are weaker. It is also similar to PW RMS T plots from observations for January, though for quasi-stationary 16-day WN1 PWs only, which is likely a significant component in the PW signal anyway during the NH winter stratosphere [25].

Secondly, Fig. 4.13 indicates that the PW amplitudes increase significantly between 17th Jan (day 5) and 26th Jan (day 14), during the northward motion and strengthening of the polar vortex. The amplitude increase occurs in both the mid-latitudes and high-latitudes in the stratosphere, while mainly in the mid-latitudes only in the mesosphere. Additionally, it is worth noting that the maximal PW RMS values in the stratosphere seem to be shifted upwards during this amplitude increase, with a vertical shift of about 15 km and a slight northward shift between Fig. 4.13(a) and (b). Furthermore, the location of the maximal PW RMS T is close to the maximal zonal mean zonal wind in the upper stratosphere on 26th Jan. These observations may indicate that the strengthening of the polar vortex and an increase of PW amplitudes in the vicinity of the vortex are related.

Interestingly, it appears that the PW amplitudes decrease from 26th Jan (day 14) in (b) to 2nd Feb (day 21) in (c), even though the polar vortex remains fairly strong, but with a short weakening and strengthening phase occurring within this time. Furthermore, a strong increase in PW amplitudes follows from 2nd Feb in (c) to 9th Feb (day 28) in (d). This occurs while the vortex destabilises, loses its structure, and weakens significantly. The stratospheric PW RMS maximal point is slightly shifted down in altitude, although still considerably higher up than during the early stage of the simulation. The PW RMS temperature here exceeds 30 K, the strongest in the month-long interval. Hence, taking the strong PW amplitude increase from 17th to 26th Jan into account as well, there are indications that the changes in the polar vortex strength are linked to the strengthening of PW amplitudes.

The Hovmöller plots of Fig. 4.14 further suggest that at high latitudes, e.g. 65°N in (b), there appear to be two distinct stratospheric PW RMS maxima in time. These occur around days 10-15 (22nd-27th Jan) and days 22-29 (3rd-11th Feb). This is also visible in the latitude-time plot at 50 km altitude in (c), where the northward migration of PWs and polar vortex also can be seen. Furthermore, the altitude-time plot at 45°N in (a), as well as the latitude-time plot in (c) both indicate that in the mid-latitudes, only the first amplification of PWs during days 10-15 occurs. Also, the second amplification on days 22-29 is much weaker at mid-latitudes. Hence, in the northward migration and strengthening of the polar vortex, the PWs at all latitudes are amplified. In contrast, in the destabilisation and weakening of the vortex on days 22-29, only the high-latitude PWs seem to be affected, which is also the location of the vortex maximum.

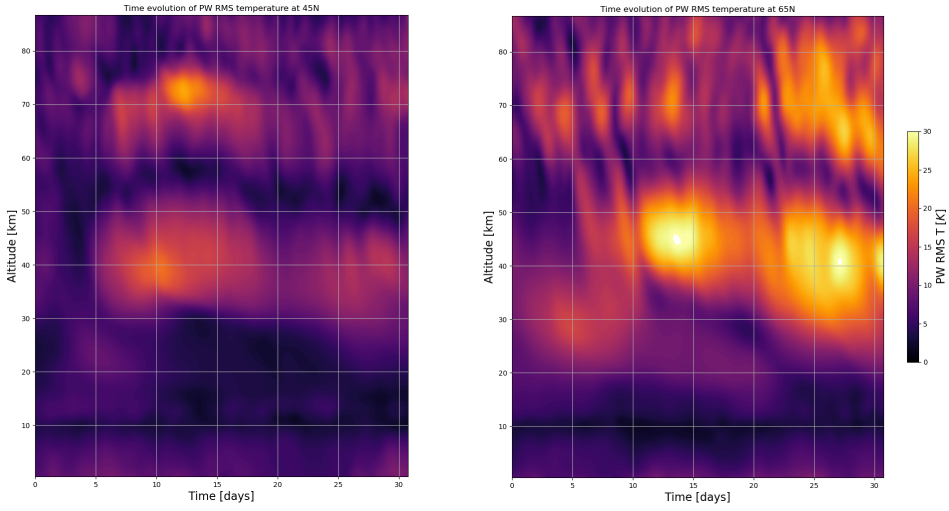

(a) 45°N **(b)** 65°N

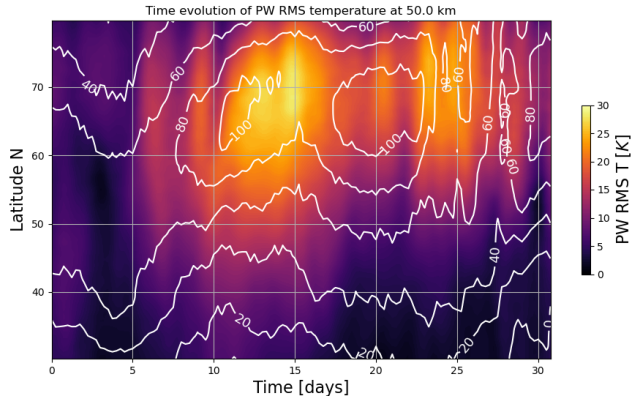

(c) 50 km

Figure 4.14: Hovmöller diagrams for PW RMS temperature.. The upper two plots show the altitude-time diagram of GW power at (a) 45°N and (b) 65°N. Fig. (c) shows the PW RMS T in a latitude-time diagram at 50 km, i.e. close to the maximal zonal mean zonal wind in the polar vortex. Contour lines of zonal mean zonal wind are marked in white for the latter plot.

A possible explanation of the first amplification of PWs during days 10-15 is that PWs from the troposphere and lower stratosphere can propagate upwards along the weak polar vortex edges over Europe. This affects the vortex edge and moves it northwards while the PWs may grow in amplitude. Indeed, as mentioned when concerning the vertical profiles of PWs in Fig. 4.5(a)-(b), the PW tilt on 17th Jan may indicate propagation of PWs from the troposphere below. This allows the stratospheric waves to grow and could also trigger a vortex instability that causes the vortex to shift northward, as PWs are known to do so when amplified by tropospheric PWs below [21]. The process could likely be further amplified as the substantial northward shift and strengthening of the vortex generate zonal

temperature and wind variances on its way, contributing to the PWs. From the polar vortex wind jet profiles in Fig. 4.3, it is known that the vortex changes its shape and centre throughout the interval. Since the vortex edge is observed to wobble rapidly during its northward migration, substantial zonal variations occur, that manifest as PWs.

The slight dampening of PW amplitudes in the stratosphere during days 15-22 (27th Jan to 3rd Feb) occurs during the strongest zonal mean zonal wind, right before the substantial weakening of the vortex. This could indicate that the PWs break when reaching the large amplitudes on day 15, causing PW drag on the mean flow. Since the mean flow decelerates only after the dampening of the wave amplitudes occurs, it could indicate a lag from wave breaking to mean flow interaction, particularly for such a strong vortex. In fact, PWs are known to strongly deform and weaken the polar vortex by applying drag to the wind, if the PW amplitudes are strong [21].

As is now known from the above presentation and discussion, the polar vortex experiences a significant destabilisation, starting from day 22 (3rd Feb). Looking at the polar vortex edges in the wind plot at 41 km from Fig. 4.3, the vortex shifts south towards Europe again, with a rapidly wobbling jet. This strong destabilisation may cause the vortex to shed PWs, and due to the rapid loss of kinetic energy in the polar vortex due to reduced wind strength, this energy may pump into the newly generated PWs. Hence, the PW amplitudes become large again close to the polar vortex. Such a mechanism of PW amplification from a weakening and unstable polar vortex has been proposed and is called a ”spontaneous adjustment” of the vortex as an equilibrium mechanism [46]. When the vortex is excessively strong beyond its stable equilibrium state, the theory goes that it reduces the vortex energy and momentum by shedding waves, particularly PWs, but also GWs, that become prominent as the polar vortex jet wobbles. From the discussion above, there are strong indications that such a spontaneous adjustment mechanism occurs for the vortex in this dataset, generating PWs, and some GWs, to gain stability. That should not come as a surprise, given that spontaneous adjustment events are reportedly found in previous runs using earlier WACCM models [32].

4.4 Temporal Spectral Analysis of GW Power, PW RMS T and Zonal Mean Zonal Wind

As described in section 3.4.2, the Generalised Lomb-Scargle (GLS or LS) method is used to study the frequency spectra of GW power, PW RMS T, and zonal mean U. For convenience, the frequency is converted to the period in all of the following discussion. A temporal spectral analysis aims to understand what periods are present in the signals, and their spatial location in altitude and latitude. Comparing the LS spectra for GW power, PW RMS T, and zonal mean U can further indicate any interaction or relation between them, particularly if any similar periods are found.

The LS periodograms in the stratosphere at 41 km altitude, at 45°N are shown in Fig. 4.15 for (a) GW power, (b) PW RMS T, and (c) zonal mean U. All have peaks surpassing the 1% False Alarm Probability (FAP) level, marked by the red dashed line. Hence, these peaks have less than 1% chance of resulting from noise.

The GW power has a notable peak centred around a period of 12 days. This aligns

with the findings in Fig. 4.12(a), which indicates a recurring 12-day intensification of GW power at this specific altitude and latitude. Upon closer examination of the GW plots at this altitude and latitude, it appears that this period most likely occurs due to tropospheric generation of GWs at different longitudes for different times. These occur when an eastward PW wind, closely related to the polar vortex edge, is located above mountainous regions along the 45°N latitude. For example, around 15th-18th Jan, the orography-generated GWs over Central Europe dominate, while on 27th-30th Jan, most waves at this altitude and latitude are located in the Northeast of Japan. However, some weakly increased wave activity occurs in Europe too. In both cases, a moderately strong stratospheric polar vortex edge with moderate eastward PW winds can be observed at these two locations.

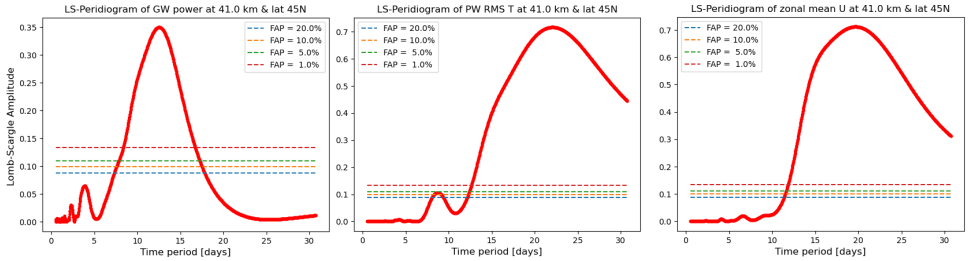

Figure 4.15: Lomb-Scargle periodograms for (a) GW power, (b) PW RMS T, and (c) zonal mean zonal wind at 41 km, 45°N. Dashed lines mark False Alarm Probability (FAP) levels. The red dashed line indicates the 1% FAP level.

For both PW RMS T in Fig. 4.15(b) and zonal mean U in (c), there is a broad, significant peak around 15-25 day periodicity at 45°N and 41 km altitude. They are similar in width, centring, and LS amplitude. The similarities do not necessarily imply any relationship between them. However, it does align with the discussion of PW generation from the migration, wobbling, and instability of the polar vortex edges as presented at the end of Section 4.3. In studies of oscillations in the vortex streamlines at mid-latitudes, findings suggest a 20-day oscillation of the vortex edges at mid-latitudes sometimes occurs during winter, associated with the PJO [23]. It is found that the periodicity of the edge is strongest over Europe and Western Asia during winter. This is because of the typical displacement of the polar vortex towards Europe in the winter, favouring a vortex edge above Central Europe. Moreover, similar 20-day variations in stratospheric ozone over Central Europe have been linked to PW activity [11]. It is also found that when PWs generate and amplify, they also may displace the polar vortex [21]. Hence, the similar 20-day periodic peaks of PW RMS T and zonal mean zonal wind at 45°N, 41 km altitude may indicate this vortex-PW mechanism in the winter mid-latitude middle atmosphere.

It is important to stress that for a month-long dataset, there are a limited number of cycles of the long-period signals. For a 20-day periodicity of a 31-day dataset, only 1.5 cycles fit. Hence, there are uncertainties about whether this periodicity is general or a one-time occurrence in the model simulation.

A last remark of Fig. 4.15(b) is that there are signs in the periodogram of a peak

around 14-16 days for the PW RMS T, that is merged with a longer-period peak. This is indicated by a slight break of the smooth curve, from very steep around 13-16 days, followed by a less steep curve. This peak is likely a trace of the 16-day quasi-stationary PWs of WN1 that are typically present in the NH winter stratosphere [25]. These waves have been known to modulate GWs, particularly in the MLT during NH winters [35].

It is possible to generalise the LS periodograms shown in Fig. 4.15 to simultaneously display LS amplitudes and significant periods for different altitudes or latitudes. This involves calculating the LS periodogram separately for each altitude/latitude at a specific latitude/altitude and presenting the peaks as coloured contours in an altitude-period or latitude-period plot. To easier see where peaks of 99% statistical significance are located, only the amplitudes above the 1% FAP level are plotted. The latitude-period plots of the significant LS amplitudes are shown in Fig. 4.16, for an altitude of 41 km. Similarly, the altitude-period plots are shown in Fig. 4.17, for latitude 45°N in (a)-(c), and 65°N in (d)-(f).

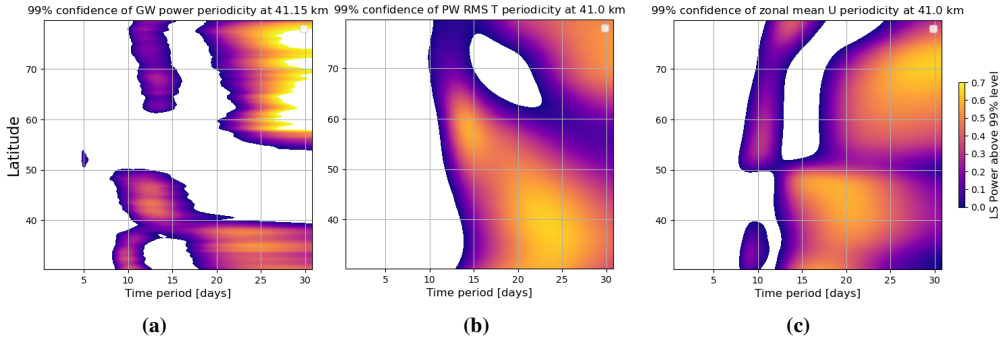

Figure 4.16: Latitude-period plot for the Lomb-Scargle amplitudes surpassing the 99% confidence level, for (a) GW power, (b) PW RMS T, and (c) zonal mean zonal wind at 41 km altitude. The plots show the signals' significant (p=0.01) periods at different latitudes.

On the latitude-period LS plot displayed in Fig. 4.16, the significant LS amplitudes at 41 km reveal that GW power experiences a notable 10-15 day peak at 45°N as well as in the majority of mid- and high-latitudes. This peak is also present vertically in most of the middle atmosphere in the altitude-period plots of Fig. 4.17(a) and (d), at 45°N and 65°N respectively. However, the significance and LS amplitudes are generally more prominent in the mid-latitudes. The vertical bands from the troposphere and up further suggest that this periodicity is likely associated with orography-generated GWs at different locations close to the polar vortex edges, giving a roughly 12-day periodicity of the zonal GW power. However, whether there is a PW interaction in this signal, is unclear from the LS periodograms alone.

There is also a broad long-period peak of 20+ days of GW power at high latitudes and altitudes. It is present all along the middle atmosphere at 65°N as a 30-day peak. The location could indicate that the stratospheric and mesospheric GWs in the high latitudes vary slowly, or that they look periodic in the dataset due to a single maximum peak occurring in the 31-day long simulation, as seen by the GW power Hovmöller plots in Fig.

4.11. The long-period variations could result from non-orographic GWs possibly linked to the spontaneous adjustment event of the vortex at high altitudes and latitudes. Both PW amplitudes and the zonal mean zonal wind also show long-period variations at similar altitudes and latitudes. However, the short length of the dataset restricts the discussion of these long-period signals, due to significant uncertainties.

Some interesting observations can be inferred from the latitude/altitude-period LS amplitude plots in Figs. 4.16(b), 4.17(b) and (e). For example, there seems to be a dominant long-period PW amplitude variation of roughly 20-30 days in the mid-latitude stratosphere, with a 20-day periodicity at 45°N 41 km, as previously discussed. However, the most significant period shortens with increasing latitude, becoming a 14-16 day oscillation of PW amplitudes at 60°N 41 km. Why this is the case, is difficult to answer from this analysis alone. Overall, the vertical LS profiles show the dominance of long 20-30 day periods in the PW RMS T signals in the middle atmosphere, especially in the mid-latitudes. This may be associated with large-amplitude PWs being generated at the polar vortex edges, which have been argued may cause a 20-day variation as the vortex centre moves between the Pole and high latitudes of the European sector.

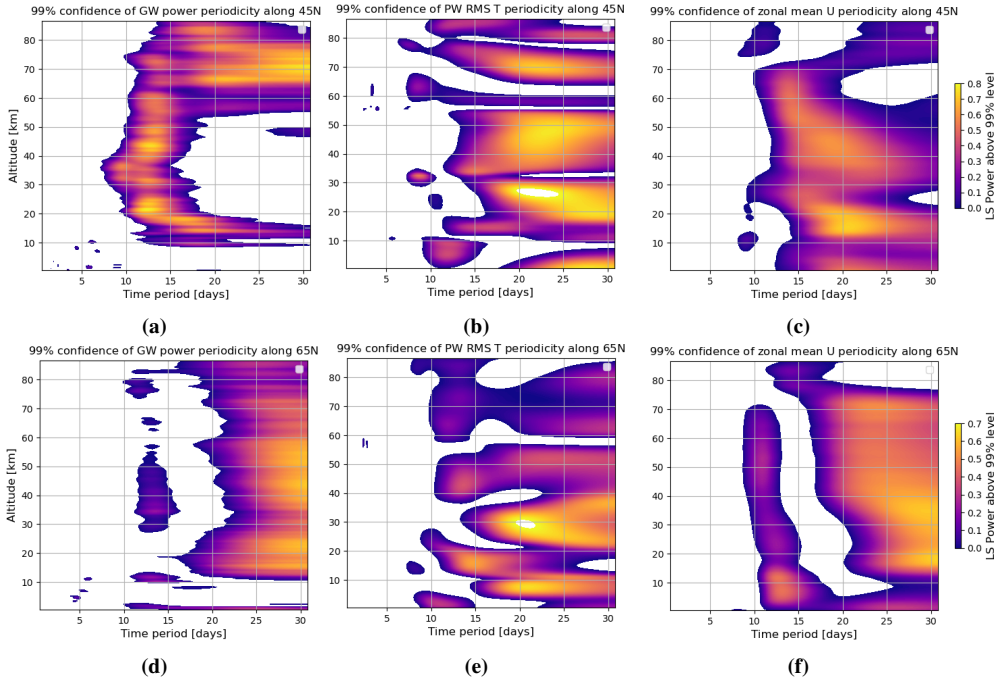

Figure 4.17: Altitude-period plot for the Lomb-Scargle amplitudes surpassing the 99% confidence level, for (a) & (d) GW power, (b) & (e) PW RMS T, and (c) & (f) zonal mean zonal wind at 45°N (upper) and 65°N (lower). The plots show the signals' significant (p=0.01) periods at different altitudes and highlight differences between the two latitudes.

Overall, the LS periodograms and vertical and latitudinal LS profiles indicate that PW amplitudes and zonal mean zonal winds could be related in periods by the 20-day

oscillations in the polar vortex edges, particularly in the mid-latitudes. Furthermore, GW power shows a 12-day period at mid-latitudes from the tropopause and up to the middle mesosphere, most likely caused by bursts of troposphere-generated GWs at different locations when the polar vortex edge happens to rapidly wobble at that location. While the GW generation at a specific mid-latitude location is only weakly 12-day periodic, the strong 12-day period in the GW power is due to different GW generations. At both high latitudes and high altitudes GW power oscillates with long periods of 20+ days. The same goes for the zonal mean U and to some extent PW RMS T. However, whether there is a link between the GW power and the background wind and PW amplitudes needs to be clarified and needs further investigation.

4.5 The Effect of Planetary Waves on Gravity Waves During A Polar Vortex Spontaneous Adjustment Event

The above presentation and discussion of the atmosphere, GWs, PWs, polar vortex, GW power, and PW RMS T, begs the question: Is there a link between GW power and PW amplitudes? It is well-established by the discussion and results above that the PWs are most likely linked to the migration, instability, and wobbling of the polar vortex. PWs can both cause a polar vortex displacement and can be generated by an excessively strong vortex that tries to regain a stable vortex equilibrium. Hence, it is now reasonably clear why and how the PWs appear. However, this is only the first step in understanding how GWs are affected by PWs. Now a relation between PWs and GWs must be made, if there is any.

The previous discussion, particularly from Sections 4.1.4 and 4.2, suggests that some GWs are generated in situ in the stratosphere. This occurs during intense PW activity. Increased GW activity is also visible close to the meandering polar vortex edges, which is also where strong PWs are generated. This could be partly due to the generation of GWs in the spontaneous adjustment of the vortex, but may also be enhanced by the PWs. One way to measure whether there is a trend between GW power and PW RMS T is to calculate their time series correlation. It does not necessarily say anything about whether there is true causality. Although, in light of the discussions above, it could indicate whether there is a good chance to believe any interactions occur. However, first it has to be established whether there are any correlations between GW power and the zonal mean zonal wind, as well as the latter vs PW amplitudes.

4.5.1 On the GW Power and PW RMS T Correlations With Zonal Mean Zonal Wind

The zonal mean zonal wind, PWs and GWs may all be linked. No causal links can be safely drawn about a possible PW-GW interaction without first investigating how the zonal mean zonal wind correlates with PW amplitudes and GW power. Hence, the following paragraphs revolve around Fig. 4.18 where such correlation profiles are given.

As already well-established by the discussion and results in the previous sections, PWs are most likely caused by the migration, strengthening, wobbling, and subsequent

weakening of the polar vortex. Additionally, middle-atmospheric PWs are probably amplified by the propagation of PWs from below. A correlation plot between the PW RMS T and the zonal mean zonal wind is shown in Fig. 4.18(a). There is a strong anti-correlation in the mid-latitude stratosphere and lower mesosphere, while there is a strong correlation at high latitudes. The polar vortex wind is strongest (but not particularly strong overall) in the mid-latitudes at the beginning of the dataset during weak PW activity, and weaker when PW activity is strong. Oppositely, at high latitudes, the PW activity is generally very strong during strong zonal mean zonal wind. Generally, the zonal mean zonal wind is the strongest when the vortex is far north. PWs amplify both at mid- and high latitudes while the vortex grows in strength at high latitudes due to the vortex PW amplification. Indeed, it has been observed that PW amplitudes in the vicinity of the vortex are enhanced when the polar vortex strength is large [11]. This explains the in-phase zonal mean zonal wind vs. PW correlation at high latitudes only, while anti-correlation occurs in the mid-latitudes. Hence, the strongly positive correlation at high latitudes is most likely related to the spontaneous generation of PWs in a polar vortex spontaneous adjustment. However, PWs also exist at mid-latitudes, and become amplified there too. As they are close to the polar vortex edge, but far south from the strongest zonal mean zonal wind, there is an anti-correlation here. This strongly indicates that PW amplification is a crucial consequence of polar vortex vacillations.

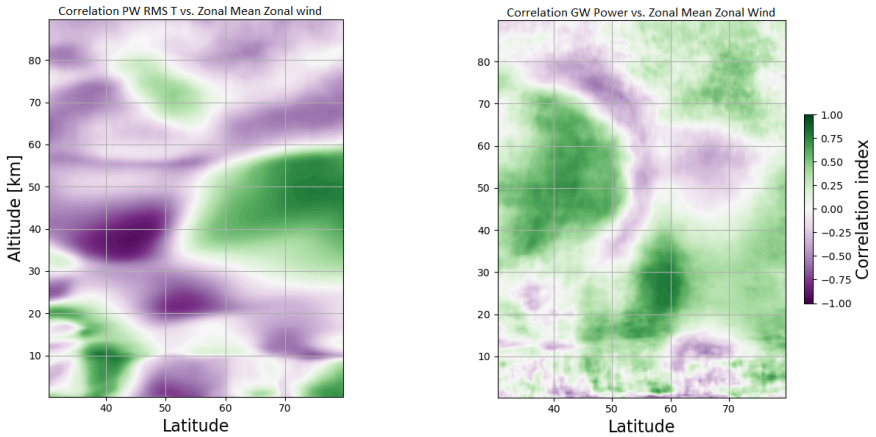

Figure 4.18: Correlations with the zonal mean zonal wind. Altitude-latitude correlation profile for (a) PW RMS T vs. zonal mean zonal wind, and (b) GW power vs. zonal mean zonal wind.

An exception occurs during the final polar vortex weakening at high latitudes when PWs are strongly amplified and the zonal mean zonal wind is only moderately strong. This does not align with the correlation at high latitudes and is likely a weakening factor for the correlation index. However, this event is caused by the spontaneous adjustment mechanism of the vortex. As a second vortex strength maximum is reached in the late stage, the polar vortex starts a spontaneous adjustment event, where the excessively strong vortex strength becomes unstable and sheds energy into PW generation and amplification

while the vortex edge starts wobbling rapidly due to vortex instability. Indeed, for the case study of the 2016 January stratosphere over Europe, a significant amplification of WN1 PWs occurred during a polar vortex breakdown [15]. Although the dampening of the vortex strength in the WACCM-X simulation is not as extreme as the 2016 case, it still manifests similar WN1 PW amplifications during the vortex weakening.

The GW power correlation with the zonal mean zonal winds in Fig. 4.18(b) indicates that GW power tends to correlate with the background zonal wind. However, the correlation is generally weak and less systematic in structure than in the previous case. At mid-latitudes, a correlation in the middle atmosphere indicates that the GWs here typically propagate through this region when the zonal mean wind is moderately strong (as opposed to weak). Most GWs here may be associated with orography-generated GWs that occur when the polar vortex is located far south causing moderate zonal wind jets above mountain ranges. This is backed by observations of MWs over Europe in a far-south-centred vortex case of January 2016, as well as other similar events [9], [14], [23].

There is an anti-correlation of GW power vs. zonal mean zonal wind at 50-60 km altitude between 60-70°N. This is a result of the excessively strong polar vortex maximal wind being located in this region for a longer time, which becomes too strong to allow for GW propagation through this region, as observed in altitude-latitude profiles of GW power in Fig. 4.11.

The strong polar vortex wind, and closely related PWs associated with the vortex edge, may cause large wind shears around the vortex maximum wind. Indeed, in a spontaneous adjustment, the vortex may shed GWs. This could explain the positive correlation of GW power vs. zonal mean zonal wind in the mesosphere, above the vortex maximum wind. Hence, the vortex may be a source of upward- and downward-propagating GWs. However, as known, PWs play a crucial part in the vicinity of the polar vortex, so the vortex itself is not necessarily the single cause of GW generation. It remains to investigate the correlation of GW power vs. PW RMS temperature.

4.5.2 On the Correlation of GW Power With PW RMS Temperature

The correlation between GW power and PW RMS temperature is presented in Fig. 4.19. The figure shows the correlation index in the interval from -1 (anti-correlation) to +1 (correlation) in the latitude-altitude plane between 30°-80°N and 0-88 km altitude. Interestingly, the correlation is remarkably structured, separated into mid-latitude and high-latitude, as well as stratospheric and mesospheric domains.

The mesospheric domains can be explained by the fact that the PWs and GWs here, hence the PW RMS T and GW power, largely depend on what happens in the stratosphere. Since there are indications that PWs propagate upward, mesospheric PWs are formed and stacked upon the stratospheric, as previously seen in Fig. 4.5. The phases are opposite, and their amplitude is weaker than the stratospheric PWs. There is a strong connection between the mesospheric and the stratospheric PWs. In fact, a strong correlation between them is known from earlier studies [26]. Hence, there is a link between the increase and decrease of PW amplitudes in both regions. On the other hand, GWs that are generated below may propagate up to the mesosphere, where they typically break. Therefore, the total GW power in the mesosphere is strongly influenced by GWs in the stratosphere. However, more variability is involved, as GWs have various sources and may be filtered

in the stratosphere. Overall, this explains why there is a mirroring of the stratospheric correlation in the mesosphere. The significant source variability in GWs and their breaking may explain the weaker correlation indices in the mesosphere. However, it remains to explain the stratospheric correlations.

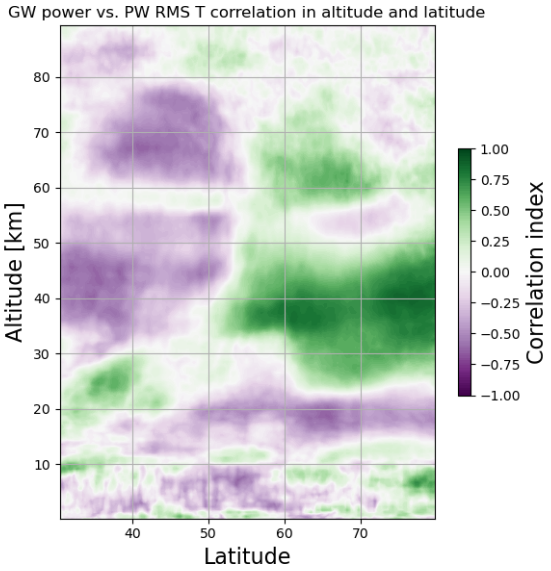

Figure 4.19: A 2D view of the cross-correlation between temperature-based GW power and PW RMS amplitude temperatures between heights 0-88 km and latitudes 30°-80°N. The correlation index is normalised to the interval [-1,1]. What stands out is the apparent correlation in the high-latitude stratosphere and mesosphere, with a clear separation between the two layers, while anti-correlations are present in the mid-latitudes with similar layer separation.

The stratospheric correlation profile indicates that at high latitudes, north of around 50-60°N, GW power correlates with the PW temperature amplitudes. The correlation index is generally around 0.40-0.80 in this region between 25 and 50 km altitude. The correlation is therefore moderate in most of this region. However, with the data at hand and knowing from the previous section that long periods are involved, the correlation is somewhat uncertain. The systematic correlation in the high-latitude stratosphere may suggest that the GW power and PW amplitudes are indeed related. Based on the data depicted in Figs. 4.12 and 4.14, it has been observed that during days 10-17 (22^{nd}-29^{th} Jan) and 23-31 (4^{th}-12^{th} Feb), when PW amplitudes are high in the high-latitude stratosphere, there is a corresponding increase in stratospheric GW power. Hence, the GW power, proportional to the total amount of GW potential energy zonally, in the high-latitude stratosphere is correlated to the amplitude of the temperature-based PWs.

The correlation in the high-latitude stratosphere can also be somewhat inferred from looking at the Hovmöller diagram for time-mean-subtracted GW power variations (coloured) and the PW RMS T (contours) at 41 km altitude in Fig. 4.20. For example, at 60°N, the GW power is above average for that latitude and altitude during days 10-17 and 25-31, coinciding with the above-average PW amplitudes. Moreover, at 70°N, both GW power

and PW RMS T are below average in the first half, and above average in the latter days, with both peaking around days 25-31.

On the other hand, in the mid-latitudes from around 50°N, and southward between 30-55 km altitude, there is a moderate anti-correlation between the GW power and the PW RMS temperatures. When GW power tends to be high, the PW amplitudes are generally low, and vice versa. Again, this is observed in the Hovmöller plot of GW power variations in time vs. PW RMS T variations at 41 km, in Fig. 4.20. For example, at 45°N, the GW power is above average during the first five days when most of the waves are MWs generated orographically over Southern and Central Europe and in parts of Siberia. Meanwhile, the PW amplitudes are below average, indicated by the negative PW perturbation from the average PW amplitude. Between days 7-15, GW power is generally below average, while PW RMS temperature amplitudes are above average. The trend continues to some degree. Although, knowing the temporal spectral characteristics of the signals, the GW power has a dominant 12-14-day period at this altitude and latitude, while the PW amplitudes have a broad range of long periods in the range of 15-30 days. The anti-correlation could weaken if a longer dataset is studied since the dominant periods do not match.

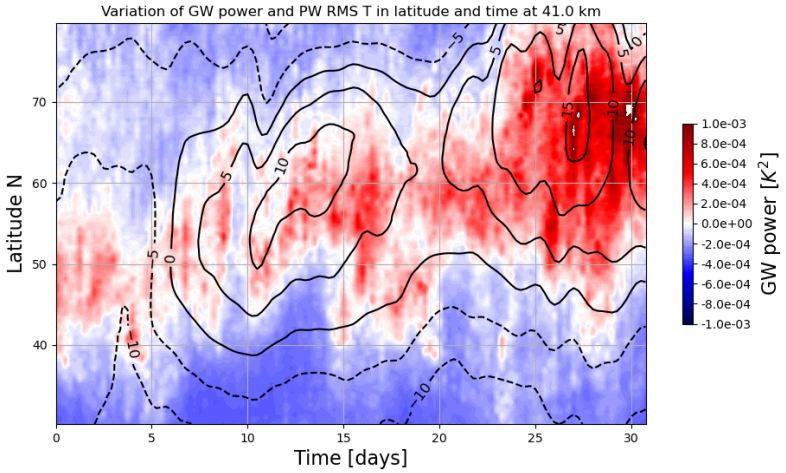

Figure 4.20: Hovmöller latitude-time diagram of time-mean-subtracted GW power variation (coloured) and time-mean-subtracted PW RMS T variation (contours from -15 to 15 K with 5 K spacing) at 41 km altitude. The mean-subtraction is done to highlight the coincidental variations in GW power and PW RMS T.

The correlation plot of GW power vs. PW RMS temperatures in Fig. 4.19 is a central result. It does show regions of correlations and anti-correlations, in such a systematic way as to suggest some interaction or modulation occurs. This is further backed by the Hovmöller plot of Fig. 4.20. In contrast to the GW power vs. zonal mean zonal wind correlation, the rather systematic structure of the correlation between GW power and PW RMS T is intriguing and suggestive of a close relation between PW amplitudes and GW power. The less systematic correlation structure of GW power vs. zonal mean zonal wind, and the relatively systematic correlation of the latter with PW amplitudes, further

suggest the role of the zonal mean zonal wind as a primary driver of the PW amplitudes. It does not mean that the zonal mean wind does not play a role in GW generation. There are indications that the vortex generates mesospheric GWs above the zonal mean wind maximum, and their correlation backs this hypothesis. However, in the stratosphere and the vicinity of the vortex, the GW power vs zonal mean zonal wind correlations are less systematic, as opposed to the two other correlations. This indicates that the strength of the zonal mean zonal wind in the stratosphere is linked to the PW amplitudes, due to the spontaneous adjustment mechanism. Moreover, the PW amplitudes appear to be related to GW power. Hence, the PW amplitudes seem quite relevant for GW generation.

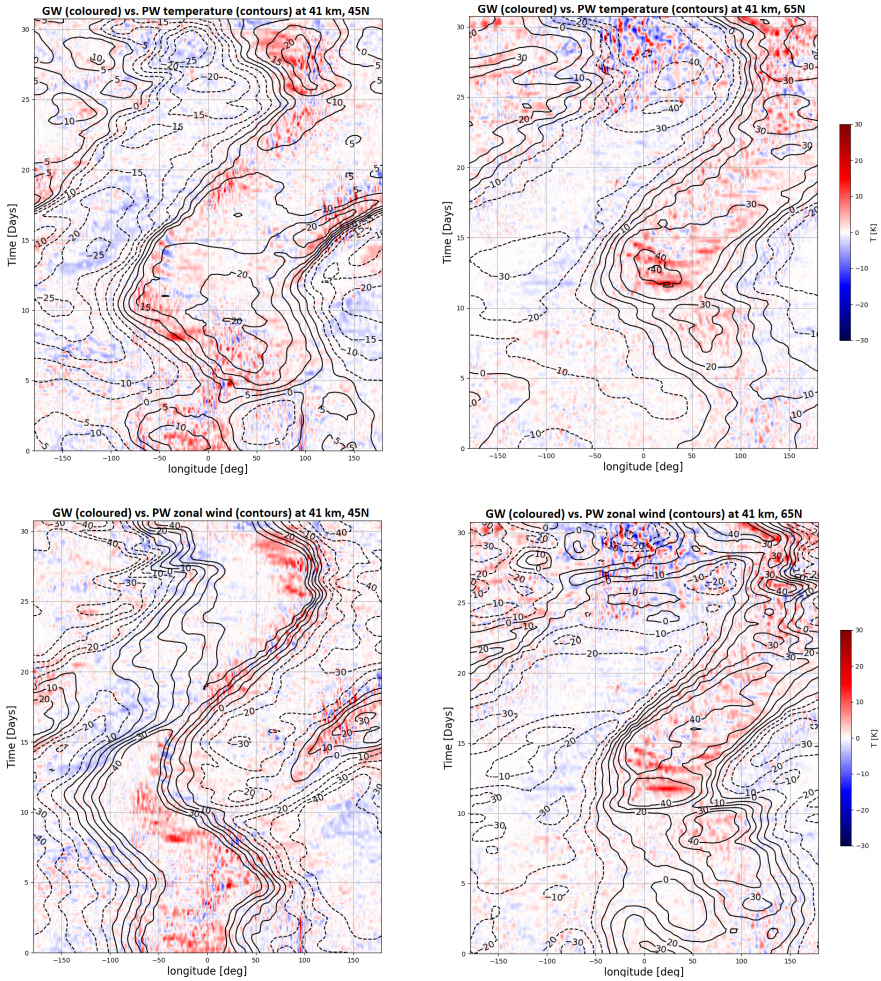

Figure 4.21: Combined Hovmöller plots of GW temperature and PW temperature (upper) and PW zonal wind (lower) at 41 km, at 45°N (left) and 65°N (right). The y-axis represents time in days (start date 1 on 13th Jan), and the longitude is on the x-axis.

A possible mechanism for GW generation by PWs in the middle atmosphere originates from the strong shears caused by the PWs. When PWs are generated and amplified in the spontaneous adjustment mechanism of the polar vortex, the waves are seen as large zonal variations to the background temperature and wind, in this case, strong WN1. They follow the curvature of the polar vortex edge, which is rapidly wobbling and unstable in an adjustment situation, a common feature of such instabilities. At the edges of the PWs that follow, large temperature gradients (in PW T) create strong geostrophic PW winds along the PW edges. The PW winds will then cause strong wind velocity gradients, i.e. strong horizontal wind shears. The stronger the shear, the more in-situ forcing acts to generate temperature and wind perturbations, hence generating non-orographic GWs. This has been a dominant theory of how jets and fronts may generate GWs [46]. The stronger the PW amplitudes, the stronger the horizontal wind shears and the stronger the generating force. Thus, GW activity in the stratosphere tends to follow the PW temperature amplitudes in regions of the atmosphere where the polar vortex is strong enough to cause the spontaneous adjustment that is the primary driving factor. In fact, looking at the combined GW-PW Hovmöller plots of Fig. 4.21, at 41 km, one observes that GW activity is much stronger in regions of large PW temperature amplitudes at 65°N (upper right plot).

When looking at the GW-PW Hovmöller plots on the right-hand side of Fig. 4.21 at 65°N, it is evident that there are significant non-orographic waves present in the strong PW amplitudes of both PW temperature and PW winds. Non-orographic GWs are visible as somewhat weaker-amplitude waves (due to less vertical propagation distance from the source, hence less exponential growth of amplitudes), and with wavefronts that are wide and not quasi-stationary for a day or so (contrary to MWs). Note that the PW T and PW U are in-phase at high latitudes, while out-of-phase at mid-latitudes. GWs are often observed close to or in regions of large PW wind shears, more so in the latter stage at 65°N. For example, large temperature- and PW zonal wind gradients between 100°-180°E occur during the latter days when the polar vortex destabilises, vortex strength decreases, and PWs increase significantly at this latitude. Significant GW activity occurs in this region during the latter days, most likely dominated by non-orographic waves due to the long zonal wavelength scales. Hence, in addition to the large PW U shears present, this suggests strong PW shears generate GWs. However, as seen in the latitude-altitude GW power plots in Fig. 4.11, GW power is strong directly above the strongest polar vortex jet at high latitudes, i.e. above 60 km. Hence, there is reason to believe more non-orographic GWs would be visible at for example 71 km altitude, since at 41 km the waves generated above would not be visible as the vortex wind generally restricts vertical propagation through the strongest winds. Moreover, orographic GWs are seen around 50-0°W in the latter days, attributed to wind over Greenland. Although the PW winds are in-between an eastward-to-westward PW wind transition, the overall zonal wind is moderately eastwards. With favourable ground winds over the mountain range of Greenland, in combination with moderate eastward winds, the MWs are then allowed to propagate vertically.

At mid-latitudes, some non-orographic GWs are generated at different longitudes where the polar vortex edge passes. This is best illustrated by the Hovmöller plots at 41 km, 45° on the left-hand side of Fig. 4.21. Again, non-orographic GWs show somewhat weaker amplitudes, wide wavefronts, and rapidly evolving in time. Although some such waves are visible in regions of strong eastward PW zonal wind, in particular over

the Atlantic (50-0°W) the first few days, most appear along the curve of strong PW zonal wind gradients, as seen with very dense line spacing in the lower left plot in Fig. 4.21. Here, strong shears may generate non-orographic GWs. However, the dominant sources of increased GW power at this latitude stem from orographic waves due to their large amplitudes and extent over Continental Europe, Siberia, and Japan. They are visible as large-amplitude waves of relatively short zonal wavelengths, and with quasi-stationary phases, visible as lines along the time axis. Orographic GWs occur within the eastward PW zonal wind the first 5-7 days over Europe (around 0-10°E), as well as in the eastward PW wind over Eastern Asia (100-180°E) around days 14-19. Furthermore, some orographic GWs, along with non-orographic waves, seem to occur in regions of strong shears, when this occurs over orography. Hence, this suggests orographic GWs are propagating vertically and filtered through by PWs with eastward winds. This is as long as the total wind is not too strong, as it is strong at high latitudes, but not in the mid-latitudes. The filtering is therefore primarily a mid-latitude phenomenon in this simulation. This agrees with the observational and numerical studies suggesting that stratospheric PWs may filter orographic GWs, allowing them to propagate vertically into the mesosphere [26].

Furthermore, it has been found from satellite and atmospheric sounding that quasi-stationary PWs with amplitude-variations of roughly 30 days, attributed to wave-mean flow interactions, correlate well with GW potential energy in the middle atmosphere locally above Europe [12]. Although a remark must be made that this correlation was found at mid-latitude Europe, hence not aligned with the findings in Fig. 4.19. However, the distinct border between correlation and anti-correlation at around 50°N, may not be strict, but may depend on the dataset and the vortex dynamics that drive the PWs. Moreover, it was found by the same study that PW temperature and GW potential energy were out-of-phase in what longitudes their maximal amplitudes occur at mid-latitudes. Interestingly, the Hovmöller plot at 41 km 45°N (upper left) in Fig. 4.21, suggests similarly that in this simulation, mid-latitude GWs typically appear in between the maximal PW amplitudes zonally, hence in regions of large temperature gradients, i.e. strong PW winds.

The lack of apparent similarities in the periodicity of GW power and PW amplitudes may indicate that the PW interaction with GWs found here is mainly in terms of GW generation and enhanced activity, as well as GW filtering by PW winds, rather than direct interactions enhancing or reducing wave amplitudes of already existing waves. However, the dataset is short in terms of studying the dominant periods of the signals. Hence such direct wave-wave interactions cannot be excluded. Moreover, a direct wave-wave interaction may occur on more local scales as GW scales are significantly smaller and locally variable than for PWs. Hence, the amplitudes and propagation characteristics may still be affected by PWs locally in one region. Since this analysis primarily focused on total zonal GW power and PW amplitudes, such interactions on a local scale may become hard to detect. Although the combined GW-PW Hovmöller plots in Fig. 4.21 depict the longitudinal time-evolution of PW and GW amplitudes and phases, it is hard to infer the local effect of PWs on already-existing GWs. This is mainly because of the intermittent and small-scale nature of GWs and since the PW shears themselves generate GWs. Hence, a possibility in studying the direct wave-wave interaction may be to extend Alexandersen's work on the correlation of wave phases rather than the zonal amplitude and power at focus here. Rather than looking at the time series at a single grid point, one might pick a

zonal-vertical, meridional-vertical, or horizontal plane of the model to calculate GW-PW correlation indices. For example, a PW-GW phase correlation for a zonal-vertical plane at mid- and high latitudes, may reveal systematic correlation of their phases longitudinally and vertically, and possibly highlight differences between latitudes.

Overall, the findings suggest that orographic GWs are dominant in the mid-latitudes in regions of eastward PW winds, when the polar vortex edge is located above orography. Furthermore, there are strong indications that non-orographic GWs are generated in the stratosphere and mesosphere, in the vicinity of the polar vortex, due to strong wind shears. The shears are caused by strong WN1 PWs that are likely amplified and shed by the polar vortex due to vortex instability and a spontaneous adjustment event to regain stability. The GW power is correlated with PW amplitudes in the middle atmosphere at high latitudes, due to the strongly non-orographic dominance of waves here. On the other hand, in the mid-latitudes, GW power and PW amplitudes are somewhat anti-correlated, due to orographic GWs being dominant, which show some variability in occurrence zonally.

Chapter 5

Conclusion & Further Work

The role of PWs in the generation and propagation of GWs in the middle atmosphere in the Northern Hemisphere winter has been studied by using the high-resolution WACCM-X. The simulation interval has been from 13th Jan to 12th Feb, with a 6-hour time resolution. It is found that the zonal GW power, proportional to the total zonal GW potential energy, is positively correlated with PW RMS temperature amplitudes in the middle atmosphere at high latitudes, north of 55°N. On the other hand, they are anti-correlated in the mid-latitudes between 30-55°N. This reflects two different regions of GW-PW interaction. In the mid-latitudes, the primary source of zonal GW power is from the orographic GWs. These appear mainly over Europe and Northeastern Asia when the polar vortex makes a southward migration off the Pole, so the edge is located above orography, but with moderate winds only. The PWs are generally weak, but their associated zonal winds are typically in their eastward phase in the stratosphere when orographic GWs are seen propagating from the ground to the mesosphere. Hence, the simulation observes the filtering of orographic GWs by PW winds, particularly in the mid-latitudes, consistent with observations. However, the vortex strengthens and migrates polewards with sudden wobbles when PWs from the troposphere propagate upward. The overall result is a strengthening of PWs in the middle atmosphere at both mid and high latitudes. Meanwhile, the orographic GWs in the mid-latitudes die out due to the absence of the vortex edge that favours their existence. Hence their activity against the PW amplitudes is anti-correlated. On the other hand, non-orographic GWs are dominant at high latitudes, and occur in the middle atmosphere only, in regions of strong wind shears due to large PW amplitudes. Hence, the GW power correlation with PW RMS T indicates that the significant source of GWs is very likely from the strong wind and temperature variations associated with PWs, particularly near the polar vortex.

These are significant results, first of all, because they show that the WACCM-X can realise GW processes consistent with observations, e.g. the orographic GWs over Europe, and non-orographic GWs around the vortex edge. Secondly, the results broaden the perspective of the GW-PW interactions to the whole middle atmosphere in the winter mid- and high-latitudes, compared to the previous single-point analysis done by Alexander-

sen from WACCM5 [3]. Thirdly, they indicate that the sources of non-orographic GWs are primarily PW wind shears near the polar vortex, which are again associated with the complex vortex-PW interaction through a spontaneous adjustment event. However, while correlations are found at high latitudes and regions of GWs are located, the process is complex and intermittent. Nevertheless, such a simulation using a high-resolution model that parameterises non-orographic GWs has previously been proposed as a possible way to progress our knowledge of their generation in practice in a full-atmosphere simulation [46]. Hence, the analysis from this unique WACCM-X simulation helps us understand the intertwined mechanism, where the polar vortex is linked to PW generation, and PW shears appear to become sources of GWs.

However, the correlation is based on a 31-day simulation, where GW power, PW RMS amplitudes, and the zonal mean zonal wind are found to have long-period oscillations, and therefore few cycles in the time interval. It is somewhat uncertain whether these periodic signals are general for the whole winter and occur for several winters, or if they are purely a one-time event. Hence, a longer dataset is needed and should be a focus for further studies. However, a full-year simulation run of WACCM-X is underway and may become available in the future.

Furthermore, this study focused on the total zonal GW power and PW amplitudes in the NH middle atmosphere. The interactions found are in terms of filtering of GWs by PW winds and generation of non-orographic GWs by PW shear forcing. More direct and local interactions regarding GW amplification/reduction by PWs, are hard to detect by this method. Such an analysis could build upon ideas from this thesis, specifically in wave filtering and calculating 2D correlation plots. Moreover, the work of Alexandersen may be expanded. Instead of looking at GW-PW phase correlation at a single point, 2D correlation profiles could be calculated for specific zonal-vertical, meridional-vertical and horizontal planes. For example, a PW-GW phase correlation for a zonal-vertical plane at mid- and high latitudes, may reveal systematic correlation of their phases longitudinally and vertically, and possibly highlight differences between latitudes.

Bibliography

[1] M. J. Alexander, S. D. Eckermann, D. Broutman, and J. Ma. Momentum flux estimates for south georgia island mountain waves in the stratosphere observed via satellite. *Geophysical Research Letters*, 36(12), 2009.

[2] M. J. Alexander, M. Geller, C. McLandress, S. Polavarapu, P. Preusse, F. Sassi, K. Sato, S. Eckermann, M. Ern, A. Hertzog, Y. Kawatani, M. Pulido, T. A. Shaw, M. Sigmond, R. Vincent, and S. Watanabe. Recent developments in gravity-wave effects in climate models and the global distribution of gravity-wave momentum flux from observations and models. *Quarterly Journal of the Royal Meteorological Society*, 136(650):1103–1124, 2010.

[3] H. Alexandersen. Resolved gravity waves in a high-resolution model - the interaction of gravity waves with planetary waves. Master's Thesis, Norwegian University of Science and Technology, 2022.

[4] D. G. Andrews. *An Introduction to Atmospheric Physics*. Cambridge University Press, 2 edition, 2010.

[5] R. M. Barton. Vertical temperature structure of the atmosphere. StratusDeck `https://stratusdeck.co.uk/vertical-temperature-structure`. Accessed: 01.12.2022.

[6] E. Becker and S. L. Vadas. Secondary gravity waves in the winter mesosphere: Results from a high-resolution global circulation model. *Journal of Geophysical Research: Atmospheres*, 123(5):2605–2627, 2018.

[7] E. O. Bingham. *The Fast Fourier Transform and its Applications*. Prentice Hall, Englewood Cliffs, New Jersey, USA, 1988.

[8] K. Boateng, B. Weyori, and D. Laar. Improving the effectiveness of the median filter. *International Journal of Electronics and Communication Engineering*, 5:85–97, 01 2012.

[9] K. Bossert, S. L. Vadas, L. Hoffmann, E. Becker, V. L. Harvey, and M. Bramberger. Observations of stratospheric gravity waves over europe on 12 january 2016: The role of the polar night jet. *Journal of Geophysical Research: Atmospheres*, 125(21):e2020JD032893, 2020. e2020JD032893 2020JD032893.

[10] N. Butchart. The stratosphere: a review of the dynamics and variability. *Weather and Climate Dynamics*, 3(4):1237–1272, 2022.

[11] Y. Calisesi, H. Wernli, and N. Kämpfer. Midstratospheric ozone variability over bern related to planetary wave activity during the winters 1994–1995 to 1998–1999. *Journal of Geophysical Research: Atmospheres*, 106(D8):7903–7916, 2001.

[12] U. Das. Short- and long-term stationary planetary wave variability in the middle atmosphere in contemporaneous satellite and reanalysis data. *Journal of Atmospheric and Solar-Terrestrial Physics*, 231:105864, 2022.

[13] T. J. Dunkerton and N. Butchart. Propagation and selective transmission of internal gravity waves in a sudden warming. *Journal of Atmospheric Sciences*, 41:1443–1460, Apr. 1984.

[14] A. Dörnbrack. Stratospheric mountain waves trailing across northern europe. *Journal of the Atmospheric Sciences*, 78(9):2835 – 2857, 2021.

[15] A. Dörnbrack, S. Gisinger, N. Kaifler, T. C. Portele, M. Bramberger, M. Rapp, M. Gerding, J. Söder, N. Žagar, and D. Jelić. Gravity waves excited during a minor sudden stratospheric warming. *Atmospheric Chemistry and Physics*, 18(17):12915–12931, 2018.

[16] A. Eliassen and E. Palm. *On the Transfer of Energy in Stationary Mountain Waves*. (Det Norske Videnskaps-Akademi i Oslo. Geofysiske publikasjoner). I kommisjon hos Aschehoug, 1961.

[17] P. J. Espy. Our friend the gravity wave. Stockholm University, 2016. Accessed: 05.11.2022.

[18] D. C. Fritts and M. J. Alexander. Gravity wave dynamics and effects in the middle atmosphere. *Reviews of Geophysics*, 41(1), 2003.

[19] C. Hafen. Read netcdf data with python. `https://towardsdatascience.com/read-netcdf-data-with-python-901f7ff61648`, 2020. Accessed: 26.11.2022.

[20] V. L. Harvey, R. B. Pierce, T. D. Fairlie, and M. H. Hitchman. A climatology of stratospheric polar vortices and anticyclones. *Journal of Geophysical Research: Atmospheres*, 107(D20):ACL 10–1–ACL 10–22, 2002.

[21] P. Haynes. Stratospheric dynamics. *Annual Review of Fluid Mechanics*, 37(1):263–293, 2005.

[22] C. O. Hines. Internal atmospheric gravity waves at ionospheric heights. *Canadian Journal of Physics*, 38(11):1441–1481, 1960.

[23] K. Hocke, S. Studer, O. Martius, D. Scheiben, and N. Kämpfer. A 20-day period standing oscillation in the northern winter stratosphere. *Annales Geophysicae*, 31:755–764, 04 2013.

[24] J. R. Holton. The role of gravity wave induced drag and diffusion in the momentum budget of the mesosphere. *Journal of Atmospheric Sciences*, 39(4):791 – 799, 1982.

[25] W. Li, C. Huang, and S. Zhang. Global characteristics of the westward-propagating quasi-16-day wave with zonal wavenumber 1 and the connection with the 2012/2013 SSW revealed by ERA-Interim. *Earth, Planets and Space*, 73(1):113, Dec. 2021.

[26] R. S. Lieberman, D. M. Riggin, and D. E. Siskind. Stationary waves in the wintertime mesosphere: Evidence for gravity wave filtering by stratospheric planetary waves. *Journal of Geophysical Research: Atmospheres*, 118(8):3139–3149, 2013.

[27] R. Lindsey. Understanding the arctic polar vortex. `https://www.climate.gov/news-features/understanding-climate/understanding-arctic-polar-vortex`, 2021. Accessed: 23.05.2023.

[28] R. S. Lindzen. Turbulence and stress owing to gravity wave and tidal breakdown. *Journal of Geophysical Research: Oceans*, 86(C10):9707–9714, 1981.

[29] H.-L. Liu. Cedar tutorial: Atmospheric gravity waves: Apply classroom physics to research. `https://cedarscience.org/cedar-tutorials-videos`, 2008. Accessed: 05.11.2022.

[30] H.-L. Liu. Quantifying gravity wave forcing using scale invariance. *Nature Communications*, 10, 06 2019.

[31] H.-L. Liu, C. G. Bardeen, B. T. Foster, P. Lauritzen, J. Liu, G. Lu, D. R. Marsh, A. Maute, J. M. McInerney, N. M. Pedatella, L. Qian, A. D. Richmond, R. G. Roble, S. C. Solomon, F. M. Vitt, and W. Wang. Development and validation of the whole atmosphere community climate model with thermosphere and ionosphere extension (waccm-x 2.0). *Journal of Advances in Modeling Earth Systems*, 10(2):381–402, 2018.

[32] H.-L. Liu, J. M. McInerney, S. Santos, P. H. Lauritzen, M. A. Taylor, and N. M. Pedatella. Gravity waves simulated by high-resolution whole atmosphere community climate model. *Geophysical Research Letters*, 41(24):9106–9112, 2014.

[33] N. R. Lomb. Least-Squares Frequency Analysis of Unequally Spaced Data. , 39(2):447–462, Feb. 1976.

[34] A. Mann. To improve weather and climate models, researchers are chasing atmospheric gravity waves. *Proceedings of the National Academy of Sciences*, 116(39):19218–19221, 2019.

[35] A. Manson, C. Meek, Y. Luo, W. Hocking, J. MacDougall, D. Riggin, D. Fritts, and R. Vincent. Modulation of gravity waves by planetary waves (2 and 16 d): observations with the north american-pacific mlt-mfr radar network. *Journal of Atmospheric and Solar-Terrestrial Physics*, 65(1):85–104, 2003.

[36] J. P. McCormack, V. L. Harvey, C. E. Randall, N. Pedatella, D. Koshin, K. Sato, L. Coy, S. Watanabe, F. Sassi, and L. A. Holt. Intercomparison of middle atmospheric meteorological analyses for the northern hemisphere winter 2009–2010. *Atmospheric Chemistry and Physics*, 21(23):17577–17605, 2021.

[37] N. A. McFarlane. The Effect of Orographically Excited Gravity Wave Drag on the General Circulation of the Lower Stratosphere and Troposphere. *Journal of Atmospheric Sciences*, 44(14):1775–1800, July 1987.

[38] K. S. Moen. Separation of atmospheric gravity waves, planetary waves and tides in a high-resolution general circulation model. Physics Specialisation Project, Norwegian University of Science and Technology, 2022.

[39] G. D. Nastrom and K. S. Gage. A climatology of atmospheric wavenumber spectra of wind and temperature observed by commercial aircraft. *Journal of Atmospheric Sciences*, 42(9):950 – 960, 1985.

[40] NCAR. Ncar sima geospace. `https://app.globus.org/file-manager?origin_id=69c93e3c-3e80-11ec-890a-417713cb3dee&origin_path=%2F`, Accessed: 24.01.2023.

[41] R. B. Neale, C.-C. Chen, A. Gettelman, P. H. Lauritzen, S. Park, D. L. Williamson, A. J. Conley, R. Garcia, D. Kinnison, J.-F. Lamarque, et al. Description of the ncar community atmosphere model (cam 5.0). *NCAR Tech. Note NCAR/TN-486+ STR*, 1(1):1–12, 2010.

[42] NOAA. Jetstream - longwaves and shortwaves. National Weather Service and National Oceanic and Atmospheric Administration, `https://www.weather.gov/jetstream/longshort`. Accessed: 29.11.2022.

[43] NumPy. numpy.fft.rfft. NumPy, `https://numpy.org/doc/stable/reference/generated/numpy.fft.rfft.html`. Accessed: 20.02.2023.

[44] D. A. Ortland and M. J. Alexander. Gravity wave influence on the global structure of the diurnal tide in the mesosphere and lower thermosphere. *Journal of Geophysical Research: Space Physics*, 111(A10), 2006.

[45] P. Pieter. Butterworth filters. 2021. `https://tttapa.github.io/Pages/Mathematics/Systems-and-Control-Theory/Analog-Filters/Butterworth-Filters.html` Accessed: 07.12.2022.

[46] R. Plougonven and F. Zhang. Internal gravity waves from atmospheric jets and fronts. *Reviews of Geophysics*, 52(1):33–76, 2014.

[47] PyAstronomy. The generalized lomb-scargle periodograms (gls) pyastronomy documentation. PyAstronomy, `https://pyastronomy.readthedocs.io/en/latest/pyTimingDoc/pyPeriodDoc/gls.html`. Accessed: 31.03.2023.

[48] J. D. Scargle. Studies in astronomical time series analysis. II. Statistical aspects of spectral analysis of unevenly spaced data. , 263:835–853, Dec. 1982.

[49] SciPy. scipy.ndimage.median-filter. SciPy, https://docs.scipy.org/doc/scipy/reference/generated/scipy.ndimage.median_filter.html. Accessed: 21.11.2022.

[50] SciPy. scipy.signal.iirfilter. SciPy, https://docs.scipy.org/doc/scipy/reference/generated/scipy.signal.iirfilter.html. Accessed: 07.12.2022.

[51] SciPy. scipy.signal.sosfiltfilt. SciPy, https://docs.scipy.org/doc/scipy/reference/generated/scipy.signal.sosfiltfilt.html. Accessed: 07.12.2022.

[52] A. K. Smith. The origin of stationary planetary waves in the upper mesosphere. *Journal of the Atmospheric Sciences*, 60(24):3033 – 3041, 2003.

[53] N. Stray. Planetary waves in the mlt: Vertical coupling and effects. Doctoral thesis, Norwegian University of Science and Technology, 2015.

[54] R. Stull. Weather for sailing, flying snow sports - gravity waves. www.eoas.ubc.ca/courses/atsc113/flying/met_concepts/03-met_concepts/03d-mountain_waves/index.html. Accessed: 01.11.22.

[55] UCAR. The netcdf data model. https://docs.unidata.ucar.edu/netcdf-c/current/netcdf_data_model.html, Accessed: 20.12.2022.

[56] G. K. Vallis. *Atmospheric and Oceanic Fluid Dynamics*. Cambridge University Press, Cambridge, U.K., 2006.

[57] J. Vanderplas. Understanding the lomb-scargle periodogram. *The Astrophysical Journal Supplement Series*, 236, 03 2017.

[58] VirginiaTech. At the edge of the clouds. Bradley Department of Electrical and Computer Engineering, Virginia Tech. https://ece.vt.edu/research/annual-report/annual-report-2022/edge-of-clouds.html, Accessed: 05.11.2022.

[59] M. Zechmeister and M. Kürster. The generalised lomb-scargle periodogram - a new formalism for the floating-mean and keplerian periodograms. *A&A*, 496(2):577–584, 2009.

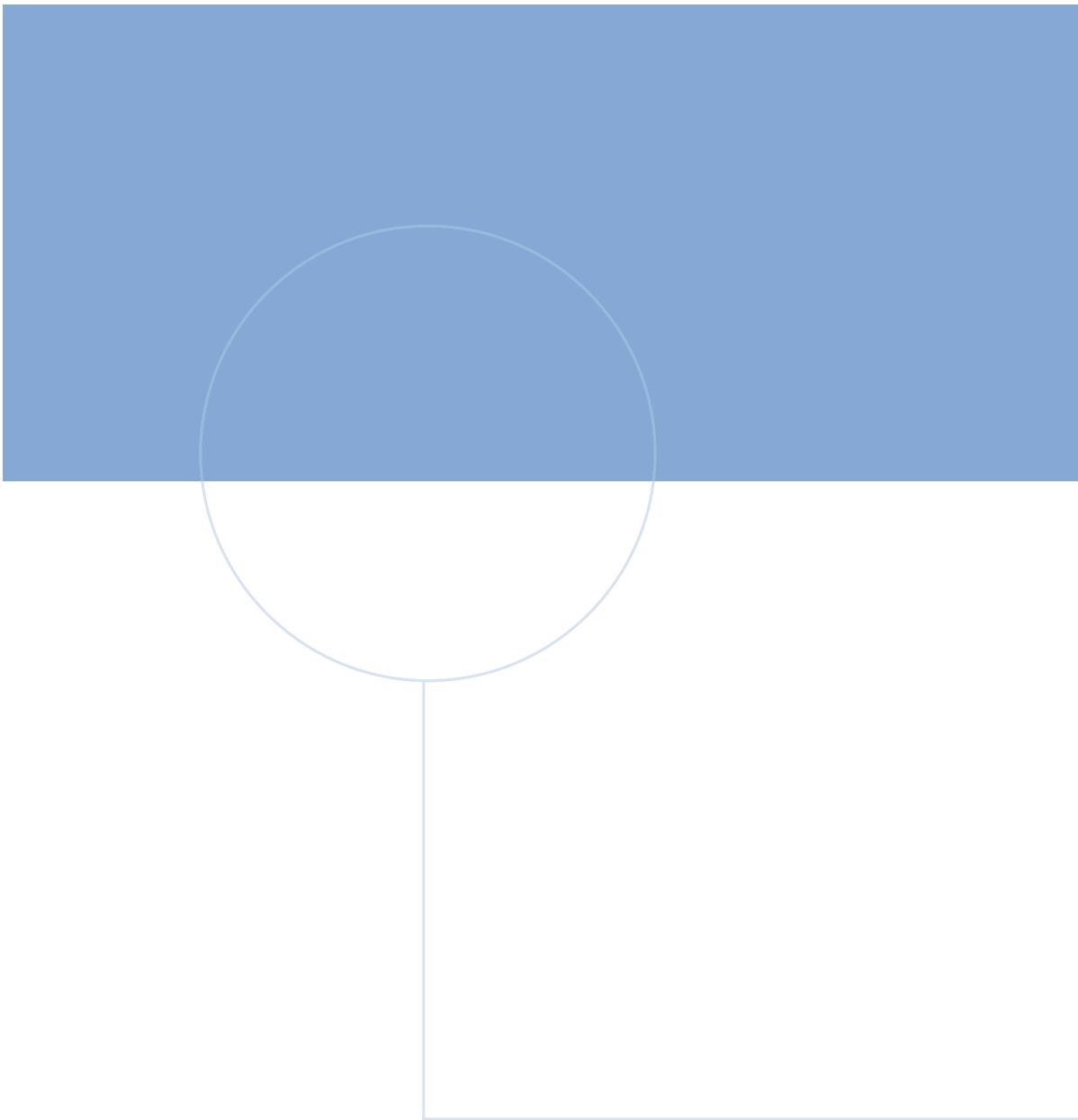

NTNU

Norwegian University of
Science and Technology